The Messenger

No. 151 – March 2013

Progress on the VLT deformable secondary mirror
Commissioning of KMOS
Ultra-faint dwarf galaxies
The VIPERS redshift survey

ESO

Upgrading VIMOS — Part II

Peter Hammersley[1]
Ronald Brast[1]
Paul Bristow[1]
Pierre Bourget[1]
Roberto Castillo[1]
Hans Dekker[1]
Michael Hilker[1]
Jean-Louis Lizon[1]
Christian Lucuix[1]
Vincenzo Mainieri[1]
Steffen Mieske[1]
Dan Popovic[1]
Claudio Reinero[1]
Marina Rejkuba[1]
Chester Rojas[1]
Ruben Sanchez-Jannsen[1]
Fernando Selman[1]
Alain Smette[1]
Josefina Urrutia Del Rio[1]
Javier Valenzuela[1]
Burkhard Wolff[1]

[1] ESO

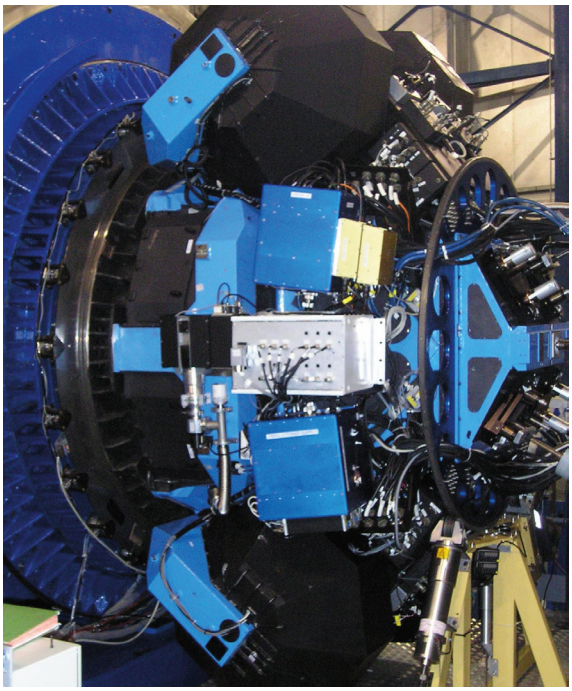

Figure 1. VIMOS on the Nasmyth platform of VLT UT3.

VIMOS is the powerful visible (360–1000 nm) imager and multi-object/integral field spectrometer mounted on the VLT Unit Telescope 3, Melipal. Its high multiplex advantage makes it ideal for undertaking large-scale spectroscopic surveys of faint sources. In order to extend the life of the instrument, improve its performance and prepare for possible large-scale surveys, in 2009 it was decided to upgrade VIMOS. The first phase of the upgrade, which included replacing the detectors and the fitting of an active flexure compensation system, has been previously reported; this article describes the second stage of the upgrade, which has improved the delivered image quality and stability.

The instrument and upgrades

VIMOS has four identical arms, each with a 7 by 8 arcminute field of view on the sky with a gap between the fields of 2 arcminutes. The instrument offers three main modes:

- *UVBRIz*-band imaging covering four fields each 7 × 8 arc-minutes;
- slitlet-based multi-object spectroscopy with spectral resolutions from a few hundred to 2500 in each of the four imaging fields;
- integral field unit (IFU) spectroscopy with three fields of view: 13 by 13, 27 by 27, and 54 by 54 arcseconds depending on the specific mode requested.

VIMOS and its commissioning on the VLT in 2002 were described in Le Fevre et al. (2002) and in operation by D'Odorico et al. (2003). After eight years of operation it became necessary to upgrade the instrument in order to address various issues and to extend its useful life. The first phase of the upgrade was implemented in 2010, (Hammersley et al., 2010) and included:

- Replacement of the shutters, which were worn out.
- Replacement of the CCD detectors, which has improved the sensitivity in the red and reduced the fringing.
- Reduction of the instrument flexure.
- Provision of new mask cabinets that keep masks in position more reliably.
- Improvement of the data reduction pipeline.

The second upgrade phase took place in 2011–12 and addressed a number of issues which became apparent following the first phase: image quality; the focus mechanisms and their control; the efficiency of the HR-blue grism; calibration and operational procedures; and operational efficiency.

This article discusses the results of this second phase. More technical details on the overall upgrade programme can be found in Hammersley et al. (2012).

Improving image quality

Following the change of the detector, it became apparent that the optimum focus was changing across the detector due to a tilt between the detector and the re-imaged focal plane. This meant that if the detector was well focused at its centre, then the edges would not be as well focused. Due to the optical configuration of VIMOS this could lead to the images at the corners of each detector becoming significantly elongated.

In May 2011 an intervention was made to correct this effect by moving one of the lenses and the detector laterally with respect to the rest of the optics. This reduced the tilt between the telescope focal plane and detector by typically a factor five. At the correct focus only the extreme corners of the array showed a small amount of astigmatism. Figure 2 shows the evolution of average

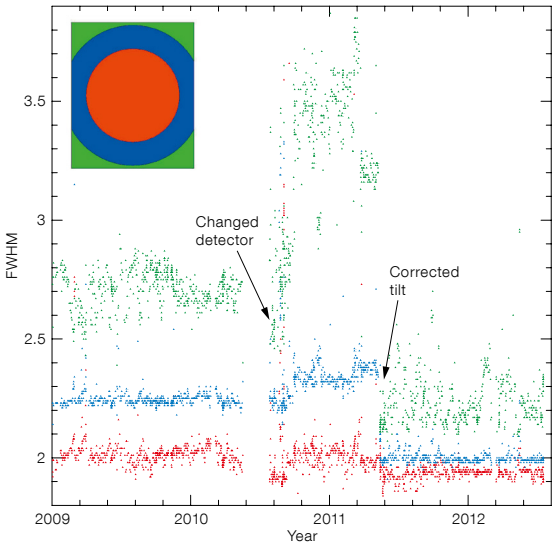

Figure 2. Evolution of the image FWHM in pixels since 1 January 2009 for VIMOS channel 4. The red points correspond to the average FWHM of the pinholes within 800 pixels of the centre; blue between 800 and 1200 pixels and green to those beyond 1200 pixels (see the schematic of the regions used on the detector to the upper left). Arrows mark when the detector was changed and the tilt corrected.

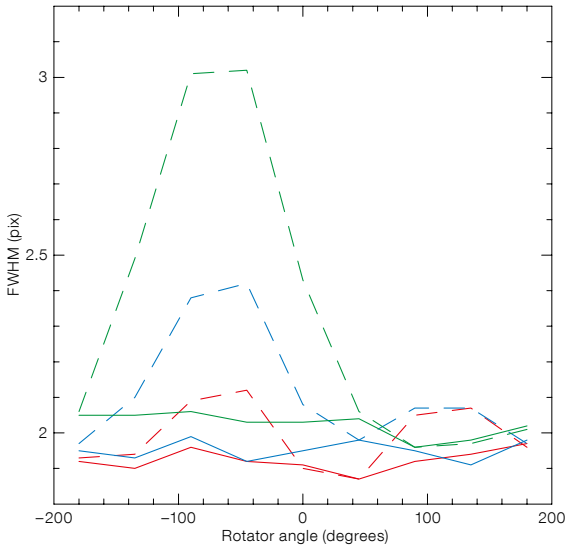

Figure 3. Variation of the FWHM in pixels with rotator angle for VIMOS channel 3. The dashed lines show the case with no focus compensation and the solid lines with compensation.

image quality in three regions of detector 4 since 1 January 2009. The data were obtained using daytime calibration images of a pinhole mask placed in the focal plane. The dates when the detector was changed and the tilt corrected are marked with arrows on Figure 2. The degradation of image quality following the detector exchange is clear, but following the correction of the tilt, the image quality towards the edge of the detector has significantly improved. Currently, approximately 90% of the imaging area has an image full width at half maximum (FWHM) < 2.4 pixels and an ellipticity below 0.1, whereas prior to the upgrade it was closer to 70%.

Focus control

The original focus mechanism and control software also limited the performance of the instrument. Among the problems were: the stepper motor could lose steps and so lead to a drift in the focus position of the camera; the camera focus changed significantly with the rotator angle and this could not be corrected; it was not possible to control the focus for each grism; updating the focus parameters in the control software was very complicated and it was very easy to inadvertently make mistakes which were not immediately obvious.

In March 2012 the original focus stepper motors were replaced with DC motors, each with an encoder. The software was updated to allow the focus offset to now take into account rotator angle and grism as well as temperature and filter for each channel. After implementing the new motors and encoders, it was found that the mechanism did not have sufficient range to focus all of the modes correctly, affecting in particular the IFU, and so a further intervention in October 2012 was required to correct this.

Figure 3 shows the variation in FWHM with rotator angle when observing the pinhole mask for the three colour-coded regions designated in Figure 2. The dashed lines show the FWHM with no compensation with rotator angle and the solid lines indicate the cases with compensation. This plot demonstrates that the instrument is now far closer to the optimum focus in normal operation where the rotator angle is constantly changing.

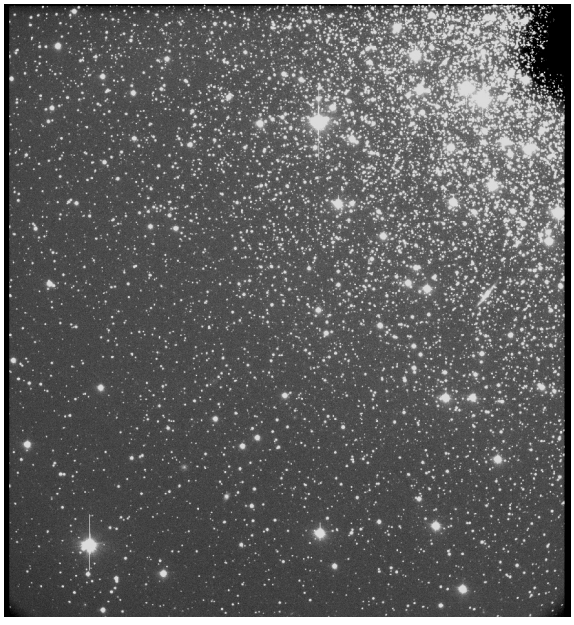

Figure 4. *R*-band image of the globular cluster M55 taken in October 2012, after the focus upgrade. This shows the whole field of view in channel 3 (7 by 8 arcminutes). The dark area to the top right is caused by the guide probe vignetting the image.

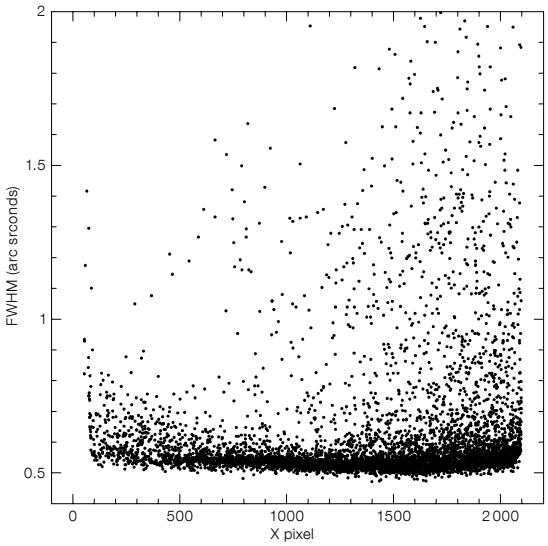

Figure 5. The variation of the stellar FWHM, in arcseconds, as a function of the X position on the image shown in Figure 4.

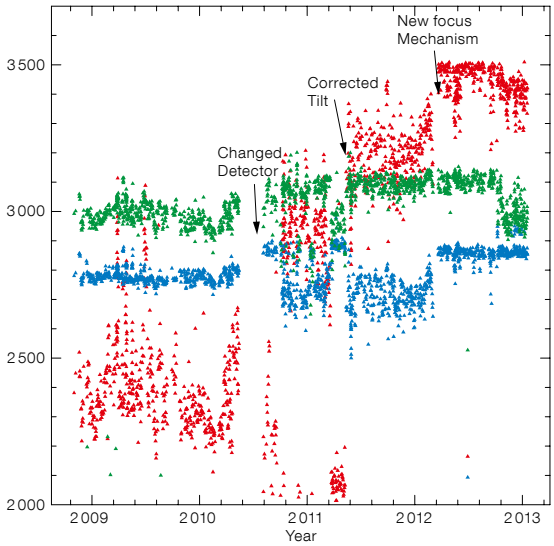

Figure 6. The spectral resolution in the red, blue and central regions of lamp spectra, colour-coded red, blue and green, taken with the HR-orange grism in IFU mode for channel 1 is shown. The dates when the detector was changed, the tilt corrected and the new focus mechanism were implemented are all marked. It should be noted that this is one of the more extreme examples.

Figure 4 shows a VIMOS *R*-band image of the globular cluster M55, taken with 0.5-arcsecond seeing during the last intervention. This uses the full imaging field of view on channel 3. Figure 5 shows how the image quality varies with position on the horizontal axis (X direction). The sources with FWHM ~ 0.55 arcseconds are stars, while extended background objects and blended stars have larger FWHM, in particular near the centre of the globular cluster (top right). There is some elongation in the bottom corners of the image and the FWHM in those regions increases from about 0.55 to 0.60 arcseconds.

Spectral resolution

The grisms used by VIMOS are placed in the pupil and it was originally assumed that these would not significantly affect the focus. Tests in May 2011, however, showed that this was not the case, and the high-resolution grisms in particular required a significant focus offset if the spectral resolution was to be maintained across the whole detector. When the focus was not optimum then the resolution was degraded, particularly at each end of the spectral range. The new focus control allows the focus to be set for each grism and this has led to the resolution being more uniform between the four quadrants and over time. The red end of the spectrum now always has a higher resolution than the blue (as it should be), which was not always the case beforehand.

As an illustration of the implication of this change for observations, we estimate that programmes to detect Lyman-α emitters at high redshift would have up to a 40 % gain in sensitivity just because the red end of the HR-red spectrum

Figure 7. The total VIMOS efficiency when using the old (purple) and new (green) HR-blue grisms is shown.

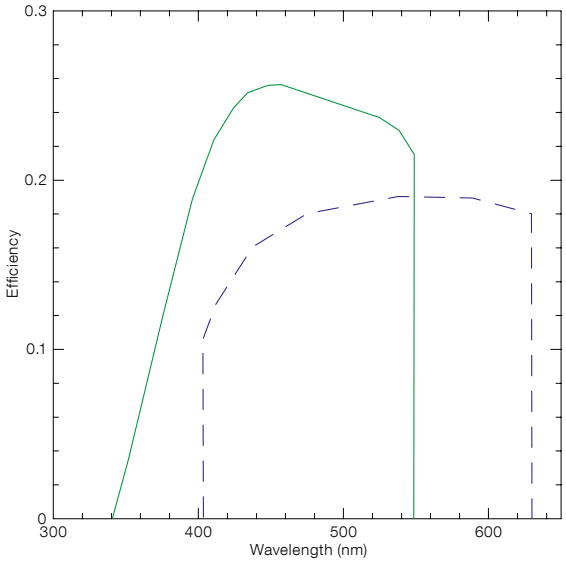

Figure 8. The evolution of the average technical down time of VIMOS from 2008 to 2011 showing the improvement resulting from the upgrade activities.

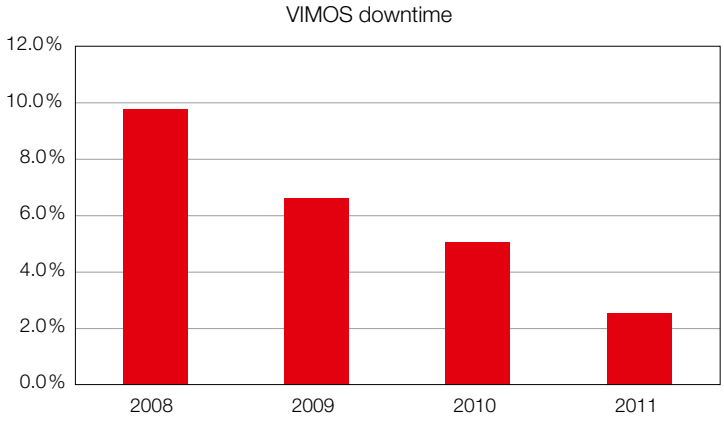

is now in focus. Figure 6 shows the evolution of the resolution of the HR-orange grism for channel 1 since 2009. The dates when the detector was changed, the tilt corrected and the new focus mechanism installed are marked. As is apparent, since March 2012 the red spectral region, in particular, has improved, although some fine tuning is still required.

HR-blue grism

The original HR-blue grism had a relatively low transmission and so early on when the upgrade was planned it was decided to replace it with a Volume Phase Holographic (VPH) grism. The transmission of the new grism is up to about 50 % higher and there is useful transmission below 360 nm (Figure 7). The spectral resolution has, however, been reduced by about 30 % and the new dispersion is 0.71 Å per pixel.

Operations

A significant effort has been made to improve the reliability of VIMOS. Some of the maintenance procedures have been modified and strengthened, such as making a test insertion every time a new mask is loaded into the instrument. As Figure 8 demonstrates, these procedures have noticeably reduced the technical down time.

Additional steps have also been taken to make the science operations more efficient. One example is the elimination of the mandatory need for pre-imaging using the PILMOS mode to prepare the masks, which can now be cut directly, based on user catalogues (see Bristow et al., 2012).

An upgraded VIMOS

The VIMOS upgrade programme, which is now nearing its conclusion, has been made possible by a significant and successful collaboration between the ESO staff at Garching and Paranal. The most important improvements are:

1) The instrument has a better sensitivity in the red.
2) There is far lower detector fringing, allowing better sky subtraction in the red.
3) Opto-mechanically, VIMOS is more stable, which makes the instrument simpler to calibrate.
4) There is a higher and more stable image quality across the whole detector.
5) The observing efficiency has improved.
6) The technical down time has decreased.

As a result, VIMOS is now a significantly more powerful instrument that when it was originally mounted on the telescope and it is ready for many more years of ground-breaking science.

References

Bristow, P. et al. 2012, The Messenger, 148, 13
D'Odorico, S. et al. 2003, The Messenger, 113, 26
Hammersley, P. et al. 2010, The Messenger, 142, 13
Hammersley, P. et al. 2012, SPIE, 486, 5MH
Le Fevre, O. et al. 2002, The Messenger, 109, 21

ESO/R. Gendler

VIMOS colour image of the barred spiral galaxy NGC 1097, with additional colour information from an image taken by amateur astronomer Robert Gendler superimposed. VIMOS images in *B*-, *V*- and *R*-bands were combined and highlight the star formation regions in the spiral arms, the dust lanes in the bar and the starburst ring around the active galactic nucleus. The companion elliptical galaxy is NGC 1097A at a similar distance of 20 Mpc. See Picture of the Week 11 July 2011 (potw1128a) for more details.

Six Years of Science with the TAROT Telescope at La Silla

Alain Klotz[1]
Michel Boer[2]
Jean-Luc Atteia[1]
Bruce Gendre[1]
Jean-François Le Borgne[1]
Eric Frappa[3]
Frederic Vachier[4]
Jerome Berthier[4]

[1] IRAP-Observatoire Midi Pyrénées, Toulouse, France
[2] ARTEMIS-CNRS/OCA/UNS, Nice, France
[3] Planetarium de Saint-Etienne, France
[4] IMCCE-Observatoire de Paris, France

The TAROT telescopes are a pair of robotic autonomous observatories with identical suites of instrumentation, with one located in each hemisphere. The southern TAROT telescope, which was installed in 2006 at the La Silla Observatory, uses more than 90 % of the clear night-time, and has become a very reliable and productive instrument. The primary objective of TAROT is the detection and study of the optical counter-parts of cosmic gamma-ray bursts, and many results have been obtained in this area. But several other topics, ranging from stellar physics to supernovae, have also been addressed successfully thanks to the telescope's flexibility. We present the main scientific results obtained by the TAROT robotic observatory at La Silla.

TAROT (Télescope à Action Rapide pour les Objets Transitoires — Rapid Action Telescope for Transient Objects) consists of two robotic autonomous observatories located at the ESO La Silla Observatory and at the Observatoire de la Côte d'Azur, Calern Observatory in France. They are 25-centimetre aperture telescopes with a field of view of 2 by 2 degrees (see Figure 1) and a pixel scale of 3.3 arcseconds. Images are recorded by an Andor 2k by 2k thinned CCD camera. With a six-position filter wheel, the user can choose between one of the *BVRI* filters, a special graded neutral density V filter and an open (clear) position. The equatorial mount can slew to any part of the sky in less than ten seconds (Klotz et al., 2008). The technical details of TAROT at La Silla have been presented by Boër et al. (2003). At present, the reliability of TAROT is such that more than 90 % of the available time (i.e., cloudless night-time) is used for scientific observations.

Figure 1. A wide-field image of the nearby early-type galaxy NGC 5128, which hosts the radio source Centaurus A, demonstrating the TAROT field of view of 2 by 2 degrees.

Observation of gamma-ray bursts

The TAROT telescopes were designed in 1995 in order to catch the optical counterparts of gamma-ray bursts (GRBs). At that time, GRBs were known as short events (typically a few seconds) observed only by high-energy instruments on satellites. There were however theoretical predictions that GRBs should be also detectable at optical wavelengths (Rees & Meszaros, 1992). The design of TAROT was constrained by the large error boxes (more than 5 by 5 degrees) provided by the BATSE instrument aboard the Compton Gamma Ray Observatory (CGRO) satellite. In 1997 the BeppoSAX satellite observed the first X-ray afterglow (Costa et al., 1997) and could provide a precise position to the Nordic Optical Telescope (NOT) telescope which, in turn, recorded the first optical afterglow (van Paradijs et al., 1997).

Optical detection enables the GRB redshift to be measured. This was the ultimate proof that these objects originate from distant, cosmological sources. Current models of gamma-ray bursts involve either the disruption of a massive star with the fall-off of a transient accretion disc onto a newly born black hole and the emission of a powerful, highly relativistic collimated jet, or the coalescence of a binary system of compact objects (neutron star — neutron star or black hole — neutron star); see Gehrels & Mésáros (2012).

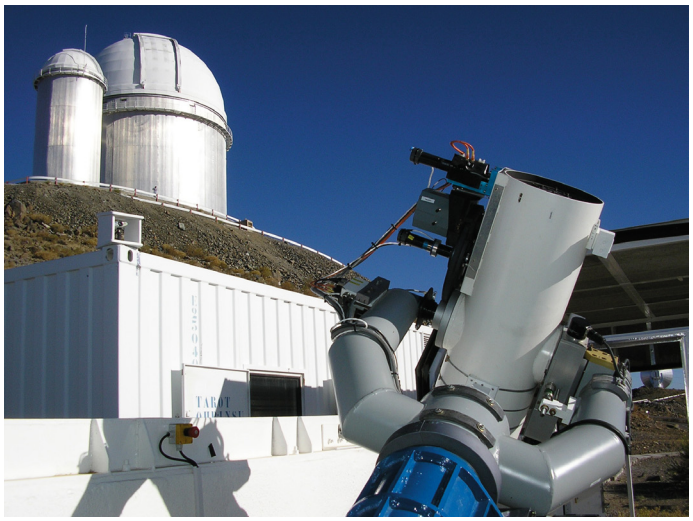

Figure 2. The TAROT La Silla telescope is located at the foot of the hill below the ESO 3.6-metre telescope in the former GMS building. Computers and electrical devices are stored in the adjacent shelter. The telescope does not require any human presence and observes every (clear) night.

Figure 3. The full Moon illuminates the TAROT observatory during a night in January 2007 when the great comet C/2006 P1 McNaught was visible with the naked eye.

TAROT Calern saw its first light in 1998. At about the same time, a rapid notification service profiting from all the internet capabilities, such as "sockets", was created. The Gamma-ray Coordinates Network[1] (GCN) promptly distributes the coordinates of GRBs detected by satellites to ground facilities within a second or less. From 1998 to 2001, 21 CGRO–BATSE GRBs were monitored by TAROT Calern. The High Energy Transient Explorer II (HETE II) and the International Gamma-Ray Astrophysics Laboratory (INTEGRAL) satellites sent the triggers for the period 2001–2004. Swift[2] was launched in 2004 and sends about 100 GRB alerts per year within an error box of 6 by 6 arcminutes. The X-ray telescope and the Ultra-violet/Optical Telescope (UVOT) visible camera onboard Swift can reduce this uncertainty to a few arcseconds.

The second TAROT instrument was installed at ESO La Silla Observatory in autumn 2006. It is located in the former GRB Monitoring System[3] (GMS) building at the foot of the hill that is home to the ESO 3.6-metre telescope (see Figures 2 and 3). Since 2006, the pair of TAROT telescopes has covered the two hemispheres. The rapidly slewing mount makes it possible to start the optical observations before the end of the high energy prompt emission. Since 2001, 120 GRB triggers have been observed by both TAROT instruments. Ten of them were optically detected by TAROT during the prompt high energy emission, giving very important science data. Another advantage of TAROT early observations of GRBs is the rapid determination of an accurate position of the optical counterpart. This position can then be sent to large facilities such as the VLT, allowing for spectroscopy while the source is still bright enough, with 97 % of the GRB redshifts determined less than one day after the trigger.

During the first few minutes after the GRB trigger, the optical emission can display large variations on a timescale of a second (or even less). Classical experiments record a set of images, typically of 5 to 10 seconds duration, during the first few minutes. However, with a readout time of not less than 5 seconds, that means a dead time of 50 %! It is then impossible to obtain a continuous light curve, and hence to draw meaningful conclusions about the prompt emission part of the light curve, or even for flares during the afterglow of the GRB. We implemented as a workaround a specific operating mode: the first image, which lasts 60 seconds, is trailed in such a way that each star occupies a small ten-pixel track. If an object, such as the GRB source, is rapidly variable, this will be reflected in the trail corresponding to its position, allowing the derivation of a continuous light curve with a time bin of 6 seconds (Figure 4). The comparison of the brightness variation in the optical with the flux variation in gamma-ray energy gives precious information about the emission processes (Gendre et al., 2012). To our knowledge TAROT is the only instrument able to provide continuous light curves of the GRB events, i.e. without any dead-time for the

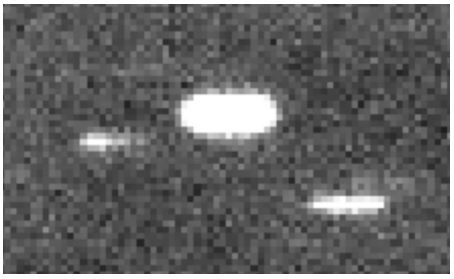

Figure 4. Trailed image of GRB 121024A. To obtain a time-resolved optical light curve during the first minute of the observation of a GRB, we trail the image such that each star occupies a small 10-pixel track on the frame. In this case TAROT observations started 45 seconds after Swift detected the event. The stars in the middle and right part of the image have a constant brightness during the exposure while the GRB optical counterpart is the left trail. At the start of the trail the brightness was R = 14.5 mag. At the end of the trail the magnitude had increased by 1.5 magnitudes only 60 seconds later! Just after this image, TAROT quickly provided the accurate position of the GRB allowing spectroscopy to be obtained with the VLT X-shooter spectrograph less than two hours later (Tanvir et al., GCNC 13890). The redshift of the source is 2.3, corresponding to an event that occurred 10.8 billion years ago.

first minute. Because of the very rapid intrinsic variability of GRBs, this feature is very important and allows us to draw significant conclusions by comparison between the gamma-ray signal and the optical emission as seen by TAROT.

Thanks to the presence of other experiments on the same site, namely GROND (Greiner et al., 2007) and REM (Chincarini et al., 2008) the ESO La Silla Observatory provides a unique set of instruments that work together to observe the optical counterparts of GRBs. TAROT and REM are rapid telescopes that can record the first few minutes of the GRB events. After this, the GROND instrument can detect very faint counterparts. During the last nine years (the SWIFT era) major advances in GRB science have come from using the data from these instruments.

Space environment, Solar System and stellar astronomy

Although GRBs are the primary objective of TAROT, because of the scarcity of their occurrence (an alert per week on average) and short duration, the time devoted to the observation of GRBs is short compared to the night-time duration. This allows ample time to study other objects which benefit from the high throughput and flexibility of TAROT. One of these programmes addresses the measurement of the pulsation periods of Galactic RR Lyrae stars. About 400 stars are monitored. The goal is to monitor period variations and study the Blazhko effect, a modulation of pulsation period and amplitude which is not yet understood (Figure 5). In 2007 we published a study on period variations on a time baseline exceeding a century (Le Borgne et al. 2007). More recently we published an analysis of the Blazhko effect for a large sample of RR Lyr stars (Le Borgne et al., 2012).

With the widespread use of space for many activities (telecommunications, remote sensing, meteorology, etc.), the issue of orbital debris has become very sensitive. Several satellites have been lost because of a collision with debris, often of centimetre size; and it is expected that the situation will become

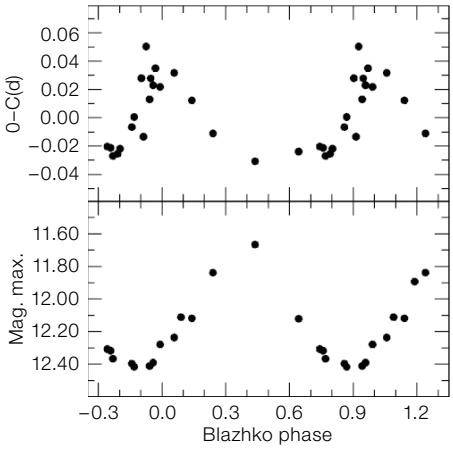

Figure 5. RR Lyrae stars in the Galaxy are observed by TAROT in order to understand the origin of the Blazhko effect. Each dot on the plot represents a light curve characteristic of the RR Lyr star XY Eri over a night (figure from Le Borgne et al., 2012). The Blazhko period is 41.22 days. The upper plot represents the delay between the times of the maximum of light and the mean value. The bottom plot represents the magnitude at the maximum of light against the Blazhko phase. This effect is monitored for 400 RR Lyrae stars.

worse within a short time, as more satellites are launched, and the risk of catastrophic collisions increases exponentially. Some orbits, like the geostationary orbit, have also become very crowded, implying that satellites have to be maintained in their orbital slot and their position has to be known with a very high accuracy. The use of radar has the advantage of allowing good precision for ranging, with the disadvantage of being less precise for the angular position; however radar measurement requires a lot of power for these high orbits. Small telescopes can give very accurate solutions. We use TAROT to monitor the position of several geostationary satellites with a high accuracy, and to survey the orbital debris. About 20 000 astrometric positions of geostationary satellites are gathered by TAROT each month. The process (observation, image processing for satellite extraction and astrometric reduction) is fully automated without any human in the loop.

Occultations of stars by minor planets provide a very accurate method to determine the dimensions of asteroids. However, even with a very precise prediction, it is impossible to forecast with enough accuracy the path of the shadow on the

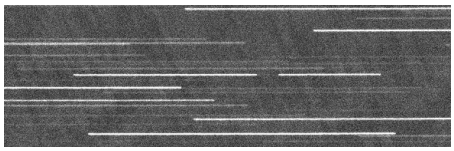

Figure 6. TAROT La Silla recorded this image without any diurnal motion and stars appear as trails. The trail in the centre of the image is of the star TYC 0611-00505-1 which was occulted by the asteroid (227) Philosophia for 6.41 seconds on 6 November 2011. This duration corresponds to an asteroid size of 74 kilometres.

Earth. TAROT is among the few telescopes that can easily monitor a star for a possible occultation. In practice we record all the predicted occultations that occur within less than 1000 kilometres from the telescope. Ninety-second images are taken with no sidereal motion. The star occulted appears as a trail with a gap if we have been lucky enough to catch the occultation (as was the case for the image shown in Figure 6). Sixty such occultations have been measured[4]. The duration of the gap can be converted to a length and gives constraints on the size of the minor planet. The date of the occultation also provides its astrometric position with an error generally less than 100 milliarcseconds.

Extragalactic studies

The discovery of supernovae (SNe) on the rise is a very important topic, both to understand the physics of the explosion and for their use in the determination of distances in the Universe. We decided to start a programme aimed at the earliest possible detection of nearby SNe. Four hundred nearby galaxies are monitored each night, and the same field is observed every three days. Two observation campaigns were carried out in 2007 and in 2012. Eight supernovae were discovered. The most interesting one of them was 2012fr, which exploded in the nearby spiral galaxy NGC 1365 (Figure 7). As the galaxy was observed in detail by the Hubble Space Telescope before the explosion, it is possible to constrain the brightness of the progenitor. SN 2012fr is a Type Ia supernova that was discovered by TAROT — La Silla less than two days after the explosion ignited, giving crucial data for models of supernovae. The light curve of SN 2012fr

Figure 7. TAROT image of the barred spiral galaxy NGC 1365 showing the supernova 2012fr discovered with TAROT as the blue source just above the nucleus of the galaxy. SN 2012fr was the brightest apparent supernova of 2012.

observed by TAROT shows that the decay in the *B*-band is very slow compared to the standard value. Investigations are continuing since the supernova will be observable for the whole of the year 2013. Everyone can contribute to this programme and has a chance to discover a supernova using the dedicated tool SN_TAROT[5].

Serendipitous science

We have launched a large scientific programme which consists of extracting the magnitudes of all the objects in all the images taken at both telescopes. For that purpose we have constructed an archive of the images which resides on the CADOR computer at the Observatoire de Haute-Provence, France. A first extraction was done in the period 2005–2007 using images of TAROT Calern only and a catalogue of 1175 new periodic variable stars was published (Damerdji et al., 2007). Now more than one million TAROT images are stored in the CADOR database. A major effort is underway to make a full analysis of the images, and to update the catalogue.

The Institut de Mécanique Celeste et de Calcul des Ephémerides (IMCCE) makes use of these images to extract the astrometric positions of known asteroids. In turn these positions are used by the SkYBOT virtual observatory service and 30 000 asteroid positions were extracted in 2012.

Education and Public Outreach

TAROT is also used by high school teachers who conduct science projects with their students. Examples of such programmes include the determination of the age and distance of star clusters using TAROT images, the monitoring of the position of satellites of giant planets to determine their mass, or the observation of supernovae to determine their type and distance from their light curve.

Prospects

Since 1998, the TAROT network of telescopes has contributed actively to GRB science. Its major contribution has been its unique capability to monitor the first few minutes of the optical emission. Its initial goals have been reached and even surpassed and 30 refereed papers have been published using TAROT data. Although TAROT will continue to work on this topic, we are also preparing actively for the new horizons of multi-messenger astronomy.

TAROT is already connected to the ANTARES experiment, a neutrino telescope consisting of lines of photomultipliers installed in the depths of the Mediterranean Sea. TAROT also participated in the 2010 campaign to follow up the triggers provided by the gravitational wave (GW) interferometers LIGO and VIRGO, and has successfully passed the blind tests (Abadie et al., 2012). The next generation of GW detectors will be ready in 2017 and TAROT will get ready to participate in this exciting new adventure. At the same time TAROT has been the seed for an effective automated network of heterogeneous telescopes around the world, and we are finding ways to complement and enhance the observation of the fast transient sky from the Earth.

Acknowledgements

The TAROT telescopes were built and are maintained thanks to the technical and financial support of Centre National de la Recherche Scientifique, Région Midi-Pyrénées, Institut National des Sciences de l'Univers (CNRS-INSU), of the Centre National d'Etudes Spatiales (CNES), and of the Observatoire de Haute-Provence (CNRS). TAROT acknowledges also the support of the Programme National Hautes Energies (PNHE) for collaborative research through the FIGARO grants. We thank the technical staff of various institutes (IRAP, OHP, DT-INSU and ARTEMIS) for their dedication and expertise in installing and maintaining TAROT, enabling a very high level of reliability.

References

Abadie, J. et al. 2012, A&A, 539, 124
Boër, M. et al. 2003, The Messenger, 113, 45
Chincarini, G. et al. 2008, The Messenger, 134, 30
Costa, E. et al. 1997, Nature, 387, 783
Damerdji, Y. et al. 2007, AJ, 133, 1470
Gehrels, N. & Mészáros, P. 2012, Science, 337, 932
Gendre, B. et al. 2012, ApJ, 748, 59
Greiner, J. et al. 2007, The Messenger, 130, 12
Klotz, A. et al. 2008, PASP, 120, 98
Le Borgne, J. F. et al. 2007, A&A, 476, 307
Le Borgne, J. F. et al. 2012, AJ, 144, 39
Rees, M. & Mészáros, P. 1992, MNRAS, 258, 41
van Paradijs, J. et al. 1997, Nature, 386, 686

Links

[1] Gamma-ray Coordinates Network: http://gcn.gsfc.nasa.gov
[2] Swift: https://heasarc.gsfc.nasa.gov/docs/swift/swiftsc.html
[3] GRB Monitoring System (GMS): http://www.eso.org/public/teles-instr/lasilla/grb.html
[4] Listing of TAROT minor planet occultations: http://www.euraster.net/tarot/
[5] Supernova hunting with SN_TAROT: http://cador.obs-hp.fr/sn_tarot/

Accurate Sky Continuum Subtraction with Fibre-fed Spectrographs

Yanbin Yang[1]
Myriam Rodrigues[2]
Mathieu Puech[1]
Hector Flores[1]
Frederic Royer[1]
Karen Disseau[1]
Thiago Gonçalves[3]
François Hammer[1]
Michele Cirasuolo[4]
Chris Evans[5]
Gianluca Li Causi[6]
Roberto Maiolino[7]
Claudio Melo[2]

[1] GEPI, Observatoire de Paris, CNRS, Université Paris Diderot, Meudon, France
[2] ESO
[3] Observatorio do Valongo, Brazil
[4] SUPA, Institute for Astronomy, University of Edinburgh, Royal Observatory of Edinburgh, United Kingdom
[5] UK Astronomy Technology Centre, Royal Observatory of Edinburgh, United Kingdom
[6] INAF–Osservatorio Astronomico di Roma, Italy
[7] Cavendish Laboratory, University of Cambridge, United Kingdom

Fibre-fed spectrographs now have throughputs equivalent to slit spectrographs. However, the sky subtraction accuracy that can be reached has often been pinpointed as one of the major issues associated with the use of fibres. Using technical time observations with FLAMES–GIRAFFE, two observing techniques, namely dual staring and cross beam-switching, were tested and the resulting sky subtraction accuracy reached in both cases was quantified. Results indicate that an accuracy of 0.6% on sky subtraction can be reached, provided that the cross beam-switching mode is used. This is very encouraging with regard to the detection of very faint sources with future fibre-fed spectrographs, such as VLT/MOONS or E-ELT/MOSAIC.

Why fibres could be an issue when observing faint targets

One of the key science drivers for the future instrumentation of the Very Large Telescope (VLT) and the European Extremely Large Telescope (E-ELT) is to study faint galaxies in the early Universe at very high redshifts (e.g., Navarro et al., 2010; Cirasuolo et al., 2011). The detection and spectroscopic follow-up of these sources will require an accurate and precise sky subtraction process. For instance, in its deepest observations, VLT/MOONS (Cirasuolo et al., 2011) will study sources as faint as H_{AB} = 25 mag in their continuum and emission lines in ~16 hours of integration, while E-ELT/MOSAIC (which is a concept design for a multi-object spectrograph [MOS] on the E-ELT; Evans et al., in prep.) will push this limit up to J/H_{AB} ~ 30 mag in emission, and up to J/H_{AB} ~ 27 mag for continuum and absorption line features. These spectral features will be typically observed between bright OH sky lines. However, the near-infrared (NIR) sky continuum background is found to be J/H_{AB} ~19–19.5 mag in dark sky conditions (Sullivan & Simcoe, 2012), i.e., hundreds to a thousand times brighter than the sources to be detected in the continuum. While the expected relatively bright emission lines with restframe equivalent widths larger than ~15 nm (e.g., Navarro et al., 2010) should easily emerge above this background, continuum and absorption line detections will clearly be hampered by possible systematic residual signal left by the sky subtraction process. For the future detection of such faint sources, it is therefore critical to check that sky subtraction techniques are accurate enough, i.e., that one can actually reach accuracies at a level of a few tenths of a percent at least.

In this respect, slit spectrographs have long been considered as much more accurate than fibre-fed spectrographs. This is mainly due to two different issues: (i) fibre-fed spectrographs, if not carefully designed, can suffer significant loss of light compared to slit spectrographs (resulting from, e.g., fibre cross-talk on the detector or focal ratio degradation [FRD] which results in a change of aperture at the output of the fibres); (ii) it is more difficult to achieve an accurate sky subtraction process with fibres than with slits. Recent developments in fibre technology and careful designs of fibre-fed spectrographs can control the issues of the first kind. For instance, good spacing of fibres on the detector can avoid significant cross-talk, while fibre-fed spectrographs can now potentially reach global throughputs similar to those of classical multi-slit spectrographs (e.g., Navarro et al., 2010).

However, issues related to the accuracy of sky subtraction remain, and this turns out to be particularly problematic when dealing with faint sources. Perhaps the two most important effects often associated with fibres, which further limit the accuracy of the sky subtraction compared to slits, are: (1) sky continuum variations between the position of the object and the position at which the sky is measured (due to the finite coverage of the fibres in the focal plane and the minimum practical distance of closest approach); and (2) variations in the fibre-to-fibre response (due, e.g., to point spread function [PSF] variations, fringing or FRD). We refer to, e.g., Sharp & Parkinson (2010) for a detailed description of the factors limiting the sky subtraction accuracy with fibres. After the E-ELT phase A instrumentation studies finished, we undertook to better characterise these two important potential caveats. We now report on some of the results obtained during the past two years.

Characterising the sky continuum spatial variations

The signal from the sky is difficult to predict and subtract in the NIR, mainly because of its strong variability in space and time. Variations of about 15% in amplitude are typical over spatial scales of a few degrees (e.g., Moreels et al., 2008). These variations are clearly dominated by the flux fluctuations of the bright and numerous OH emission lines, and, in the second order, by the intensity variations of absorption bands produced by molecules of water and other components of the Earth's atmosphere. Between these telluric emission and absorption lines, the sky signal has a continuum level about ~19–19.5 mag_{AB} in the *J*/*H* bands, the origin of which is still poorly understood. It could be due to a pseudo-continuum associated with instrumental residuals, e.g., diffuse scattered light from the wings of bright emission lines within the spectrograph (Trinh et al., 2013), or to continuum radiation from

constituents of the atmosphere. To our knowledge, the spatial and temporal variability of this sky continuum as a function of both space and time has never been characterised.

We first investigated these issues using archival VLT/FORS2 narrowband imaging and spectroscopy data. Over timescales of a few tens of minutes, Puech et al. (2012) and Yang et al. (2012) found that the sky continuum background exhibits spatial variations over scales from ~ 10 to ~ 150 arcseconds, with total amplitudes below 0.5 % of the mean sky background. At scales of ~ 10 arcseconds or below (on which the sky is likely to be measured with future fibre-fed spectrographs), the amplitude of the variations is found to be ~ 0.3–0.7 %. Note that this should still be considered as an upper limit to real sky continuum variations, since scattered light and noise variance can be difficult to mitigate in such low signal-to-noise data. Regardless, this is a very encouraging result, which suggests that sky background subtraction can, in principle, be achieved with an accuracy of a few tenths of a percent.

Testing sky subtraction with cross beam switching observations

Reaching sub-percent accuracy on sky subtraction still requires that the variations in fibre-to-fibre response are dealt with. For this purpose we requested ESO technical time on FLAMES–GIRAFFE, which is the ESO optical workhorse multi-object fibre-fed instrument at VLT/UT2. Such tests reveal that accuracies of few tenths of a percent can indeed be reached, provided that a cross beam-switching observing sequence is used (see Figure 1). In the following, we describe the observations conducted and the results obtained.

We undertook technical observation with FLAMES–GIRAFFE on 8 March 2012, using the Medusa mode with clear conditions and a seeing of ~ 0.9 arcseconds. The fibres were distributed over a 20 by 20 arcminute region in the zCOSMOS field (Lilly et al., 2007). Seventy fibres were distributed in pairs separated by 12 arcseconds and oriented along the north–south axis, as illustrated in Figure 1. Three

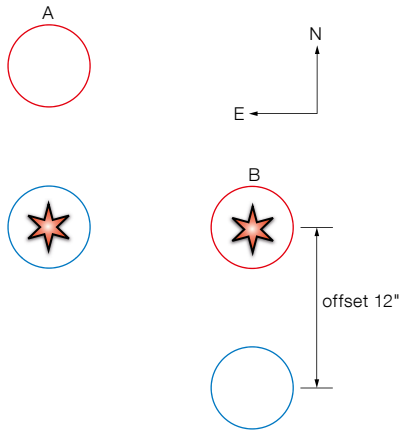

Figure 1. Illustration of cross beam-switching observations. The astrophysical object of interest is represented as a star. The fibres are positioned in pairs in the focal plane, with distances of 12 arcseconds between the two fibres of each pair along the north–south axis. Such a pair is represented by red and blue circles. The observing sequence consists of dithering the telescope from position A to position B by 12 arcseconds such that the object (and the sky) is always observed within one of the two fibres of a given pair.

of these pairs were “pure sky”, meaning that no object was observed in any pair of fibres. Preliminary results from these three pairs were presented in Rodrigues et al. (2012).

The LR8 GIRAFFE setup, which covers 820–940 nm with a spectral resolution of R = 6500, was chosen to obtain spectra at NIR wavelengths. The target field was observed at low airmass (< 1.2), i.e., when it was relatively close to the meridian with an hour angle of less than ~ 30 minutes. During the observations, the Moon was located ~ 28 degrees away from the target field, contributing about 50 % to the sky continuum background flux. The total continuum background of the observations reaches m_{AB} ~ 19.7 mag arcsecond^{-2}, which is very similar to the J-band sky continuum brightness in dark conditions (Sullivan & Simcoe, 2012) and therefore particularly well-suited to our purposes.

The observations were carried out using a cross beam-switching configuration in which the telescope was offset by 12 arcseconds along the north–south axis three times in a row (see Figure 1), resulting in an A–B–A–B–A–B sequence. FLAMES does not have a template for cross beam-switching observations, so the telescope guiding had to be switched off during all the dithered B exposures. In principle, the pointing error during offsets is better than 0.2 arcseconds, which is much smaller than the diameter of the fibres (1.2 arcseconds). However, in order to prevent any risk of significant misalignments between the objects and the fibres during the dithered B exposures, an A–B–A–B-like sequence was preferred instead of the usual A–B–B–A-like sequence. This preserved the signal-to-noise ratio and only resulted in larger overheads. Each individual (A or B) exposure was ten minutes. The three consecutive A–B sequences obtained represent a total effective exposure time of one hour, immediately after which attached flat-field exposures were acquired.

Data analysis and results

Basic reduction steps were performed using the ESO pipeline (bias correction, internal calibration lamp flat-fielding, wavelength calibration and extraction of 1D spectra). We focused on the sky continuum background since targets will be observed between the sky emission and strong telluric lines (e.g., Vacca et al., 2003; Davies et al., 2007). Seven spectral regions free of sky emission and absorption lines were defined (see Figure 2) to test the accuracy of different sky subtraction strategies. To increase the statistics, but limit the impact of the object spectrum, we limited the analysis to 15 pairs with object I_{AB}-band magnitudes fainter than 21. The mean magnitude of these 15 objects is found to be I_{AB} = 21.88 mag, which corresponds to a continuum flux that is ~ 7 times fainter than the contribution from the sky continuum. To compare the sky continuum subtraction accuracy reached using cross beam-switching observations, we also reduced the data in order to mimic a simpler staring mode observing strategy. Both observing and reduction methods are detailed below.

In staring mode observations, an object and the nearby sky (12 arcseconds away in the present case) are observed with a pair of fibres simultaneously. For each object in the sample, we derived two spectra by combining the three A exposures and the three B exposures,

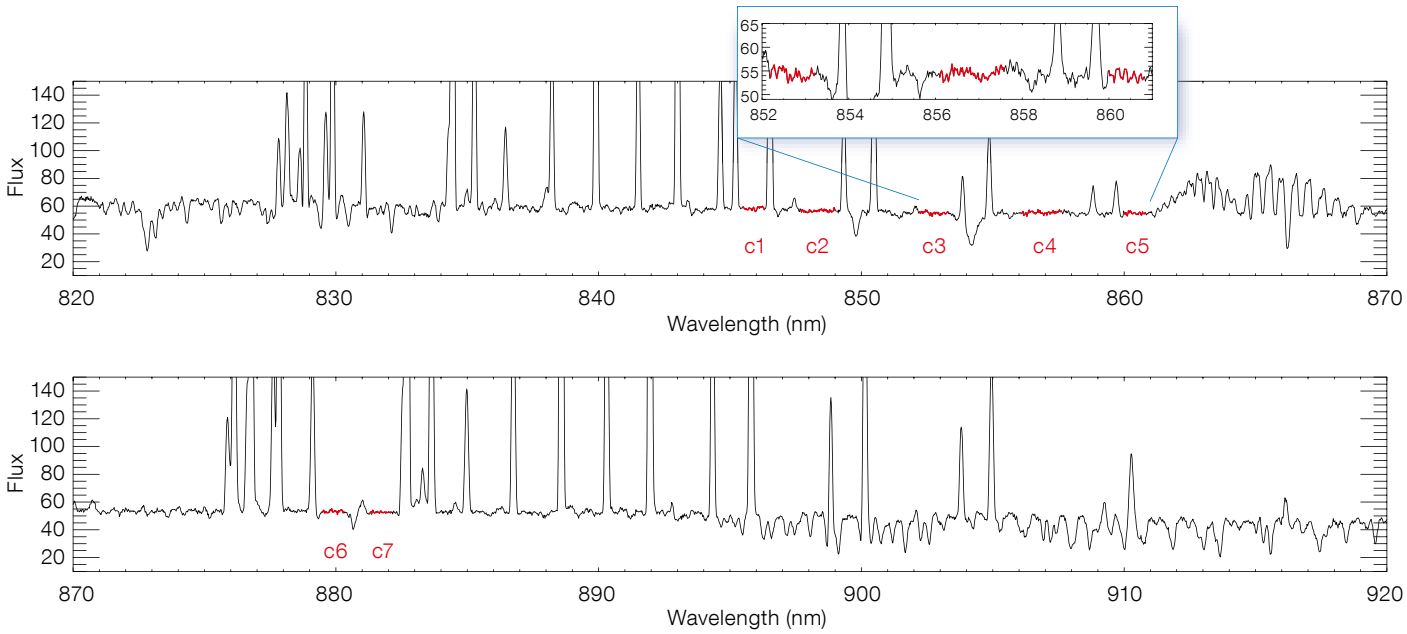

Figure 2. Sky spectrum from 820 to 920 nm obtained after combining 72 sky fibres. OH emission lines and atmospheric absorptions, i.e., telluric lines, can be seen almost everywhere. Only a few relatively clean continuum regimes are left, such as the red regions marked as c1 to c7, which are selected for further analysis.

respectively. The resulting exposure time of each spectrum is 30 minutes. Here, there is no point in combining all A and B exposures together since, by definition, in staring mode the sky is sampled on only one side of the object, and the object and sky are observed with different fibres which would lead to large residuals. Thus, we simply subtracted the integrated B spectrum from the integrated A spectrum. Since the objects have fluxes that are significantly fainter than that of the sky continuum (see above), the resulting difference can be considered as a first-order estimate of the residuals from the sky subtraction process.

In cross beam-switching mode, the telescope is dithered by 12 arcseconds along the north–south axis between the A and B positions. During the three consecutive A–B sequences, a given object is always observed by one of the fibres of the pairs alternately. Within a single A–B sequence, the object spectrum can be extracted twice (once in A and once in B) and subtracted one from another. In contrast to the staring mode, one can combine all six exposures to produce a spectrum with a one-hour integration. In cross beam-switching mode, object and sky are indeed observed by the same fibre but at different times, and the sky is sampled at both sides around the objects. Finally, if one combines all the exposures of all the objects together, one can actually simulate the result of a 15-hour on-sky spectrum. Combining all the measurements in the seven distinct spectral windows can mimic a simulated integration time of up to 105 hours. This is sufficiently long so as to sample deep integration times for future VLT or E-ELT observations (i.e., of a few tens of hours). In the absence of any residual systematic effect, one would expect that the resulting signal-to-noise ratio of the combined spectrum is reduced by a factor 3.8 (combining the 15 exposures together) and 10 (combining all the exposures of all objects together), respectively.

For each exposure of all objects, we estimated in each spectral window the residual local error after sky continuum subtraction (i.e., the accuracy of sky subtraction) as the relative mean between the object and sky spectra (divided by the mean sky). As we argued, considering all such measurements for all exposures of all objects in the sample simulates a 105-hour integration, providing us with well-defined statistics for measuring the mean expected accuracy as well as its associated uncertainty, as shown in Figure 3. We found in this case a mean accuracy of 0.6 ± 0.2 %. In comparison, the accuracy is degraded by a factor of ~ 10 when using the simple staring-mode observations. This confirms the preliminary analysis conducted by Rodrigues et al. (2012), i.e., that cross beam-switching observations allow us to reach sky subtraction accuracies of a few tenths of a percent.

Reaching the noise floor

We also investigated the exposure time needed to reach the noise floor at which the signal-to-noise ratio of the observations becomes limited by systematic effects associated to sky continuum

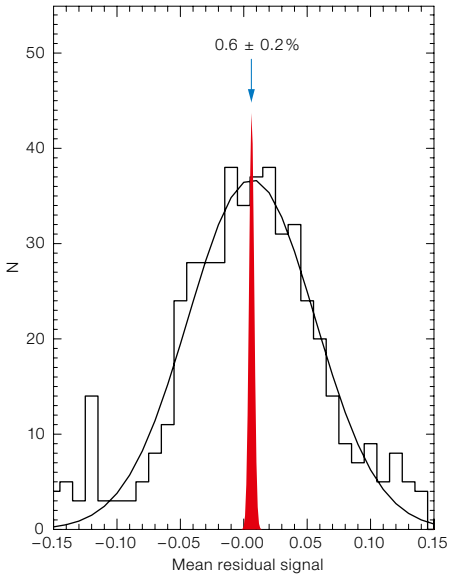

Figure 3. Histogram of the mean residual signal measured in each spectral window of all exposures of all objects observed with FLAMES–GIRAFFE. The mean value estimates the mean residual error signal, i.e., the accuracy of the sky continuum subtraction, obtained with simulated 105-hour long exposures. The red region represents the uncertainty associated with this value, which was derived using the standard error of the mean, i.e., as the standard deviation of the distribution divided by the square root of the sample size.

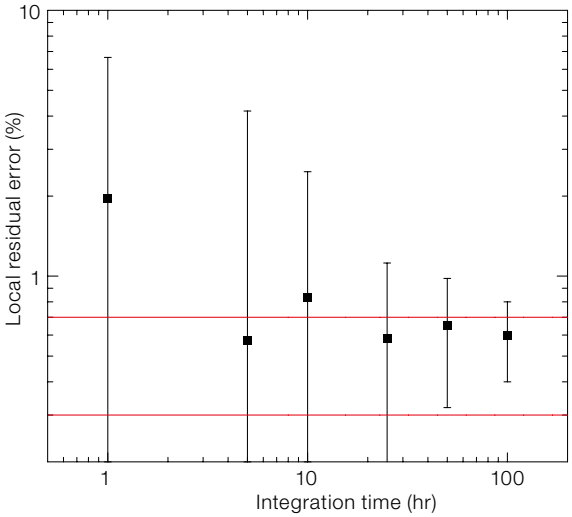

Figure 4. Local residual error as a function of integration time. The black points, with error bars, illustrate a decrease with the square root of integration time. The two horizontal red lines represent the range of variations found at ~ 10 arcsecond scales in the sky continuum background from Puech et al. (2012) and Yang et al. (2012).

subtraction inaccuracies. For this, we repeated the above measurements in samples of different sizes, which simulate different integration times, as argued above. Results are shown in Figure 4. At short integration times, the local residual error is dominated by random errors associated with the photon noise. It is expected from simple Poisson statistics that this error decreases as the square root of the integration time, until it reaches a floor (see Sharp & Parkinson, 2010). Given the limited size of our sample, it is difficult to measure such a decrease precisely, but a gradual decrease followed by a floor can indeed be seen in Figure 4. This floor is reached after 10–25 hours of integration at a value of 0.6 %. At such large integration times, the local residual error starts to be dominated by systematic effects from the sky continuum subtraction.

The trend shown in Figure 4 is similar to that found by Sharp & Parkinson (2010) at 600 nm, with a ~ 0.3% floor after 70–100 hours of integration. Besides, it is interesting to note that the 0.6 % floor in residual local error is very close to the measured variations of the sky continuum background obtained by Puech et al. (2012) and Yang et al. (2012), which range between ~ 0.3 and 0.7 %. This could indicate that long-exposure observations can really remove most of the instrumental inaccuracies and reach the physical limit due to sky continuum variations. The 0.3 % floor found by Sharp & Parkinson (2010) could be due to the smaller variations in the 600 nm sky continuum, compared to the wavelengths around 900 nm that we are probing here.

It is important to recall that the results reported here were obtained on 1D spectra with non-optimal conditions. It is likely that using more advanced procedures in the data reduction (see Sharp & Parkinson, 2010) and with more control over the instrument design regarding the potential sources of inaccuracies detailed above, one might be able to lower the floor at which signal-to-noise ratio is limited by such systematic effects, and possibly to shorter integration times. Moreover, these results support the idea that controlling and measuring instrumental scattered light would remain the main obstacle to accurate spectroscopy of faint sources. We argued above that these results should apply up to *J*-band, but it will be important to confirm these results and characterise the sky continuum variations at even longer wavelengths, where the impact of scattered light keeps increasing.

The results reported here strongly suggest that the issue of the sky continuum subtraction is not a show-stopper for the study of very faint sources with fibre-fed spectrographs. Given the flexibility of these systems, it is likely that they will play a very important scientific role in the future generation of multi-object instruments such as MOONS for the VLT (Cirasuolo et al., 2011) or MOSAIC for the E-ELT (Evans et al., in prep.).

References

Cirasuolo, M. et al. 2011, The Messenger, 145, 11
Davies, R. I. 2007, MNRAS, 375, 1099
Lilly, S. et al. 2007, ApJS, 172, 70
Moreels, G. et al. 2008, Exp. Astr., 22, 87
Navarro, R. et al. 2010, Proc. SPIE, 7735, 88
Puech, M. et al. 2012, Proc. SPIE, 8446, 7
Rodrigues, M. et al. 2012, Proc. SPIE, 8450, 3
Sharp, R. & Parkinson, H. 2010, MNRAS, 408, 2495
Sullivan, P. W. & Simcoe, R. A. 2012, PASP, 124, 1336
Trinh, C. et al. 2013, MNRAS, submitted, astro-ph/1301.0326
Vacca, W. D. et al. 2003, PASP, 115, 389
Wyse, R. F. G. & Gilmore, G. 1992, MNRAS, 257, 1
Yang, Y. B. et al. 2012, Proc. SPIE, 8446, 7

Delivery of the Second Generation VLT Secondary Mirror (M2) Unit to ESO

Robin Arsenault[1]
Elise Vernet[1]
Pierre-Yves Madec[1]
Jean-Louis Lizon[1]
Philippe Duhoux[1]
Ralf Conzelmann[1]
Norbert Hubin[1]
Roberto Biasi[2]
Mario Andrighettoni[2]
Gerald Angerer[2]
Dietriech Pescoller[2]
Chris Mair[2]
Federico Picin[2]
Daniele Gallieni[3]
Paolo Lazzarini[3]
Enzo Anaclerio[3]
Marco Mantegazza[3]
Luigi Fumi[4]
Armando Riccardi[4]
Runa Briguglio[4]
Florence Poutriquet[5]
Eric Ruch[5]
André Rinchet[5]
Jean-François Carré[5]
Denis Fappani[6]

[1] ESO
[2] Microgate, Bolzano, Italy
[3] ADS International, Valmadrera, Italy
[4] Osservatorio Astrofisico di Arcetri, Florence, Italy
[5] REOSC, St-Pierre-du-Perray, France
[6] SESO, Aix-en-Provence, France

The deformable secondary mirror (DSM), one of the key systems of the VLT Adaptive Optics Facility (AOF), has been delivered to ESO. It has been fully qualified in standalone mode and has successfully passed the technical acceptance Europe. Recently it was installed on ASSIST, the test bench for the AOF, and will undergo optical tests, which will complete its preliminary acceptance in Europe. With its 1170 actuators and 1.1-metre thin-shell mirror, it constitutes the largest adaptive optics mirror ever produced. The DSM constitutes a fine accomplishment by European industry and is set to become the "flagship" of the AOF on Paranal.

The Adaptive Optics Facility (AOF) is intended to transform the Very Large Telescope (VLT) Unit Telescope 4 (UT4) into an adaptive telescope. This is accomplished by replacing the conventional secondary (M2) mirror with an adaptive secondary, implementing the Four Laser Guide Star Facility (4LGSF) and installing adaptive optics (AO) modules on the various foci. Until recently, the AO modules consisted of GRAAL (Ground Layer Adaptive optics Assisted by Lasers; Paufique et al., 2012) for HAWK-I and GALACSI (Ground Atmospheric Layer Adaptive Corrector for Spectroscopic Imaging; Stroebele et al., 2012) for the Multi-Unit Spectroscopic Explorer (MUSE), but lately the Enhanced Resolution Imager and Spectrograph (ERIS) project has been launched and ERIS will be installed on the Cassegrain focus of UT4 with an upgraded version of the SPIFFI near-infrared imaging spectrograph. With this last addition, all instruments on UT4 will thus be optimised for use with the 4LGSF and the deformable secondary mirror.

There has been major progress since the last report in *The Messenger* (Arsenault et al., 2010), as most systems have now been delivered to ESO Garching and integrated.

The deformable secondary mirror

The DSM was delivered to Garching on 6 December 2012. This represents a major milestone for the AOF. It should be recalled that initial efforts towards the development of the DSM and thin-shell mirrors were initiated at ESO as early as 2004 in the framework of Opticon research and development efforts. This delivery initiates the start of the AOF system tests in Garching which will last for the next 18 to 24 months.

Microgate and its partner company ADS were involved early on in the project. A feasibility study was initiated in 2004 and concluded in August 2005. A single source contract was then granted to Microgate for preliminary and final design studies, which was concluded in December 2007. A few months later, the present contract was awarded for the manufacture of the DSM.

The thin-shell mirror development followed a similar time frame. Unfortunately, Opticon funded efforts were unsuccessful and Microgate had to resort to another supplier for the manufacture of the first science shell. REOSC was awarded the contract by Microgate in August 2009 and the mirror delivery took place in January 2012. The shell has since been furbished with magnets, coated and integrated into the DSM. Following the delivery of the first shell, ESO placed a contract with REOSC for a second, spare, thin shell.

The DSM system and its design have been presented in a number of papers: on AOF manufacture (Arsenault et al., 2010); integration and electromechanical testing (Biasi et al., 2012); stress polishing of the thin shell (Hugot et al., 2011); and in a progress report (Arsenault et al., 2012). We will focus here on the performance of the system.

DSM high-level functionality

The DSM is contained in a complete new M2 unit that will replace the actual Dornier M2 unit of UT4. The hub structure implements the same interface as the existing one for the telescope spider and the current Laser Guide Star Facility launch telescope. The latter will be reinstalled on the new M2 unit.

The M2 mirror surface is defined by the thin-shell mirror, 1120 mm in diameter and 2 mm thick, and the reference body, which defines a reference surface for the back (concave side) of the thin shell (Figure 1). Both are made of Zerodur. The reference body (manufactured by SESO, France) is a thick optical piece, lightweighted, with hole patterns to allow the passage of the 1170 voice coil actuators. These are mounted on the cold plate and apply forces on 1170 corresponding magnets glued on the back face of the thin shell. Metallic coatings on the shell back face and the front face of the reference body act as capacitive sensors used to measure the gap between both.

In non-adaptive optics mode, a constant command is applied to the 1170 actuators to give to the thin shell the VLT M2 prescription figure. This figure will have been calibrated on the ASSIST test bench. The command is applied at a sampling rate of 80 kHz, the internal

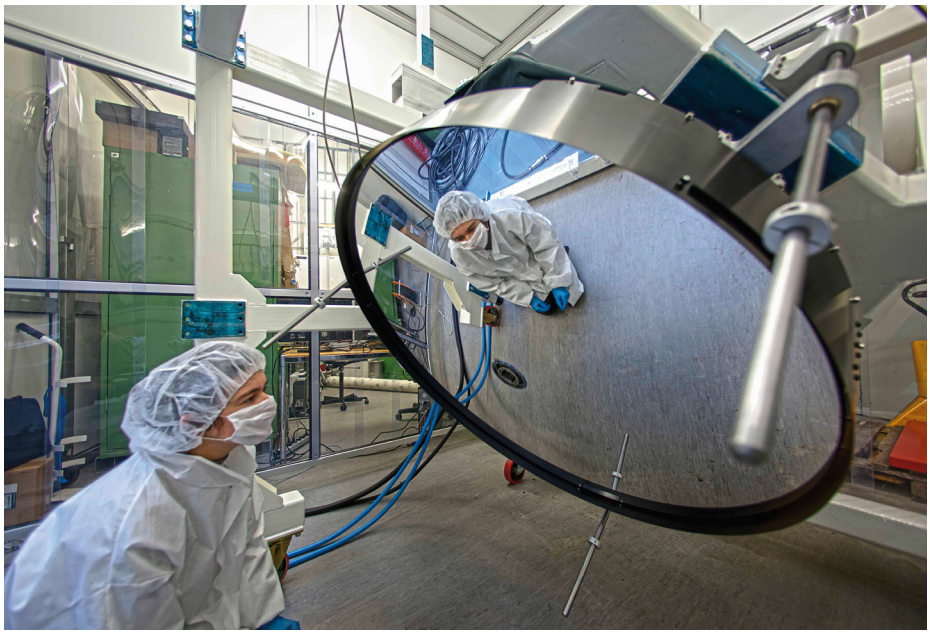

Figure 1. The deformable secondary mirror in its test stand. In operation the thin-shell mirror is held by the actuators with a gap of 65 µm between the shell back face and the reference body front face. The black metallic structure surrounding the mirror is called the "EMC skirt" and shields the system from electromagnetic interference.

control loop frequency, but kept constant. The result for the telescope user is an equivalent pseudo-rigid M2 mirror like the current Dornier mirror.

The M2 local control unit (LCU) software (and the whole system) have been developed with the intention of minimising changes in non-adaptive optics mode, so that for users and telescope operators, the mirror is set up like a Dornier M2 unit. The same adjustment possibilities are offered: two focal stations — Cassegrain and Nasmyth, focusing and centering (i.e., rotation of the mirror around its centre of curvature). The required motions are performed with a hexapod, but this is transparent to the user. The active optics of the VLT functions in exactly the same way as with the Dornier M2.

The full potential of the DSM is unleashed in adaptive optics mode: here the 1170 actuators are used to change the shape of the mirror in order to correct the atmospheric turbulence. A ± 1 N force can be applied to each actuator, which provides considerable stroke for the low order modes (tip, focus and astigmatism) while much more force is required for the high order modes, which can be very stiff. The shell is operated at a gap of ~ 65 µm; given the constraint that this gap should not be below ~ 30 µm, to ensure proper capacitive readout, this means that some ± 30–40 µm stroke is available for turbulence correction (for reference, a typical piezoelectric stack deformable mirror provides less than 10 µm total stroke). The internal control loop of the DSM operates with a given set of force/gap for each actuator. This set of gaps is updated by the adaptive optics real-time computers of GRAAL and GALACSI, and in the future, ERIS, using the Standard Platform for Adaptive optics Real Time Applications (SPARTA) architecture. The difference from a piezoelectric stack mirror, for instance, is that the DSM internal control loop manages the dynamics of the mirror in an optimal fashion. At the next iteration the SPARTA real-time computer can send a new command knowing that the previous one has been executed without time delay, creep or hysteresis.

The SPARTA real-time computers implement various control schemes depending on the instrument that is being fed: ground layer AO correction (GLAO); laser tomography AO correction (LTAO), both with laser guide stars; and classical on-axis natural guide star AO correction (NGAO). The set of modes to be controlled can also be optimised to zonal control

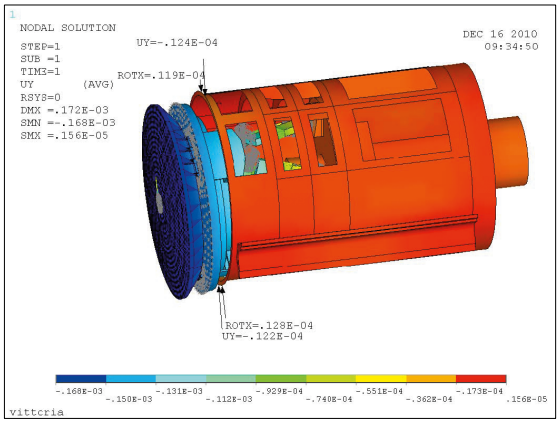

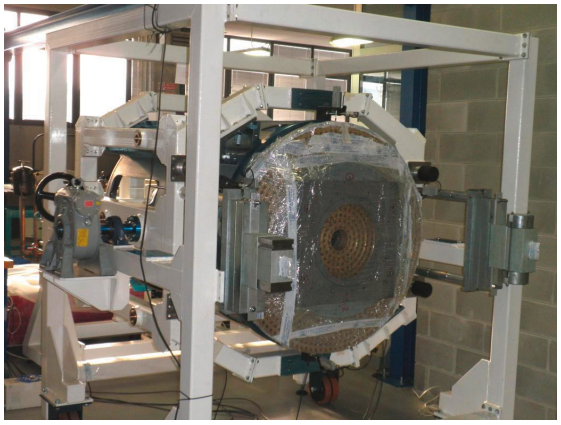

Figure 2. Finite element modelling of the complete DSM shown on the left. It is used as a baseline to compare with the experimental results. On the right, the hub with dummy weights and external encoders to measure flexure. The hub integration and service stand allows the inclination of the hub to be varied to characterise the flexure at the level of the reference body for different orientations. The results of the flexure campaign confirmed the system rigidity at 150 N/mm.

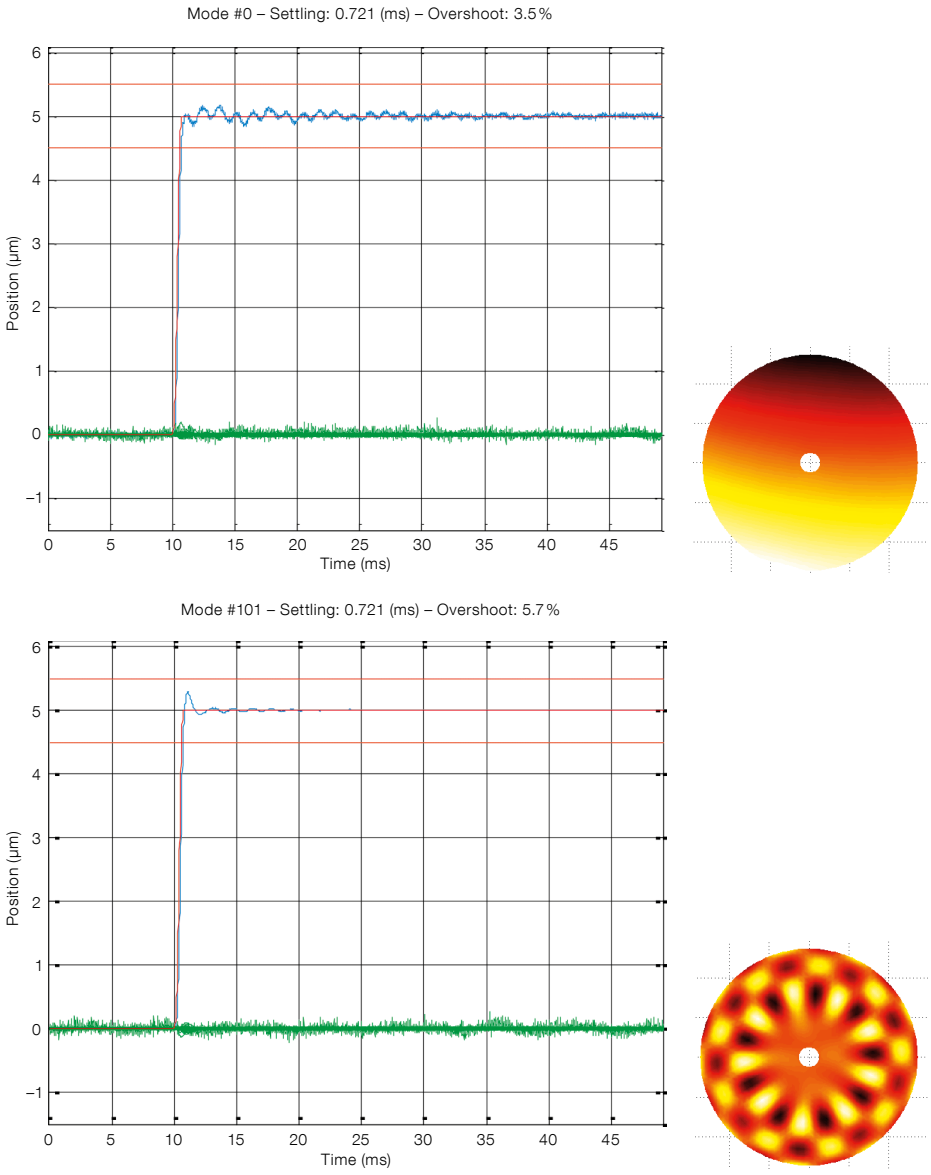

Figure 3. Response time performance for tilt (upper) and the natural eigenvector mode 101 (lower). The control parameters have been adjusted so that all modes have similar dynamical properties. The specification was 1.2 milliseconds at 90% of command and less than 10% overshoot; all modes are below 0.7 milliseconds. The stiffer the mode (i.e. mode 101), the higher its resonance frequency; thus the bigger challenge is for the low order modes such as tilt, focus, astigmatism, etc.

(individual actuators), stiffness modes (natural modes of the DSM) or Karhunen–Loeve, or any set defined by the AO specialist. Furthermore, an online algorithm monitors the interaction matrix during the observation in order to identify mis-registration between the DSM and the wavefront sensors and to update the command matrix to optimise the correction.

A subtle consequence of using an adaptive secondary is that the active optics of the VLT will be inoperative. The active optics Shack–Hartmann sensor is blind to the telescope aberrations since it is fed after the DSM and thus sees a perfectly corrected wavefront. In other words, the telescope internal aberrations and misalignments are corrected by the DSM. The strategy is thus to offload the quasi-static aberration seen on the DSM directly to the M1 mirror actuators. Note that the coma correction that is done by the centering correction of the M2 unit is the same, whether in non-adaptive or adaptive optics mode.

DSM unit system tests

Testing of the DSM started a while ago at subsystem level. The Integration Progress Review was held in May 2011 and one complete week was spent at ADS and Microgate to inspect all the hardware produced by this time, before the integration of the whole DSM system. The aim was to ensure that all components were validated before this final step. Both contractors developed custom tools and test setups for this phase of the project.

At Microgate, where the electronics and software were developed, the corresponding subsystems were inspected and tested: electronic control boards, actuators, racks and software. A massive amount of data was acquired, which has been reviewed by ESO, and will be built into the system as internal calibration data used during system operation. Mechanical subsystems were also tested and inspected at the ADS premises. The hexapod motion characteristics were tested: centering, focusing, change of focal station (Nasmyth to Cassegrain), full range, positioning accuracy and motion cross-coupling. Particular care was taken to assess the mechanical rigidity of the system (see Figure 2).

Performance

The most impressive results of the whole system test campaign are probably the critical performance specifications, which have all been met. Among these are: the residual wavefront error after adaptive optics correction, the response time (see Figure 3), the chopping stroke and its response time. The main verification of the DSM performance is the follow-up error test. Numerical phase screens have

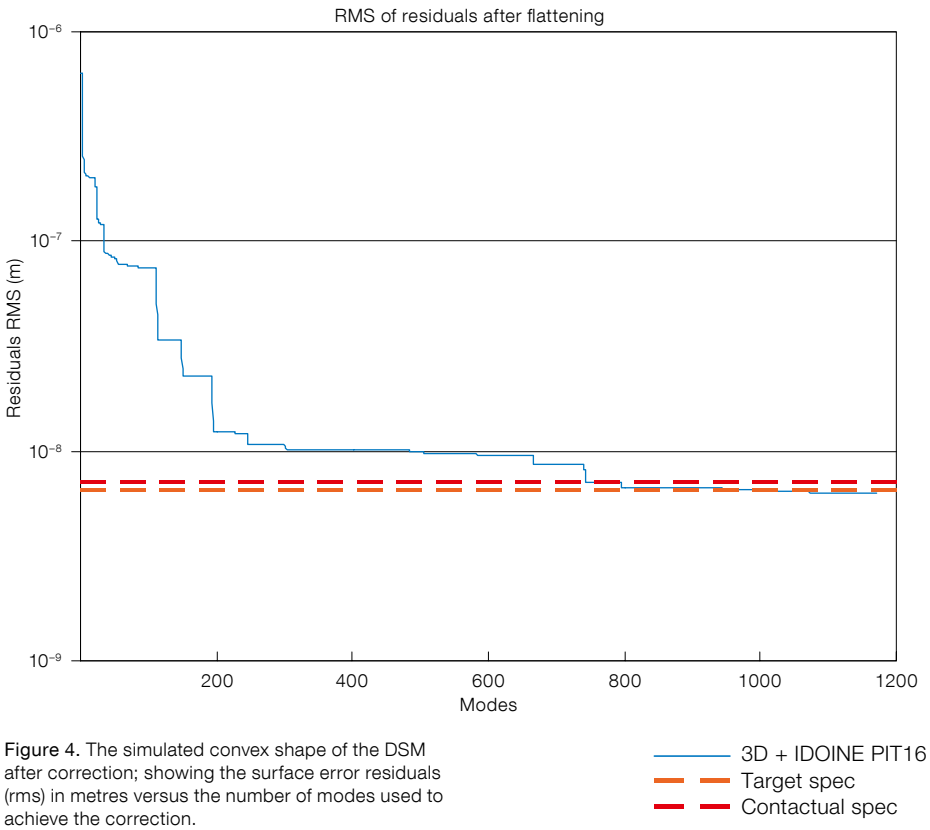

Figure 4. The simulated convex shape of the DSM after correction; showing the surface error residuals (rms) in metres versus the number of modes used to achieve the correction.

been simulated at ESO for a calibrated condition of 1.5 arcseconds at a wavelength of 0.5 µm, 20 degrees elevation angle and 1000-mode correction. These are quite demanding conditions. From these phase screens one can easily infer the shape that must be taken by the DSM to correct the wavefront. A file containing the time history for all actuators has been provided to Microgate.

The test then proceeds by switching on the DSM and fooling it into believing that the capacitive sensors measure the distances in the time history file. The internal control loop then corrects these offsets. The system measures the capacitive sensor signals versus time and makes a few simple assumptions about time delay. At each calculation cycle, a delta can be measured between the real mirror position and the sent perturbation. This constitutes the main part of the error signal. If the error due to the high order modes not corrected by the DSM is added to this delta, then the result gives the performance of the system in terms of residual root mean square (rms) wavefront error. The result of this test gives 131.5 nm rms wavefront error while the specification requests 149 nm rms. The internal control loop of the DSM (between coils and capacitive sensors) represents a huge asset at the time of testing as it allows the subsystem to be fully qualified before it is integrated into the AOF with guide stars, external real-time computer and optical Shack–Hartman sensors.

Thin-shell mirror

The convex face of the thin shell is polished to the nominal M2 optical prescription and then the optical piece is thinned to the 2 mm nominal thickness. The defects in the convex shape can be relatively high (several micrometres) if they represent low order deformations; but these can then easily be corrected by the actuators of the DSM. A computer program has been developed by the Osservatorio Astrofisico di Arcetri in order to assess the forces required to obtain the M2 nominal prescription figure from the actual convex shape. The specification to be fulfilled by the optical supplier is then to provide a convex face that requires less than 0.1 N (10 % of full range) to bring the shell to the 8 nm rms surface error.

The first science shell reached the specified quality requirement: the convex shape could be brought to 8 nm rms surface error by correcting ~ 800 modes and this required ~ 0.1 N force (see Figure 4). If all the 1170 modes are corrected, the surface error is reduced further, but higher forces are required.

The next challenge was the thinning and accurate surfacing of the back face of the thin shell. In order to ensure good dynamical behaviour (response time, electronic damping and homogeneous and low-noise capacitive sensor readout), the gap between the reference body and thin shell must be homogeneous. The criteria is thus to thin the shell to a homogeneous thickness. Here there is both a constraint from the polishing and also from the measurement: the acoustic devices used to measure the thickness, although they possess sufficient accuracy, are somewhat sensitive and measurements can easily be degraded by conditions (surface cleanliness, sensor/surface interface, surface roughness, parasitic devices running simultaneously, etc.).

Despite these difficulties the first shell was realised to specification and delivered to ADS in January 2012. Following this, an aluminium coating was applied to the back face, leaving 1170 circular apertures for the gluing of the magnets (Figure 5). This coating has essentially an electrical purpose. After the gluing of all the magnets, the optical coating is deposited on the convex side.

The last integration step is to glue the central membrane onto the shell; this is done in the setup with the shell held up by the actuators and kept in position for several hours while the glue is curing. Note that the membrane allows tip and tilt and piston motion (along the optical axis) of the shell, while restraining motion perpendicular to the optical axis.

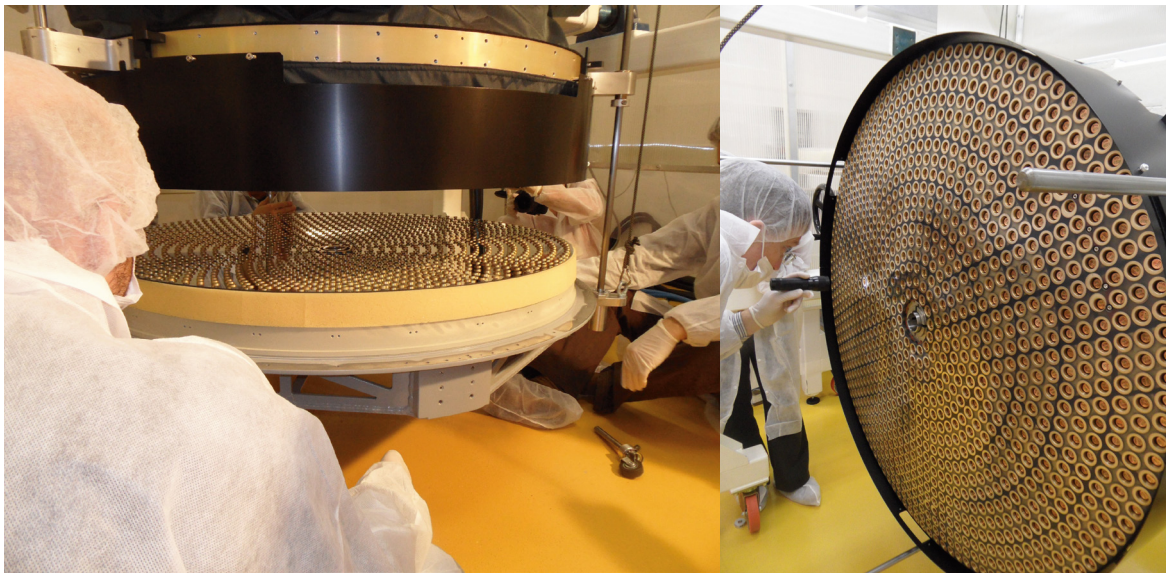

Figure 5. Left: The thin shell being dismounted. The magnets glued to the back face are visible. Right: The front face of the reference body. The 1170 recesses for the magnets surrounded by the chemically deposited rings of silver coating (for capacitive sensing) can be clearly seen. The copper parts inside the reference body recesses are the caps on top of the voice coil actuators.

ESO has awarded a contract to REOSC for a second science shell that will be used as a spare. The latter will be fully characterised before the DSM is shipped to Chile for commissioning.

Handling and maintenance

A fear often expressed in dealing with such a fragile thin-shell mirror is the danger of hosting it in a VLT system. The concern is certainly justified, but the suppliers have taken particular care in developing detailed procedures and a set of handling tools to ensure that any handling will be conducted under the best and safest conditions. For instance, a multi-purpose container has been developed for the thin shell. Its design is the result of years of experience with previous deformable thin-shell mirrors and detailed finite element modelling (FEM). The concept consists of two halves holding the thin shell in a sandwich and the spacers between these two halves are calibrated to exert a pre-defined load on the shell.

The shell transport box (STB; Figure 6, left) fulfils several functions as well as transport of the shell: the lower (concave) half is used as receptacle for the shell removal and installation on the DSM; the complete STB with shell can be suspended from a reverse “U” shape handling device allowing the shell to be flipped; and the convex half of the shell can be used as a “coating body”.

A similar philosophy has been applied to the DSM system itself. Other tools enable various maintenance operations: a test stand has been provided for the hub alone or with the DSM; another stand has been provided for the DSM assembly alone (Figure 6, right); a stand hosts the hexapod when it is removed from the hub; and dummy weights are provided to replace missing components, allowing continual use of the same tools in a balanced configuration.

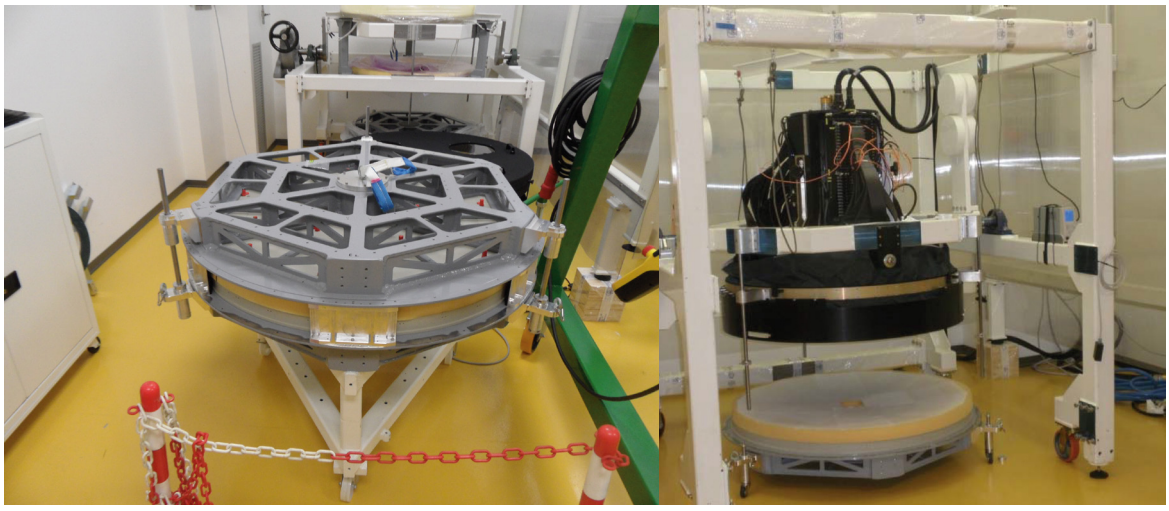

Figure 6. Left: the shell transport box, which is the DSM multi-purpose handling and protection equipment, is shown. Right: the DSM test stand allows the DSM, with its electronics, to be fully operational in the laboratory.

Next phases and key milestones for the AOF

Now that the DSM has been successfully delivered, the subsequent sequence of events is straightforward. The AOF project has now reached a stage where most of the tasks are now sequential and on the critical path. In January 2013 the DSM was mounted on ASSIST (Stuik et al., 2012). There a team from Arcetri Observatory and ESO will fully characterise the DSM optically. This phase will last around four months and is still the responsibility of the contractor.

ASSIST, with its 1.7-metre main mirror provides a complete optical setup for the DSM; no simple task for a convex secondary mirror (Figure 7). With the use of a fast interferometer, the DSM will first be characterised optically. For the other tests with GRAAL and GALACSI, the input module of ASSIST simulates a constellation of sources, natural and laser guide stars defocused and aberrated by calibrated turbulence. The AO modules can be mounted on ASSIST and an output optical module simulates the optical and mechanical interface of the VLT Nasmyth focus.

During that time GRAAL will complete its standalone tests and validation. Then, mounted on ASSIST with the DSM, the whole assembly will be used to fully qualify the adaptive optics loop. The source module of ASSIST with phase screens to generate calibrated turbulence will feed the DSM and GRAAL. The GRAAL real-time computer and wavefront sensor will create realistic conditions for closed-loop operation. The natural guide star mode on-axis of GRAAL will first be tested.

These tests will constitute a strong basis to continue with GRAAL GLAO correction mode tests and characterisation. Then GRAAL will be replaced by GALACSI and the GLAO correction mode of GALACSI tested. The second mode of correction of GALACSI (LTAOs for the MUSE narrow-field mode) will then follow. Before shipment the DSM will be refurbished with the spare thin shell whose delivery is planned for the end of 2013. The second shell in the DSM will then be fully qualified and validated on ASSIST.

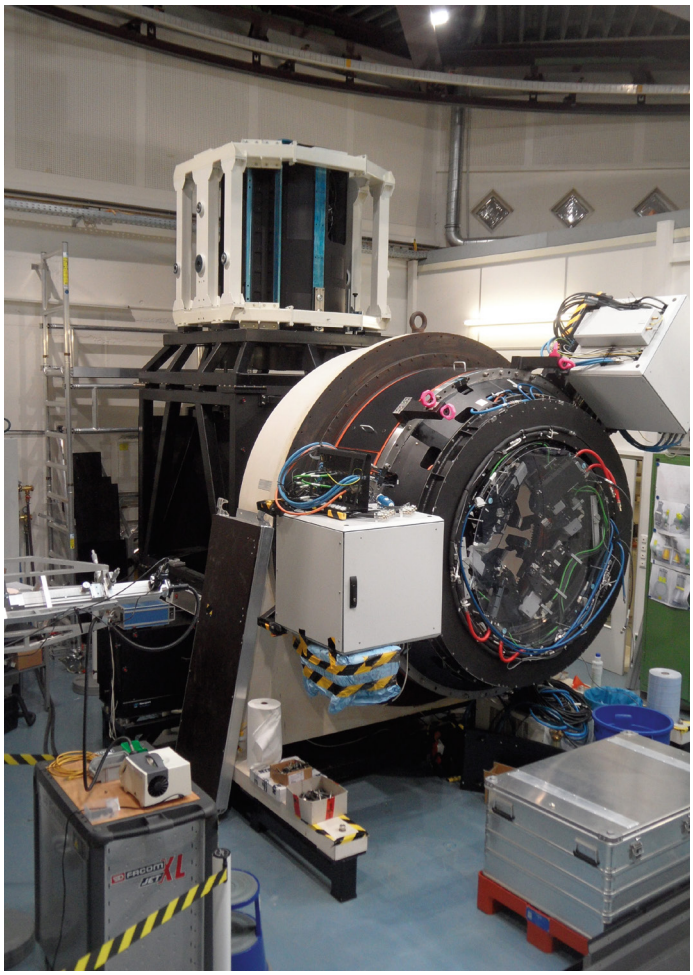

Figure 7. The DSM mounted on the ASSIST test bench in the ESO Garching integration laboratory at the start of the test phase. GRAAL is in the foreground.

The initial commissioning activities of the AOF are expected to last through 2015.

Acknowledgements

Many thanks are due to numerous people who have been involved, occasionally, but over a period of many years, and provided unfailing support to the project: F. Koch for structure analysis and counselling; M. Cayrel for supporting critical steps of development of the thin shell; S. Stanghellini for his expert advice and enthusiasm during the reviews and latest acceptance procedures; J. Schimpelsberger for his diligence with all contract amendments and negotiations; M. Duchateau and R. Brast for their help with electronics design/acceptance reviews. C. Dupuy and S. Tordo have always been active in the background to help with integration and interfaces and R. Stuik from the University of Leiden has been leading the development of ASSIST and helping with the interfacing of the DSM on the test bench. Finally, our Paranal colleagues P. Sansgasset and G. Hüdepohl, who have been our “base of knowledge” concerning VLT M2 units, are thanked together with J.-F. Pirard for preparing the arrival of the AOF in Paranal and the DSM in particular.

References

Arsenault, R. et al. 2010, The Messenger, 142, 12
Arsenault, R. et al. 2010, Proc. SPIE, 7736, 20
Arsenault, R. et al. 2012, Proc. SPIE, 8447, 0J
Biasi, R. et al. 2012, Proc. SPIE, 8447, 88
Hugot, E. et al. 2011, A&A, 527, A4
Kuntschner, H. et al. 2012, Proc. SPIE, 8448, 07
Paufique, J. et al. 2012, Proc. SPIE, 8447, 116
Stroeble, S. et al. 2012, Proc. SPIE, 8447, 115
Stuik, R. et al. 2012, Proc. SPIE, 8447, 118

ALMA Completes Its First Science Observing Season

Martin Zwaan[1]
Paola Andreani[1]
Andrew Biggs[1]
Maria Diaz Trigo[1]
Evanthia Hatziminaoglou[1]
Elizabeth Humphreys[1]
Dirk Petry[1]
Suzanna Randall[1]
Thomas Stanke[1]
Felix Stoehr[1]
Leonardo Testi[2]
Eelco van Kampen[1]

[1] European ALMA Regional Centre, ESO
[2] ESO

The Atacama Large Millimeter/submillimeter Array (ALMA) has recently completed its first year of science observing and the second year is beginning with increased capabilities. The completion rates for European-led proposals are reported. User support activities in the European ALMA Regional Centres are summarised, together with the results of a survey of users.

Wednesday, 2 January 2013, marked the completion of data-taking for Cycle 0, ALMA's first ever science observing season. In Cycle 0, data were observed and processed on a "best effort" basis since, during this observing season, many future capabilities still had to be commissioned, new antennas integrated into the array and software and procedures still needed to be tested. Despite these constraints, it is very gratifying that of the 113 highest priority projects selected for the first Cycle, 94 % were fully or partially observed, 35 of which were led by European principal investigators (PIs). At the time of writing, 26 of these European-led projects have been fully observed and their quality assured, and the data have been delivered to the PIs. Of the other nine projects that were not fully observed, the existing data have been partly delivered. In summary, 35 European PIs have received Cycle 0 data thus far.

Cycle 0 science

The first proprietary ALMA data were delivered to users in all three executives in December 2011. It is expected that the final quality-assured Cycle 0 data will have arrived with the PIs by the end of February 2013. Many teams that received ALMA Cycle 0 data are still in the midst of the analysis and paper writing, but a number of papers based on Cycle 0 have been published already, in addition to the many based on Science Verification data. The exciting results span the whole gamut of astronomical research, ranging from submillimetre galaxies and gamma-ray bursts to shells around asymptotic giant branch stars and brown dwarfs. More details of Cycle 0 science results are presented in the summary of the conference "The First Year of ALMA Science" on p. 50.

Operations and user support

High quality end-to-end user support has always been one of the main pillars of the ALMA operations model. Even for Early Science, where it has been emphasised that the execution of observing programmes would be done on a best-effort basis, ALMA has attempted to provide optimal user support throughout the lifetime of the projects. Contact scientists appointed to all Cycle 0 projects worked together with the PIs and expert staff at the Joint ALMA Observatory (JAO) in Chile and the ALMA Regional Centres (ARCs), making sure that all Phase II material was technically feasible and in agreement with the science goals. After execution of the projects, the data went through a series of quality assurance steps, the last one being full calibration of the data and the creation of datacubes or images. Gaining experience throughout the cycle, the time between data-taking and delivery to the PI dropped to approximately one month by the end of Cycle 0.

The European ARC nodes

Throughout Cycle 0 it has become clear that the European support structure with a distributed network of ARC nodes has worked extremely well. These local expertise centres provided support to their communities by organising community days, training sessions and science-oriented meetings, provided help with the preparation of Phase 2 material and hosted users for expert face-to-face support during proposal preparation and data reduction. It is also important to emphasise that nearly all contact scientists for European Cycle 0 projects are located at the ARC nodes. ARC nodes are therefore very well up to speed on the specifics of Cycle 0 projects. Thus far, PIs and CoIs of 20 Cycle 0 projects have visited one of the seven ARC nodes for face-to-face data reduction support, with the purpose of improving the calibration and imaging of their data beyond what was already provided by the observatory.

User experience

In September 2012 the second user satisfaction survey was conducted among the nearly 4000 registered users of ALMA. One of the aims of the survey was to query users about their experience with Cycle 0 scientific operations, data processing and support at the ARCs and ARC nodes. The user profile is dominated by radio and millimetre/submillimetre astronomers using ground-based facilities. However, up to 40 % of the users are experts in wavelengths longer than the submillimetre, in space-based facilities or in theory/modelling, emphasising the diversity of the ALMA community.

More than 75 % of the users who worked with ALMA data considered their quality above average. Remarkably, only 48 % indicated that they used the ALMA data analysis package CASA to reduce their data, emphasising the need to offer more data reduction workshops to the community. The high quality of the European support structure was also acknowledged: from the users who visited an ARC node for Cycle 0 data reduction, 93 % considered the quality of support above average. The experience with the generation of Scheduling Blocks (SBs) was rated above average by 55 % of Cycle 0 users, but it should be noted that the Observing Tool was still under active development during Cycle 0. Support from the ARC contact scientists for generation of Cycle 0 SBs was rated above average by 83 % of the users.

First Light for the KMOS Multi-Object Integral-Field Spectrometer

Ray Sharples[1]
Ralf Bender[2, 5]
Alex Agudo Berbel[2]
Naidu Bezawada[3]
Roberto Castillo[4]
Michele Cirasuolo[3]
George Davidson[3]
Richard Davies[2]
Marc Dubbeldam[1]
Alasdair Fairley[3]
Gert Finger[4]
Natascha Förster Schreiber[2]
Frederic Gonte[4]
Achim Hess[5]
Ives Jung[4]
Ian Lewis[6]
Jean-Louis Lizon[4]
Bernard Muschielok[5]
Luca Pasquini[4]
Jeff Pirard[4]
Dan Popovic[4]
Suzanne Ramsay[4]
Phil Rees[3]
Josef Richter[5]
Miguel Riquelme[4]
Myriam Rodrigues[4]
Ivo Saviane[4]
Joerg Schlichter[5]
Linda Schmidtobreick[4]
Alex Segovia[4]
Alain Smette[4]
Thomas Szeifert[4]
Arno van Kesteren[4]
Michael Wegner[5]
Erich Wiezorrek[2]

[1] Department of Physics, University of Durham, United Kingdom
[2] Max-Planck-Institut für extraterrestrische Physik, Garching, Germany
[3] UK Astronomy Technology Centre, Royal Observatory, Edinburgh, United Kingdom
[4] ESO
[5] Universitätssternwarte München, Germany
[6] Sub-Department of Astrophysics, University of Oxford, United Kingdom

The KMOS near-infrared multi-object integral-field spectrometer was transported to Chile in the middle of 2012 and achieved its first views of the Paranal skies in November 2012. We describe the delivery and re-integration of KMOS and present the first results from the two on-sky commissioning runs.

Figure 1. The KMOS CACOR leaving the UK Astronomy Technology Centre (left), and installed in its open-top container ready for the sea journey to Paranal (right).

KMOS is one of a suite of second generation VLT instruments which, along with MUSE (Bacon et al., 2012) and SPHERE (Kasper et al., 2012), will bring exciting new capabilities to the Paranal Observatory in next few years. KMOS is a unique design of near-infrared multi-object spectrograph that uses deployable integral field units to obtain spatially resolved spectra for up to 24 target objects selected from within an extended 7.2-arcminute diameter field of view (Sharples et al., 2010).

In mid-2012, KMOS reached its Provisional Acceptance Europe milestone (Ramsay, 2012) and then began its long journey to the summit of Cerro Paranal via a combination of road, sea and air transport. Whilst the main cryostat could be shipped in a Boeing 747 cargo hold, the auxiliary CACOR unit, which carries the KMOS electronics cabinets in a large co-rotating structure, was too large to fit into any available air-freight carrier. This large item was therefore securely packed and made the slightly more perilous, but more leisurely, journey on the open deck of a container ship (Figure 1). Fortunately both cargoes arrived without damage, more or less at the same time, at the port in Antofagasta. KMOS then made the final leg of the journey by road to the new integration hall at the Paranal Observatory.

KMOS was fully re-assembled and re-calibrated in the integration hall over an eight-week period in September–November 2012 by a dedicated team of technical experts from the UK and German consortium partners, working closely with ESO personnel. After an extensive set of verification tests, the instrument was then taken up the final stretch of the mountain road at walking pace (Figure 2, left), before being installed on the Nasmyth platform of VLT Unit Telescope 1 (Antu). Because of the size of the CACOR (about four metres high), this item had to be lifted directly

Figure 2. KMOS cryostat on the road from the integration hall to the summit (left); the CACOR being hoisted into the dome of UT1 (right).

Figure 3. Some of the commissioning team in the VLTI control room during the first night of observations with KMOS.

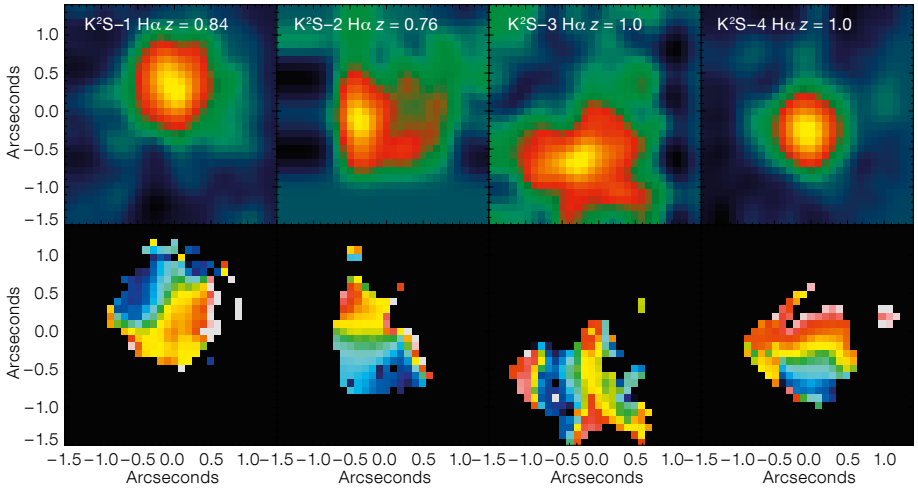

Figure 4. (Top) Hα emission line maps (top) and derived velocity fields (bottom) for a sample of faint $z \sim 1$ emission-line galaxies in the GOOD-South field. The brightest targets have an observed integrated Hα flux of 1.0×10^{-16} ergs cm^{-2} s^{-1}. These data were obtained with only 30 minutes of on-source exposure using KMOS and demonstrate the power of this facility instrument for such surveys. Reductions courtesy of Mark Swinbank.

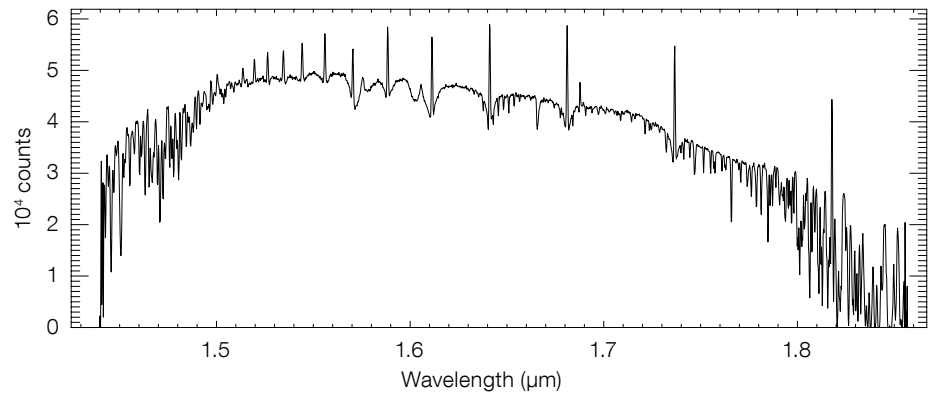

Figure 5. KMOS *H*-band spectrum of the B8 III emission line star Hip 022112 (HD 30123).

in through the dome aperture using an external crane (Figure 2, right).

Commissioning-1

First light with KMOS occurred on 21 November 2012. After a slightly cloudy start, the dome opened at 21:30 and the first targets were acquired. Initially this involved pointing the telescope at a relatively bright star and taking short exposures with one arm at a time placed at the centre of the field. Every single star appeared within the integral field unit (IFU) field of view of 2.8 × 2.8 arcseconds, much to the relief of the commissioning team (Figure 3)! Even this relatively simple observation required a large number of systems to be working together, such as the real-time display, which shows the positions of the target objects in the reconstructed datacubes. This acquisition sequence is a key feature of KMOS and allows the telescope pointing to be refined by placing a subset of the pickoff arms onto bright targets, which are then centred automatically using a shift and rotation of the telescope field of view (in much the same way that bright reference stars are used to align the slit masks in the FORS2 spectrograph). Once the field is aligned, these arms can then be redeployed to science targets.

One of the first issues to address therefore was the astrometric positioning of the arms; this included both the overall plate scale, and any radial variation at the arm focal plane(s), and also the local corrections (lookup tables) which are used to take out the individual variations in the movement of each arm. The latter stage was particularly troublesome, as it required an astrometric calibration procedure to be set up on sky using densely populated star fields in open or globular star clusters. The final calibration was not achieved until Commissioning-2, but now demonstrates that the arms have a final 1σ positioning accuracy of 0.1 arcseconds. The rest of the first commissioning run was taken up with exercising all the KMOS modes, including its unique capabilities to produce large mosaic patterns covering up to 60 by 40 arcseconds on the sky, and in obtaining calibration and performance data to complete the verification tests (e.g., Figure 4).

Commissioning-2

The second commissioning run took place in the latter half of January 2013 and, whilst not blessed with the same level of clear skies as the first run, enabled the commissioning team to complete a number of outstanding tests and improve the integration with the VLT control system. A further focus of the second run was to obtain some deep-sky observations with KMOS to evaluate the different modes of sky subtraction, and to fully test the KMOS data reduction pipeline SPARK (Davies et al., 2012). Calibration arc and flatfield exposures were taken automatically during the daytime at position angles close to those of the night's observations; this step minimises the effects of instrument flexure on the wavelength accuracy. After calibration using the daytime arc exposures, the remaining shifts of the night-sky OH lines have a root mean square residual < 20 km/s; this can be reduced to < 5 km/s by application of a simple model of the flexure. Figure 5 shows a typical example spectrum of a bright emission-line star processed at the telescope using the default pipeline.

Some of the more visually impressive capabilities of KMOS are the spectral images which can be produced using the mosaic mode in which the IFUs are packed into a regular grid pattern, with gaps which are then filled by offset pointings of the telescope. Two modes are available: either using all 24 arms (16 pointings) or a reduced mosaic of eight arms (nine pointings) if a faster coverage of a smaller area is required. All of the offsetting and combining of the cubes is handled automatically by the templates and data pipeline. Figure 6 shows one of the early results obtained (using non-sidereal tracking) of an *H*-band mosaic of Jupiter. Although the full information content of this observation (75 000 spectra in total) cannot be gleaned from a simple two-dimensional picture, the colour scheme has been tuned to reveal the spectral differences (mainly methane bands) in the equatorial zones and the polar caps of the planet. Another example is shown in Figure 7 for observations of 30 Doradus in the Large Magellanic Cloud, where the cube has been sliced to show the continuum in the *K*-band,

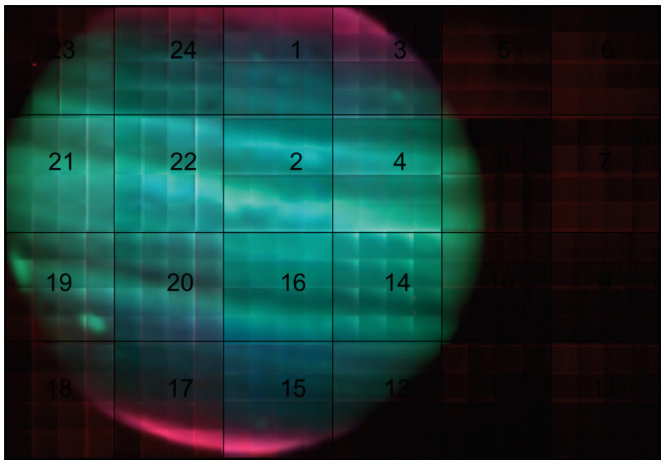

Figure 6. Reconstructed spectral image of Jupiter (pseudo colours refer to narrow bands extracted from the spectrum to highlight various features). This image was created using the 24-arm mapping template with non-sidereal tracking and comprises nearly 75 000 spectra. The numbers refer to zones covered by specific IFUs during the dithered pointings.

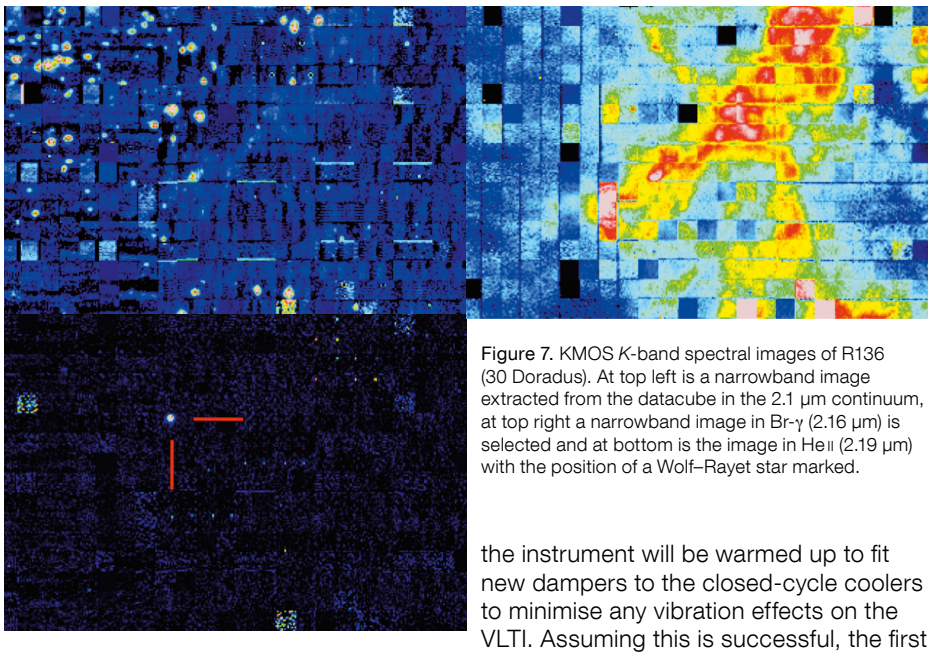

Figure 7. KMOS *K*-band spectral images of R136 (30 Doradus). At top left is a narrowband image extracted from the datacube in the 2.1 μm continuum, at top right a narrowband image in Br-γ (2.16 μm) is selected and at bottom is the image in He II (2.19 μm) with the position of a Wolf–Rayet star marked.

regions of Brackett-γ emission and the He II emission characteristic of massive Wolf–Rayet stars. The data for these commissioning observations are available for download[1].

Current status

The data from the first two commissioning runs are currently being fully reduced and analysed. During both observing campaigns, the instrument has performed nearly flawlessly and it is offered to the ESO community in the Call for Proposals for Period 92 (October 2013–March 2014). A final "Paranalisation" run is scheduled for March 2013, after which the instrument will be warmed up to fit new dampers to the closed-cycle coolers to minimise any vibration effects on the VLTI. Assuming this is successful, the first community Science Verification observations may take place in summer 2013. We look forward to much exciting new science from KMOS in the next few years.

References

Bacon, R. et al. 2012, The Messenger, 147, 4
Davies, R. et al. 2010, Proc. SPIE, 7735, 77356V
Kasper, M. et al. 2012, The Messenger, 149, 17
Ramsay, S. 2012, The Messenger, 149, 16
Sharples, R. et al. 2010, The Messenger, 139, 24

Links

[1] Access to presented KMOS commissioning data: http://www.eso.org/sci/activities/vltcomm/kmos.html

Image of the dusty H II region Sharpless 2-292 composed from MPG/ESO 2.2-metre telescope and Wide Field Imager *BVR* and Hα images. The centrally located, bright, early-type (B0) star HD 53367 ionises the nebula. More details in Release eso1237.

Boötes-I, Segue 1, the Orphan Stream and CEMP-no Stars: Extreme Systems Quantifying Feedback and Chemical Evolution in the Oldest and Smallest Galaxies

Gerard Gilmore[1]
Sergey Koposov[1]
John E. Norris[2]
Lorenzo Monaco[3]
David Yong[2]
Rosemary Wyse[4]
Vasily Belokurov[1]
Doug Geisler[5]
N. Wyn Evans[1]
Michael Fellhauer[5]
Wolfgang Gieren[5]
Mike Irwin[1]
Matthew Walker[1, 6]
Mark Wilkinson[7]
Daniel Zucker[8]

[1] Institute of Astronomy, Cambridge, United Kingdom
[2] Mount Stromlo Observatory, Australian National University, Canberra, Australia
[3] ESO
[4] Johns Hopkins University, Baltimore, USA
[5] Departamento de Astronomia, Universidad de Concepcion, Chile
[6] Harvard University, Cambridge, USA
[7] University of Leicester, Leicester, United Kingdom
[8] Macquarie University, Sydney, Australia

Galactic satellite galaxies provide a unique opportunity to map the history of early star formation and chemical evolution, the baryonic feedback on gas and dark matter, and the structure of low-mass dark matter halos, in surviving examples of the first galaxies. We are using VLT–FLAMES spectroscopy to map the kinematics and chemical abundances of stars in several ultra-faint dwarf spheroidal galaxies and the enigmatic Orphan Stream in the Halo. Two paths of early chemical enrichment at very low iron abundance are observed directly: one rapid and carbon-rich (CEMP-no), one slow and carbon-normal. We deduce long-lived, low-rate star formation in Boötes-I, implying insignificant dynamical feedback on the structure of its dark matter halo, and find remarkably similar kinematics in the apparently discrete systems Segue 1 and the Orphan Stream.

With the discoveries from the Sloan Digital Sky Survey, the galaxy luminosity function has been extended down to luminosities three orders of magnitude below previous limits in recent years. Remarkably, these extremely low luminosity objects, the dwarf spheroidal (dSph) galaxies with total luminosities as low as 1000 $L_{\odot}$, comparable to a moderate star cluster, are quite unlike star clusters — they are real galaxies. Fortunately, with their very few red giants but more populous main-sequence turn-off stars, they are within range of detailed study, with considerable efforts currently underway at the Very Large Telescope (VLT) and Keck.

These lowest-luminosity galaxies provide a unique opportunity to quantify the formation and chemical enrichment of the first bound structures in the Universe. At present, there are no convincing models for the origin and evolution of these extreme objects — observations lead the way. The ultra-faint dSphs certainly have extreme properties. They are clustered in groups on the sky, their velocity dispersions are tiny — no more than 3–4 km/s at the lowest luminosities — yet the objects themselves are very extended, with half-light radii of hundreds of parsecs, implying extreme dark matter dominance. Their chemical abundances are also extreme, with dispersions of several dex, and containing stars down to [Fe/H] = –4. There are hints that they are associated with, or possibly entangled in, kinematic streams and superimposed on — or in — the tidal tails of the more luminous Sagittarius dSph (Sgr) galaxy.

The lowest luminosity dSphs do not look like the tidal debris of larger systems, they look like the most primordial galaxies of all. Arguably even more interesting than their relevance as galaxy building blocks is to understand the objects themselves. Are they the first objects? Did they contribute significantly to reionisation? What do they tell us of the first stars? What was the stellar initial mass function (IMF) at near-zero metallicity? How are the faintest dSphs related to more luminous dSphs and the Milky Way galaxy?

In order to address these questions, we are obtaining VLT FLAMES observations using both the spectrographs GIRAFFE and UVES, with exposures of up to more than 15 hours, of member stars of the most enigmatic of the ultra-faint systems. These targets include: the lowest luminosity system Segue 1 (Belokurov, 2007a; see Simon et al. [2011] for a detailed Keck study) and the Orphan stream (Belokurov et al., 2007b), both of which are at similar distances to the bifurcated tidal tail of Sgr (Ibata, Gilmore & Irwin, 1994); the common-distance and similar-velocity pair Leo-IV and Leo-V (Belokurov et al., 2008); and the inner regions of Boötes-I (Belokurov et al., 2006b), a surviving example of one of the first bound objects to form in the Universe, providing a touchstone to test the chemical evolution of the earliest low-mass stars.

Our FLAMES GIRAFFE and UVES spectra are beginning to quantify the kinematics and abundance distribution functions in these systems, including several element ratios, providing the first quantitative study of what we find to be survivors of truly primordial systems that apparently formed and evolved before the time of reionisation. Our target fields are summarised in Figure 1.

Segue 1 and the Orphan Stream

Segue 1 is the lowest luminosity galaxy known. It has a wide abundance range, including hosting a very carbon-enhanced metal-poor star with no enhancement of heavy neutron-capture elements over Solar ratios (called a CEMP-no star: c.f., Norris et al. [2010a] for our VLT study and Beers & Christlieb [2005] for the definitions of metal-poor star subclasses). Such stars, which are like those in the Milky Way Halo field, are suspected to be successors of the very first supernovae — see below. The velocity distribution measured in Segue 1, which is consistent with the Keck study of Simon et al. (2011), shows a very narrow distribution, consistent with a dispersion of less than 4 km/s. In spite of this low dispersion, Segue 1 is completely dark-matter dominated, with a mass-to-light ratio in excess of 1000. The velocity distribution function, in which Segue 1 has its radial velocity near V = 200 km/s, also indicates the presence of stars from the Sagittarius tidal stream (at V = 0 km/s), which is at a very similar distance, and stars in a cold kinematic structure with radial velocity V = 300 km/s. This cold highest-velocity

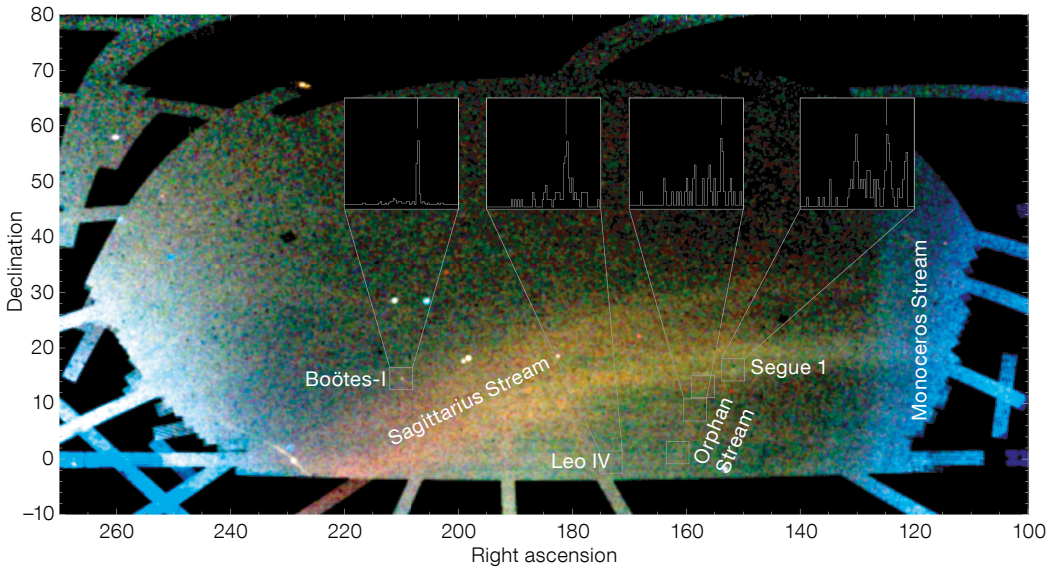

Figure 1. The background shows the "Field of Streams" (Belokurov et al., 2006a), the distribution of turn-off stars observed by the Sloan Digital Sky Survey, statistically colour-coded by distance with the bluer colour showing more nearby, the redder more distant streams. The fields observed for this project by the VLT are marked in grey, with representative velocity distributions indicated. The velocity distribution for Boötes-I is marked by its extreme narrowness. The low surface brightness Orphan Stream is very evident in velocity space, again with very low velocity dispersion. Segue 1 shows three distinct velocity peaks, corresponding to the Sgr Stream, Segue 1 itself, and the "300 km/s" stream, evident only in velocity space.

stream is not yet well defined, and remains under study.

The Orphan Stream provides another example of a Halo stream, although in this case it has a sufficiently high surface brightness to allow it to be traced over more than 60 degrees of arc. The peri-galacticon of the Orphan Stream orbit passes close to Segue 1, and hence to the Sagittarius tidal tail. As Figure 1 illustrates, the internal velocity dispersion in the Orphan Stream is unresolved at the resolution of the observations, being less that 3–4 km/s. The Orphan Stream and Segue 1 kinematics and distance, the latter determined from main-sequence turn-off fitting, provide an interesting illustration of the complexity of the outer Galactic Halo. Both Segue 1 and the Orphan Stream have similarly low internal velocity dispersions. Remarkably, at the Orphan Stream's closest approach to Segue 1, both have the same Galactocentric distance (within uncertainties), which is also the same as the local Sagittarius tail, being separated by only a few kiloparsecs (kpc) at most. Even more bizarrely, at the point of closest approach, the orbit of the Orphan Stream has exactly the same Galactocentric radial velocity as does Segue 1. Is this coincidence, or evidence of a common history?

The analysis of Simon et al. (2011) suggests that Segue 1 is contained inside its tidal radius, and is a robust, albeit small and faint, galaxy, which just happens to be passing through a busy part of the outer Galaxy. The metal-poor ([Fe/H] = –3.5) CEMP-no star Segue 1-7, which we have studied with the VLT, lies almost four half-light radii from the centre of Segue 1, while all the other well-studied members are inside 2.3 half-light radii (70 pc). Does this hint at tidal truncation of an earlier, much larger (and more luminous?) predecessor? Segue 1 is very deep inside the Galactic tidal field, well inside the (disrupting) Sgr dSph, and the Large Magellanic Cloud–Small Magellanic Cloud pair, with their gaseous tidal stream. All the dSph galaxies that are not deep in the Galactic tidal field have much larger half-light radii (Gilmore et al., 2007). We also have the remarkable similarity (indeed, near identity) of the distances and radial velocities of Segue 1 and the Orphan Stream as further clues. In spite of searching, we have not (as yet) found any trace of any extra-tidal Segue 1/Orphan Stream member stars, or a physical link between the systems: there are no identified stars with appropriate velocities in the spatial region between the Orphan Stream peri-galacticon and Segue 1. Are they just ships passing in the dark night? The hunt for enlightenment continues.

Boötes-I

Boötes-I provides an example of a complementary case: an apparently normal, extended dSph galaxy (half-light radius 240 pc), at 60 kpc Galactocentric distance, whose special features are its low surface brightness and low total luminosity (M_V = –6). Boötes-I has low mean metallicity (with a range from [Fe/H] = –3.7 to –1.9) and hosts a CEMP-no star that we have studied with the VLT ([Fe/H] = –3.3; Norris et al., 2010b). Our GIRAFFE spectra have been analysed for a kinematic study (see Koposov et al., 2011). Using careful data reduction techniques, Koposov et al. (2011) showed that GIRAFFE spectra obtained in single one-hour observing blocks over several years can be combined to deliver radial velocities with an accuracy floor approaching 0.1 km/s. From this study we demonstrated that Boötes-I has a smaller velocity dispersion than suggested by previous studies. We showed the kinematics to be best described by a two-component system, a majority with dispersion 2.5 km/s, and a minority with dispersion as high as 9 km/s, or by a single dispersion of 4.6 km/s. Our preferred interpretation is that the apparent multi-component kinematic structure may reflect orbital anisotropy inside Boötes-I. Our observations to date are limited to the central regions, so further study at larger radii is required to clarify the situation.

There are key issues in early galaxy evolution which can be resolved by the analysis of chemical element distributions. These include the early stellar high-mass IMF, star formation rates at very

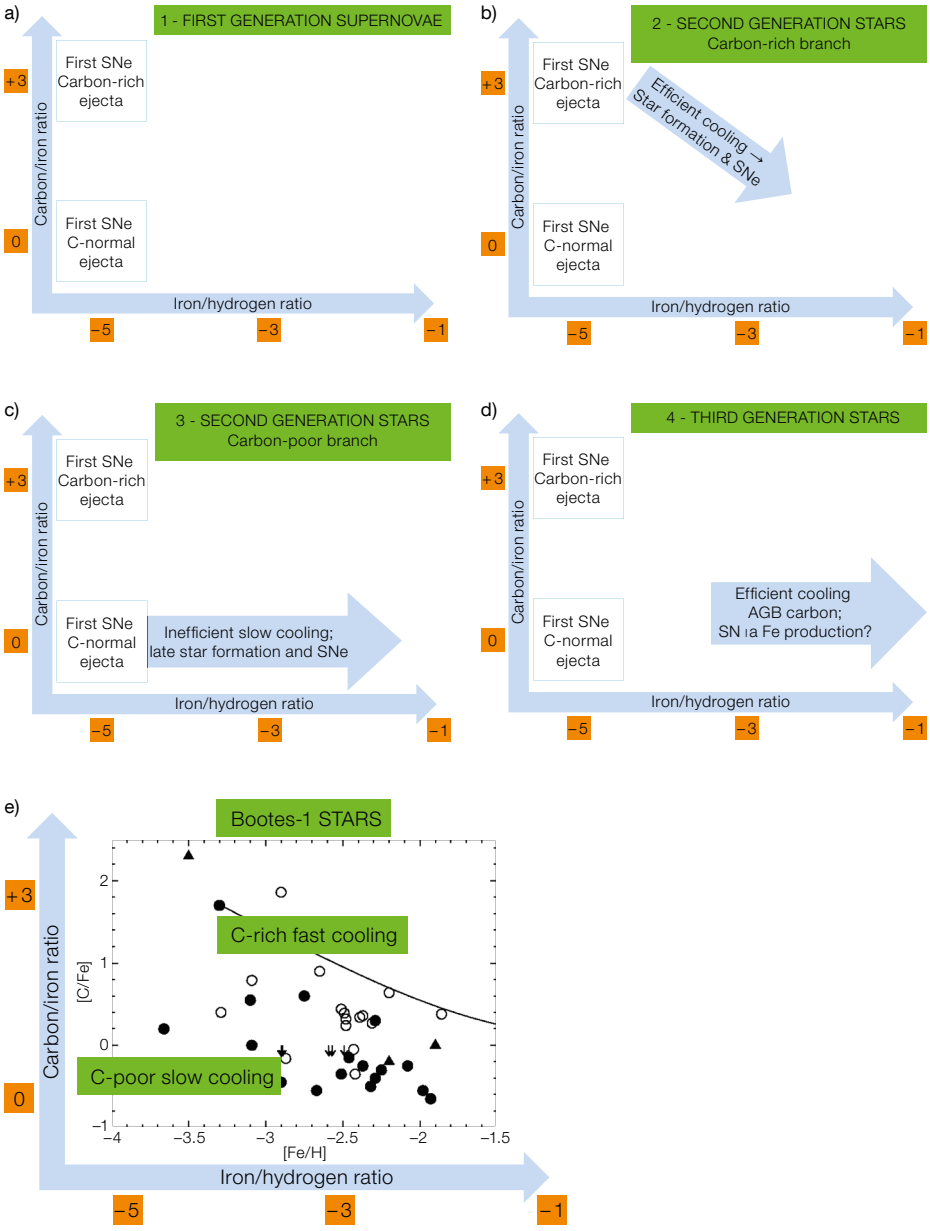

Figure 2. A schematic diagram of the two star formation and evolutionary paths evident at the lowest abundances. The very first stars, apparently of high mass, generate two patterns of chemical enrichment — carbon-enhanced and carbon-normal (Figure 2a). This difference may correspond to different progenitors, or may simply be spatial inhomogeneity from a single SN. The carbon-enhanced material very rapidly cools, apparently forming stars with a wide range of masses, including SN progenitors, which generate standard Galactic Population II abundances (Figure 2b). This process continues until the carbon abundance in the ISM is diluted to the Solar value, when [Fe/H] ~ −3. The lower carbon abundance ISM does not take part in this enrichment process, but on a slower timescale stars are formed, again with a wide range of masses and an apparently standard IMF (Figure 2c). This enrichment path also eventually reaches [Fe/H] = −3. The whole ISM is now sufficiently enriched for efficient cooling, so that chemical evidence of the evolutionary path is now lost (Figure 2d). Should either path correspond to sufficiently slow star formation, SNe Type Ia will generate low [α/Fe] at this stage. The correspondence of this model with data from stars in Boötes-I (circles) and Segue 1 (triangles) is shown in Figure 2e.

early times, and their consequences, and feedback on baryonic gas and the dark matter potential well. Our UVES observations of Boötes-I address these points directly (Gilmore et al., 2013).

α-elements and the IMF

The α-elements, together with a small amount of iron, are created and ejected by core-collapse supernovae, on timescales of less than 10^8 years after the formation of the supernova progenitors.

Enhanced ratios of α-element/Fe above the Solar values are expected in stars formed from gas that is predominantly enriched by these endpoints of massive stars. Thus chemical abundances in the stars formed within the first 0.5 Gyr after star formation began will reflect the products of predominantly core-collapse supernovae.

Although we see hints of a declining α-element abundance, suggestive of a resolution of the duration of the chemical evolution of Boötes-I, this is not formally significant in our present sample. The observed lack of scatter in these element ratios at a given [Fe/H] requires that: (i) the stars formed from gas that was enriched by ejecta sampling the mass range of the progenitors of core-collapse supernovae (SNe); (ii) the supernova progenitor stars formed with an IMF similar to that of the Solar neighbourhood today; and (iii) the ejecta from all SNe were efficiently well-mixed. Both the first and last points set an upper limit on how rapidly star formation could have proceeded, since: the star formation regions need to populate the entire massive-star IMF, the stars need sufficient time to all explode, and the gas needs time to mix the ejected enriched material. All these steps must occur before substantial numbers of low-mass stars form.

The observed lack of scatter in the α-element abundance ratios requires that the well-sampled IMF of core-collapse supernova progenitors is invariant over the range of time concerned and/or the iron abundance. This can be expressed as a constraint, from the scatter, on the variation in slope of the massive star IMF, assuming that the ratios reflect IMF-averaged yields. A scatter of 0.02 dex constrains the variation in IMF slope to be 0.2. The overall agreement between the values of the elemental abundances in Boötes-I stars and in the field of the Halo implies the same value of the massive

star IMF that enriched the stars in each of the two samples, although our formal limit on this IMF slope is only agreement within a slope range of 1.

The Galactic Halo and Boötes-I (and Segue 1) display a large range in carbon abundance at low metallicity. For iron abundances greater than about [Fe/H] = –3.2, excess carbon enhancements above the solar [C/Fe] ratio are consistent with carbon production in asymptotic giant branch (AGB) companions (called CEMP-r/s stars, which have apparent contributions of both rapid (r) and slow (s) nucleosynthetic processes; Beers & Christlieb, 2005). At lower values of [Fe/H], excess carbon is commonly seen, but is inconsistent with AGB production: rather the CEMP-no stars are more likely to have formed from gas enriched by non-standard supernovae (such as "mixing and fallback" supernovae), or by the winds from rapidly rotating massive stars. In both cases the supernova progenitors were massive stars formed from primordial material — the first stars.

CEMP-no stars

Our discovery of CEMP-no stars in the two dwarf galaxies Segue 1 and Boötes-I is strong evidence for their self-enrichment from primordial material. The carbon over-abundance reflects the yields of the very first generation of supernovae or massive stars. This provides an opportunity to consider the evolutionary history of the extremely carbon-enriched, iron-poor interstellar medium gas in these galaxies.

A key piece of information is that the most iron-poor star currently known in Boötes-I is not carbon-enhanced. Carbon-enhanced and carbon-normal stars co-exist at the same low iron abundance within the same system (and in the Galactic field Halo; c.f. Caffau et al., 2011). This provides direct evidence that carbon enhancement is not required for very low-iron abundance gas to cool and form low-mass stars. The additional information we consider here is that CEMP-no stars are not found at [Fe/H] greater than –2.5, either in the field Halo or in dwarf spheroidal galaxies.

Given the amplitude of the [C/Fe] and [Mg/Fe] values in CEMP-no stars, one must also explain why stars are not found with intermediate C and Mg excesses at higher [Fe/H]. Apparently the highly C- and Mg-enriched ISM does not survive to mix with "normal" enriched ISM and form more stars with moderate CEMP-no enrichment. Rather, the cooling efficiency of the highly carbon-enriched material must be sufficiently great that all of it cools and forms (the surviving) low-mass stars mixing with "normal" SNe ejecta before [Fe/H] reaches –3 dex. That is, our Boötes-I data provide direct evidence for two discrete channels of chemical enrichment at very low iron abundances.

With our current knowledge of stars in Boötes-I, there is no direct chemical evolution track (assuming standard yields of carbon and iron) between the CEMP-no stars and the carbon-normal stars with [Fe/H] < –3. This means that at very low iron abundance there is no one-to-one relationship between [Fe/H] and the time since the first SNe. This conclusion is summarised in Figure 2, which shows the chemical evolutionary enrichment sequence deduced from our UVES study, and its consistency with observations. The CEMP-no stars form rapidly out of gas enriched by only one generation of SNe and most likely prior to the onset of effective mixing. This results in a small mixing length, spatial inhomogeneity and a large scatter in elemental abundance ratios.

Such a scenario requires that the gas within which the CEMP-no stars form can cool and be locked up in low-mass stars very rapidly, and with high efficiency, so that material with this abundance pattern is removed from the system at early times. This picture is consistent with models of the formation of very metal-poor low-mass stars which appeal to enhanced cooling due to carbon. It may well be that the CEMP-no material resulted from a very small number of (Population III?) supernovae, possibly only one.

A surviving primordial galaxy

Our metallicity and elemental abundance data show that Boötes-I has evolved as a self-enriching star-forming system, from essentially primordial initial abundances. This allows us uniquely to investigate the place of CEMP-no stars in a chemically evolving system, as well as to limit the timescale of star formation in this dSph. The low elemental abundance scatter requires low star formation rates, allowing time for SNe ejecta to be created and mixed over the large spatial scales relevant. This is further evidence that Boötes-I survived as a self-enriching star-forming system from very early times. It also implies that only unimportant amounts of dynamical feedback between the star formation in Boötes-I and its dark matter halo can have occurred. Boötes-I is indeed a surviving primordial system, ideal to investigate the earliest stages of star formation, chemical enrichment and dark matter properties.

Acknowledgements

Based on data obtained under ESO programmes: P182.B-0372; P383.B-0038; P383.B-0093; P185.B-0946. Data-taking completed in P89. D. G. & W. G. gratefully acknowledge support from the Chilean BASAL Centro de Excelencia en Astrophysica y Technologias Afines (CATA) grant PFB-06/2007. J. E. N. and D. Y. acknowledge support by Australian Research Council grants DP0663562 and DP0984924. R. F. G. W. acknowledges partial support from the US National Science Foundation through grants AST-0908326 and CDI-1124403, and thanks the Aspen Center for Physics (supported by NSF grant PHY-1066293) for hospitality while this work was completed.

References

Beers, T. C. & Christlieb, N. 2005, ARAA, 43, 531
Belokurov, V. et al. 2006a, ApJ, 642, L137
Belokurov, V. et al. 2006b, ApJ, 647, L111
Belokurov, V. et al. 2007a, ApJ, 654, 897
Belokurov, V. et al. 2007b, ApJ, 658, 337
Belokurov, V. et al. 2008, ApJ, 686, L83
Caffau, E. et al. 2011, Nature, 477, 67
Gilmore, G. et al. 2007, ApJ, 663, 948
Gilmore, G. et al. 2013, ApJ, 793, 61
Ibata, R., Gilmore, G. & Irwin, M. 1994, Nature, 370, 194
Koposov, S. et al. 2011, ApJ, 736, 146
Norris, J. E. et al. 2010a, ApJ, 722, L104
Norris, J. E. et al. 2010b, ApJ, 711, 350
Norris, J. E. et al. 2013, ApJ, 762, 28
Simon, J. et al. 2011, ApJ, 733, 46

SUDARE at the VST

Maria Teresa Botticella[1]
Enrico Cappellaro[2]
Giuliano Pignata[3]
Andrea Baruffolo[2]
Stefano Benetti[2]
Filomena Bufano[3]
Massimo Capaccioli[4]
Enrico Cascone[1]
Giovanni Covone[4]
Massimo Della Valle[1]
Aniello Grado[1]
Laura Greggio[2]
Luca Limatola[1]
Maurizio Paolillo[4]
Andrea Pastorello[2]
Lina Tomasella[2]
Massimo Turatto[2]
Mattia Vaccari[5]

[1] INAF–Osservatorio Astronomico di Capodimonte, Italy
[2] INAF–Osservatorio Astronomico di Padova, Italy
[3] Departemento de Ciencias Fisicas, Universidad Andres Bello, Chile
[4] Dipartimento di Fisica, Universita Federico II, Italy
[5] Physics Department, University of the Western Cape, South Africa

The SUpernova Diversity And Rate Evolution (SUDARE) programme on the VLT Survey Telescope aims to collect an unbiased and homogeneous sample of supernovae (SNe) in all types of galaxies out to redshift ~ 0.6. In four years, around 500 Type Ia and core-collapse SNe are expected to be discovered, including significant numbers of rare SN types. The programme is outlined and 100 SNe candidates have already been detected in the first year of the programme. Follow-up spectroscopy of the SN candidates, an important aspect of the programme, is also described.

Despite the key role played by supernovae in discovering the accelerating expansion of the Universe (Perlmutter et al., 1998; Riess et al., 1998) there are still basic questions to answer about SN progenitors and explosion mechanisms. Furthermore the discovery of a growing number of exceptionally bright and extremely faint SNe, as well as peculiar events, suggest the existence of an unexpected SN diversity (Benetti et al., 2005), which is difficult to explain within the standard scenarios. With the goal of achieving a better insight into the physics of SN progenitors of all different flavours, we have started the SUDARE programme which is currently running at the VLT Survey Telescope (VST).

Background: SNe as fascinating transients

SNe are energetic explosions related to some of the most important problems of modern astrophysics. They are one of the more promising tools to probe the nature of dark energy in the Universe and provide a natural laboratory for studying the physics of hydrodynamic and nuclear processes under extreme conditions. SNe are involved in the formation of neutron stars, black holes, and gamma-ray bursts and are sources of neutrino emission, high-energy cosmic rays and gravitational waves. The energy release from SNe can trigger episodes of star formation (SF), impacting the evolution of gas flows and contributing to the feedback processes in galaxies. They are also the main producers of heavy elements and are fundamental for modelling the chemical evolution of galaxies and abundance patterns in clusters of galaxies. Moreover, the metal-rich ejecta of SNe are believed to be potentially important sites of cosmic dust formation.

We recognise two physically different classes of SNe: core-collapse induced explosions of short-lived massive stars (CC SNe) and thermonuclear explosions of long-lived low-mass stars (SNe Ia). All stars more massive than about eight solar masses develop an iron core that cannot be supported by any further nuclear fusion reaction, or by electron degenerate pressure, and hence collapse to form a neutron star or a black hole. Different sub-types of CC SNe have been identified on the basis of their spectroscopic and photometric properties (IIP, IIL, IIn, IIb, Ib, Ic; see Turatto et al., 2003). These subtypes have been associated with a possible sequence of progenitor characteristics related to mass-loss history, with the most massive stars and stars in binary systems losing the largest fraction of their initial mass.

Concerning SNe Ia, there is general consensus that they correspond to thermonuclear explosions of a carbon and oxygen white dwarf (WD) which reaches the Chandrasekhar mass due to accretion from a close companion. Two kinds of evolutionary paths for the progenitors are mostly considered in the literature: a) the single degenerate scenario, in which a WD, accreting from a non-degenerate companion (a main sequence star, a red giant or a helium star), grows in mass until it reaches the Chandrasekhar limit; b) the double degenerate scenario, in which a close double WD system merges after orbital shrinkage due to the emission of gravitational waves. If the total mass of the system reaches the Chandrasekhar limit, carbon ignition under degenerate conditions may produce a Type Ia SN explosion.

Motivations: SN progenitors and the nature of SN diversity

The current picture of the death of massive stars is far from clear and several important questions, such as what is the mass range of the progenitor stars of different CC SN sub-types and what are the effects of rotation, metallicity and binary evolution on these mass ranges, still await answers. The simple scheme where only mass loss drives the evolution of massive stars has difficulties in explaining the wide range of properties shown by CC SNe of the same type and the relative frequencies of the different types (IIP 69%, IIb 12%, IIn 9% and IIL 10% of all Type II; Ib 22%, Ic 54% and 24% peculiar events of all Type Ibc; Li et al., 2011).

The direct detection of the SN progenitor on pre-explosion images provides a robust mapping between the progenitor stars and their explosion, but requires high resolution and deep pre-explosion images, so that reliable results are available only for a dozen nearby SNe (Smartt et al., 2009). The nature of the SN Ia progenitor system and the details of the explosion mechanisms are thus still debated.

The use of SNe Ia as standard candles is based on the assumption that all SNe Ia are highly homogeneous (at different cosmic epochs). However, in the last few years spectroscopic and photometric peculiarities have been noted with increasing frequency (about 50%) and new subclasses of SNe Ia have been introduced (20% with high expansion velocities, 10% as SN 1991bg-like objects, 15% as SN 1991T-like objects, 5% as 2002cx-like objects; see Li et al., 2011). Whether these subclasses form distinct physical groups from normal SNe Ia, with different progenitors and explosion mechanisms, or whether they lie at the extreme end of a continuous distribution, is still unclear.

In this framework, the relationship between SN properties and the parent stellar populations can help constrain the progenitors and hence deepen understanding of the origin of the diversity. In particular, the simultaneous analysis of the cosmic evolution of SN rates and the dependence of SN rates on some host galaxy properties is a powerful diagnostic tool to investigate the effects of age, environment and metallicity on the SN progenitors and their diversity. For example, it appears that subluminous SNe Ia preferably occur in massive non-star-forming host galaxies, while super-luminous SNe Ia occur in relatively metal-poor host galaxies.

Taking into account the short lifetime of massive stars, the CC SN progenitor scenarios can be probed by comparing the star formation rate (SFR) and the rate of CC SNe in the same galaxy sample, assuming the distribution of the masses with which stars were born, i.e. the initial mass function (Botticella et al., 2012). On the other hand, the SN Ia rate echoes the whole star formation history of the host galaxy due to the time delays between the birth of an SN Ia progenitor and its death. By comparing the observed SN Ia rate in different galaxy types with that expected for the star formation history of the parent galaxy population, it is possible to constrain the distribution of the delay times (Greggio, 2010). In turn, this allows us to test the progenitor scenarios, which predict different fractions of binaries exploding with different delays.

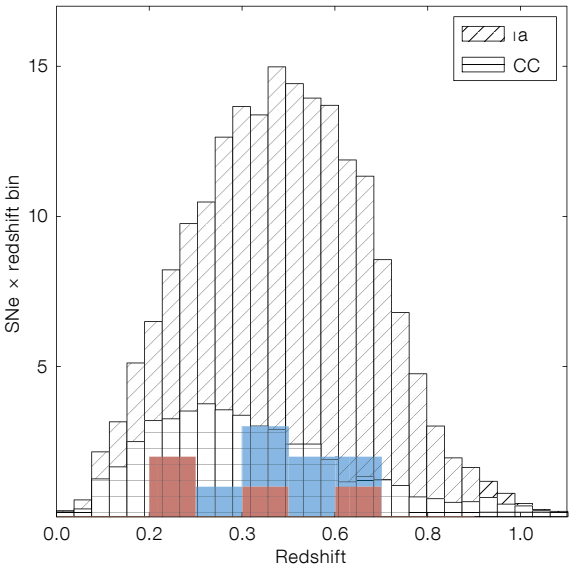

Figure 1. The number of expected SNe discovered by SUDARE in CDFS (200 SNe of which 25% CC SNe) as a function of redshift. The blue (red) histogram shows the Type Ia SNe (CC SNe) with spectroscopic classification discovered in the first season.

Similar considerations hold for the cosmic SN Ia rate in relation to the cosmic SFR.

A new SN search

Our efforts to investigate the cosmic evolution of SN rates began a decade ago with a SN search exploiting the Wide Field Imager (WFI) at the 2.2-metre MPG/ESO telescope. The Southern inTermediate Redshift ESO Supernova Search (STRESS) discovered 86 SNe (nine SNe Ia and 16 CC SNe with spectroscopic classification) during 16 observing runs distributed over a period of six years (from 1999 to 2005; Cappellaro et al., 2005). We found that the CC SN rate is already higher by a factor of two with respect to the local value by redshift $z = 0.2$, whereas the SN Ia rate remains almost constant. This finding implies that a significant fraction of SN Ia progenitors have a lifetime longer than 2–3 Gyr (Botticella et al., 2008). However, the SN sample collected from STRESS was not large enough to perform a statistically significant investigation of the SN diversity.

Therefore we decided to contribute to the international consortium for the delivery of OmegaCAM and the VST telescope (Capaccioli & Schipani, 2011; Kuijken, 2011). The wide field of view and high spatial resolution of OmegaCAM , jointly with the excellent quality of the VST optics, offers an unprecedented opportunity for an SN search in the redshift range $0.3 < z < 0.6$. This redshift range is crucial to connect measurements from past SN surveys in the nearby Universe and the future high-redshift surveys like the Dark Energy Survey (DES) or, in the longer term, with facilities such as the Large Synoptic Survey Telescope (LSST) and the ESA Euclid satellite mission.

Detailed simulations assuming the VST performance and the observational strategy of SUDARE show that we should discover about 500 SNe, of which 25% are expected to be CC SNe (Figure 1) by the end of a four-year programme. The size of this SN sample is suitable both for the measurement of the rate of all SN sub-types and to discover rare types of SN explosions. Indeed the depth of SUDARE images allows us to exploit, during each epoch, a volume of space that is about 1000 times larger than that sampled by nearby SN surveys and thus is more suitable to discover rare and peculiar events. Given an observed rate of peculiar SNe of the order of 5% of "standard" CC and SN Ia rates, we expect, by the end of our programme, to have detected about two dozen of such "weird" stellar explosions.

The novelty of SUDARE is the emphasis that we put on the analysis of the parent stellar population, with the aim of

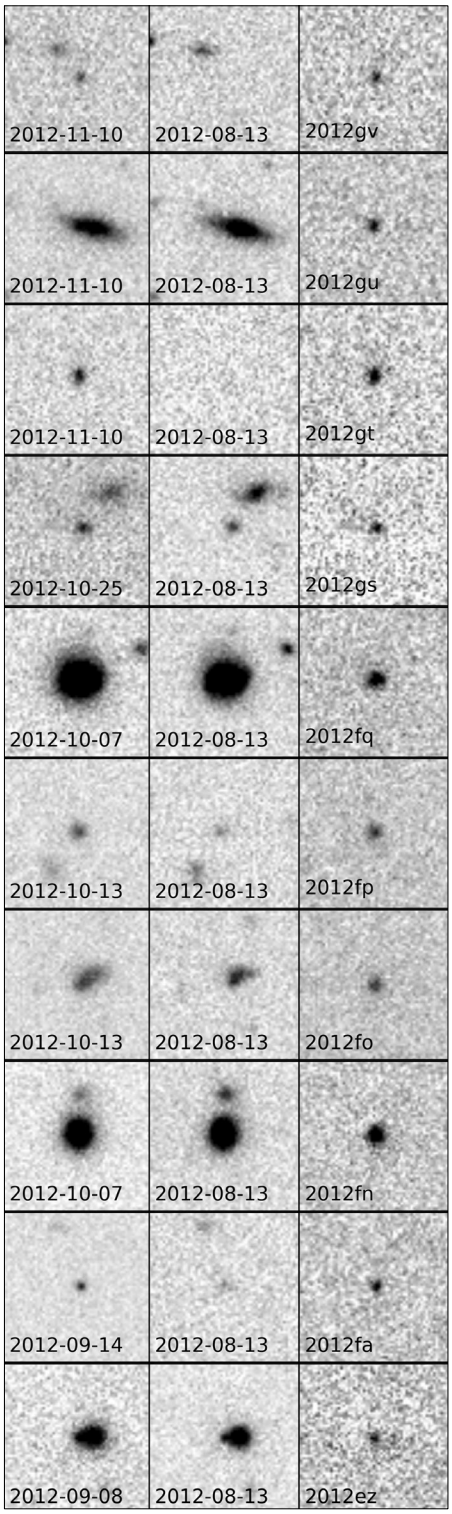

Figure 2. Search image (left panel), template image (centre panel), and difference image (right panel) for the ten SUDARE SNe with spectroscopic classification.

constraining the SN progenitors and investigating a possible evolution of SN diversity with cosmic time. Our goal of measuring SN rates as a function of galaxy age, mass, SFR, metallicity and in different environments requires a detailed characterisation of the galaxy sample surveyed. We therefore decided to search for SNe in two sky fields: the Chandra Deep Field South (CDFS) and the Cosmic Evolution Survey (COSMOS) field. These fields have an extraordinary amount of ancillary data from X-ray to radio wavelengths (e.g., the GALEX Deep Imaging Survey in the ultraviolet, the VISTA–VIDEO ESO public purvey in the near-infrared, the Spitzer–SERVS and Spitzer–SWIRE Surveys in the mid- to far-infrared, the Herschel–HerMES Survey in the far-infrared and submillimetre, and the ATCA–ATLAS Survey in the radio) that will allow us to retrieve important properties of the surveyed galaxies, including redshift, luminosity, morphology, star formation history and mass.

In addition, the VST–Optical Imaging of CDFS and ES1 (VOICE) survey (PIs G. Covone and M. Vaccari) is observing CDFS in the *u*-band and obtaining additional *g*-, *r*- and *i*-band images to improve the accuracy of the photometric redshifts and to estimate galaxy stellar masses, SFRs and environmental properties. The COSMOS field will be also monitored over the next five years in the *Y*-, *J*-, *H*- and *Ks*-bands to unprecedented depth by the UltraVISTA ESO public survey. It will be very interesting to compare the optical and near-infrared SN rates in the same galaxy sample up to redshift 0.3–0.4. This comparison will allow us to estimate the fraction of missed SNe in the optical search due to dust extinction. An important by-product of our search will be the detection of the variability of active galactic nuclei (AGNs) and the gathering of their optical light curves.

Observational strategy

The strategy of the SUDARE survey has been tuned to collect an unbiased and homogeneous sample of all SN types in an unbiased galaxy sample. We are performing a "rolling search", a frequent, long-term monitoring of the selected sky fields, in the *r*- (with a cadence of 2–4 days), *g*- and *i*-bands (with a cadence of one week) to a limiting magnitude of 25 mag. In order to reduce the possible effects due to cosmic variance, the pointing will change by one degree from season to season so that, by the end of the survey we will have covered two square degrees both for the CDFS and COSMOS fields.

The transients are detected in the *r*-band on difference images obtained by subtracting from a given image a template image acquired at a different epoch (see Figure 2 for some examples). The magnitude limit in the difference image is about 24 mag depending on the quality of the search image and the brightness of the host galaxy in the transient location. Images in *g*- and *i*-bands will provide colour evolution for each transient. A rolling search secures photometric typing for each transient that will be validated by spectroscopic classification for a fraction (30 %) of the SN candidates, obtained through dedicated programmes at 8-metre-class telescopes such as the VLT, Magellan and Gemini South.

A key feature of our strategy is the very rapid turnaround from observation to transient detection. This can be accomplished because of the excellent services offered by ESO, beginning with service observing mode, which is crucial for our programme. This is accompanied by real-time archive ingestion and delivery along with access to a mature tool for VST data reduction (VST-Tube; Grado et al., 2012). As a result we are in the position to obtain spectroscopic classification for transient events within 24 hours of their detection.

The first SNe are coming out ... and it is only the beginning!

SUDARE started on 20 October 2011 and has imaged CDFS in 55 epochs (ESO Periods 88, 89 and 90) exploiting VST and OmegaCAM guaranteed observing time (PI Cappellaro) and imaged the COSMOS field in 30 epochs (ESO Period 88: PI Pignata). So far we

have discovered a hundred SN candidates, several variable AGNs and a number of variable stars. In three different nights we obtained spectroscopic classification for a dozen of the SN candidates at the VLT, equipped with the FOcal Reducer and low dispersion Spectrograph and at Gemini-South, equipped with the Gemini Multi-Object Spectrograph. These SNe are reported in the Central Bureau for Astronomical Telegrams (CBET) 3236, 3274, 3311. Six of these SNe are Type Ia with an average redshift of 0.5 (Figure 3 shows the light curve and spectrum of one example, SN 2012gs at z = 0.52), two are Type Ic (Figure 4 shows the light curve and spectrum of SN 2012fn, a Type Ic at z = 0.28) and two are Type II in a redshift range from 0.3 to 0.6. Classifications were performed with the GELATO tool (Harutyunyan et al., 2008).

Four transients were discovered within 0.1 arcseconds from the host galaxy nuclei and all exhibited the spectrum of a Seyfert galaxy. All the SNe were discovered well before maximum light thanks to the temporal cadence of our survey that allows both an early discovery and an optimal photometric coverage. The distribution in redshift, magnitude and SN type of this subsample with spectroscopic classification is in excellent agreement with that expected from our simulations (Figure 1).

The first systematic SN search began about 80 years ago by F. Zwicky at Mount Palomar with a Schmidt telescope (with a field of view of several degrees) equipped with photographic plates. SN candidates were searched for by scanning by eye two overlapped plates acquired on different nights, and over a thousand images were inspected to find only a dozen SNe. In a single image of OmegaCAM with SUDARE, the improved magnitude limit now allows us to detect the same number of SNe. This extraordinary improvement is due to modern CCD mosaic cameras, adaptive optics and the subtraction process of digital images, allowing us to discover faint transients also in distant galaxies. The authors of this paper consider it a privilege to have started an SN search in 2011 and they all agree that the acronym SUDARE (in Italian this word means “to exude sweat”) would have been more appropriate for Zwicky’s survey.

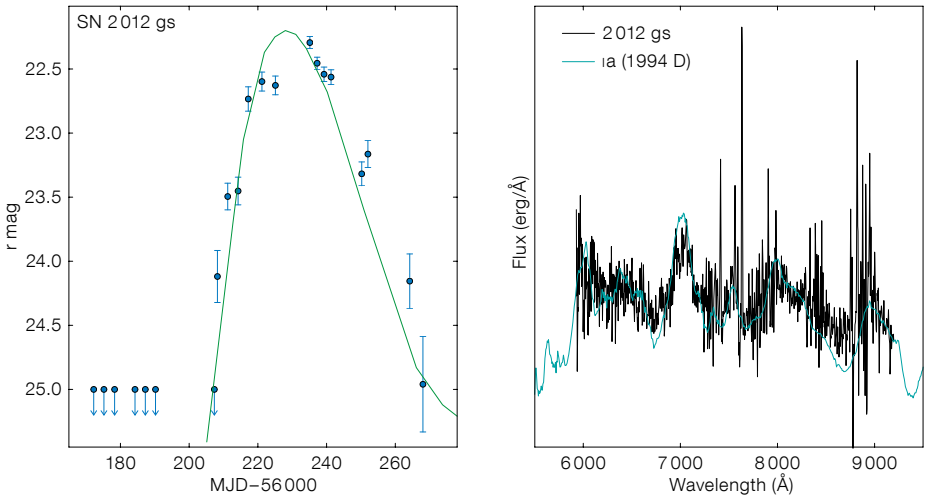

Figure 3. Light curve and spectrum of SN 2012gs, a Type Ia at z = 0.52 discovered by SUDARE. The green spectrum is the best-fit template obtained by GELATO.

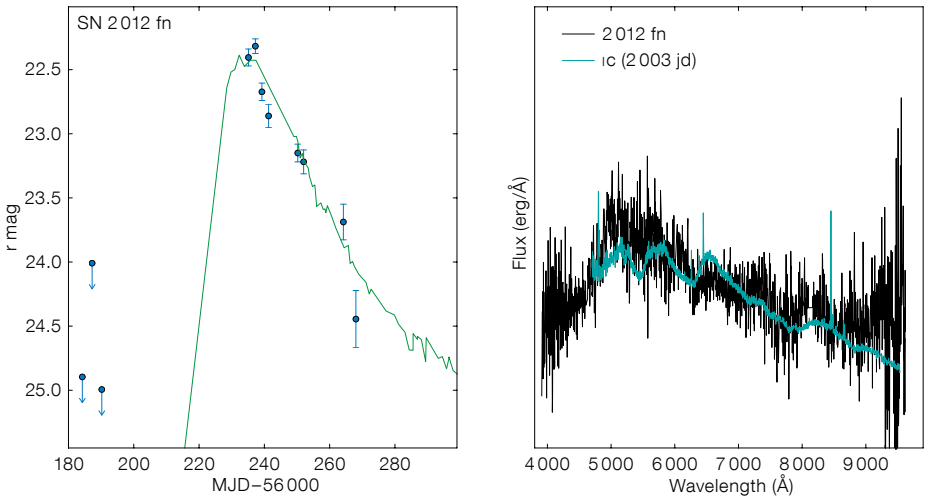

Figure 4. Light curve and spectrum of SN 2012fn, a Type Ic at z = 0.28 discovered by SUDARE. The green spectrum is the best-fit template obtained by GELATO.

References

Benetti, S. et al. 2005, APJ, 623, 1011
Botticella, M. T. et al. 2008, A&A, 479, 49
Botticella, M. T. et al. 2012, A&A, 537, 132
Capaccioli, M. & Schipani, P. 2011, The Messenger, 146, 2
Cappellaro, E. et al. 2005, A&A, 430, 83
Grado, A. et al. 2012, MSAIS, 19, 362
Greggio, L. 2010, MNRAS, 406, 22
Harutyunyan, A. et al. 2008, A&A, 488, 383
Kuijken, K. 2011, The Messenger, 146, 8
Li, W. et al. 2011, MNRAS, 412, 1441
Perlmutter, S. et al. 1998, Nature, 391, 51
Riess, A. et al. 1998, AJ, 116, 1009
Smartt, S. J. et al. 2009, MNRAS, 395, 1409
Turatto, M. et al. 2003, ESO Astrophysics Symposia, eds. Hillebrandt, W., Leibundgut, B. (Heidelberg: Springer-Verlag)

Disentangling the Kinematics and Stellar Populations of Counter-rotating Stellar Discs in Galaxies

Lodovico Coccato[1]
Lorenzo Morelli[2, 3]
Alessandro Pizzella[2, 3]
Enrico Maria Corsini[2, 3]
Lucio Maria Buson[3]
Elena Dalla Bontà[2, 3]

[1] ESO
[2] Dipartimento di Fisica e Astronomia "G. Galilei", Università degli Studi di Padova, Italy
[3] INAF–Osservatorio Astronomico di Padova, Italy

Spectroscopic VIMOS/IFU observations are presented for three galaxies known to host two stellar counter-rotating discs of comparable sizes. For the first time both the kinematics and stellar population properties of the two counter-rotating discs in the observed galaxies were separated and measured. The secondary, less massive, stellar component rotates in the same direction as the ionised gas and is on average younger and less metal-rich than the main galaxy disc. These results support the scenario of gas accretion followed by star formation as the origin for large counter-rotating stellar discs in galaxies, and set an upper limit of 44% to those formed by binary galaxy mergers.

Counter-rotating galaxies

Counter-rotating galaxies are those that host two components that rotate in opposite directions to each other. These peculiar objects have been observed in all morphological types, from ellipticals to spirals. They are classed by the nature (stars *vs.* stars, stars *vs.* gas, gas *vs.* gas) and size (counter-rotating cores, rings, discs) of the counter-rotating components (see Bertola & Corsini [1999] for a review). In this work, we investigate the peculiar class of counter-rotating galaxies with two counter-rotating stellar discs of comparable size. The prototype of this class of objects is the famous E7/S0 galaxy NGC 4550, whose counter-rotating nature was first discovered by Rubin et al. (1992). To date, there are only a few known counter-rotating galaxies similar to NGC 4550, but the census will increase as a result of the new two-dimensional spectroscopic surveys.

Different scenarios have been proposed to explain the formation of these peculiar objects. The internal origin scenario (Evans & Collett, 1994) describes the dissolution of a triaxial potential or a bar. In this process, the stars, moving on box orbits, escape from the confining azimuthal potential well and move onto tube orbits. During this process, half of the box-orbit stars are scattered onto clockwise-streaming tube orbits, the other half onto counterclockwise ones. In this way, two identical counter-rotating stellar discs can be built. In the gas accretion scenario, a disc galaxy acquires gas from extragalactic reservoirs onto retrograde orbits (e.g., Pizzella et al., 2004). If the amount of acquired gas is sufficiently large, the new gas drives away the pre-existing gas and it settles onto a counter-rotating disc. New stars are then born from the acquired gas, forming the counter-rotating stellar disc. In the binary merger scenario (e.g., Crocker et al., 2009), two disc galaxies with opposite spin directions collide and form two coplanar counter-rotating stellar discs, depending on the geometry of the encounter.

These different formation mechanisms are expected to leave differing signatures in the properties of the stellar populations of the counter-rotating component. In particular, age is a key element in differentiating among these scenarios. The internal origin predicts the same mass, luminosity, chemical composition and age for both counter-rotating stellar components. Gas acquisition followed by star formation predicts younger ages for the counter-rotating stellar component in all cases, and it allows for different metallicity and α-enhancement between the two discs. Direct acquisition of stars through mergers also allows for different metallicity and α-enhancement, but the younger component will be determined by the difference in age between the host galaxy and the merged system. Roughly, one would expect younger counter-rotating stars in ~ 50% of the cases.

A proper spectroscopic decomposition that separates the relative contribution of the two counter-rotating stellar components to the observed galaxy spectrum is therefore needed. In this way, the kinematics and the stellar populations of both the stellar components can be measured simultaneously, allowing the different formation scenarios to be disentangled.

Results of the spectroscopic observations

We started an observational campaign with the integral field unit (IFU) of the VIMOS spectrograph at the VLT aimed at determining the most efficient mechanisms in building large-scale counter-rotating stellar discs, like those observed in NGC 4550. For this study, we developed a new spectroscopic decomposition technique that fits a galaxy spectrum and separates the contributions of two counter-rotating stellar components (Coccato et al., 2011). At each position on the sky, the code builds two synthetic templates (one for each stellar component) as a linear combination of spectra from an input stellar library, and convolves them with two Gaussian line-of-sight velocity distributions with different kinematics. Gaussian functions are also added to the convolved synthetic templates to account for ionised gas emission lines (Hγ, Hβ, [O III] and [N I]).

The spectroscopic decomposition code returns the spectra of two best-fit synthetic stellar templates and ionised gas emission (Figure 1), along with the best-fitting parameters of luminosity fraction, velocity and velocity dispersion. The line strengths of the Lick indices of the two counter-rotating components are measured on the two best-fit synthetic templates. We then compare the indices Hβ, Mgb, Fe5270, and Fe5335 to the predictions of stellar population models to infer the stellar age, metallicity ([Z/H]), and abundance ratio of α-elements ([α/Fe]) of the two counter-rotating discs. We also computed the mass-to-light ratios and the mass fraction of the two counter-rotating components from the luminosity fraction and the inferred stellar population parameters. The estimated mass is used to determine which component is the main (i.e., the most massive) and which is the secondary (i.e., the least massive).

We started this project (programme IDs: 383.B-0632 and 087.B-0853A) by observing with VIMOS/IFU three galaxies that were known to host counter-rotating stellar discs of comparable size: NGC 3593 (Bertola et al., 1996), NGC 4550 (Rubin et al., 1992) and NGC 5719 (Vergani et al.,

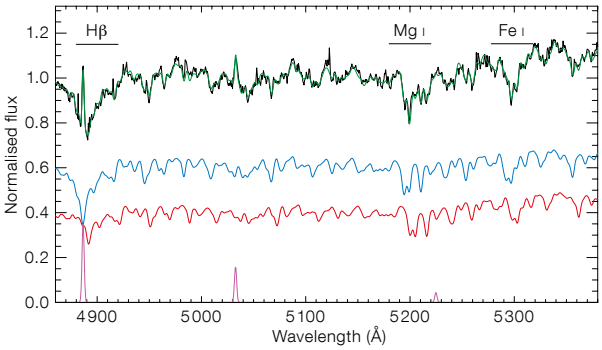

Figure 1. Fit of the galaxy spectrum (black) in a spatial bin. The best-fitting model (green) is the sum of the spectra of the ionised gas component (magenta) and the two stellar components (blue and red). The differences in the position of absorption line features and in the Hβ equivalent widths between the two stellar components (indicating different kinematics and stellar population content) are clearly evident.

Table 1. Luminosity-weighted values for the stellar population parameters of the stellar discs.

	Age [Gyr]	[Z/H]	[α/Fe]
NGC 3593			
Main:	3.6 ± 0.6	−0.04 ± 0.03	0.09 ± 0.02
Secondary:	2.0 ± 0.5	−0.15 ± 0.07	0.18 ± 0.03
NGC 4550			
Main:	6.9 ± 0.6	−0.01 ± 0.03	0.20 ± 0.02
Secondary:	6.5 ± 0.5	−0.13 ± 0.04	0.28 ± 0.02
NGC 5719			
Main:	4.0 ± 0.9	0.08 ± 0.02	0.10 ± 0.02
Secondary:	1.3 ± 0.2	0.3 ± 0.02	0.14 ± 0.02

2007). The combination of the collecting power of an 8-metre-class telescope, the large wavelength coverage (4150–6200 Å) and the high spectral resolution (full width half maximum [FWHM] of 2.0 Å) with the HR-blue grism makes VIMOS on the VLT the best-suited integral field unit for this kind of study.

In all the sample galaxies, we confirm the presence of two stellar discs of comparable size, and one ionised gas component. The secondary stellar component and the ionised gas component counter-rotate with respect to the main stellar disc. Moreover, in all the observed galaxies, these counter-rotating secondary components are younger, more metal-poor, and have higher abundances of α-elements than the main stellar discs.

Table 1 summarises the mean properties of the two counter-rotating stellar populations, and Figures 2, 3 and 4 illustrate our results. In these figures, the extension of the VIMOS/IFU field of view is plotted over the galaxy image (upper-left panels). The collected spectra are then spatially binned over the field of view with the Voronoi binning technique to increase the signal-to-noise ratio (see Coccato et al. [2013] for further details). The spectral decomposition technique is then applied on the spectrum of each spatial bin to measure the kinematics and the Lick indices of the fitted components. The measured kinematics are used to construct the two-dimensional velocity fields, where the structure of the adopted spatial binning is still visible, and the counter-rotation between the two stellar components is remarkable (lower panels). The Lick indices are shown in the diagnostic plots (upper right panels) with the predictions of single stellar population models (Thomas et al., 2011). We use Hβ and the combined [MgFe]′ = √(Mgb · [0.82 · Fe5270 + 0.28 · Fe5335]) index as indicator of stellar age and metallicity. We also take into account the variation in the abundance of α-elements and metallicity by measuring

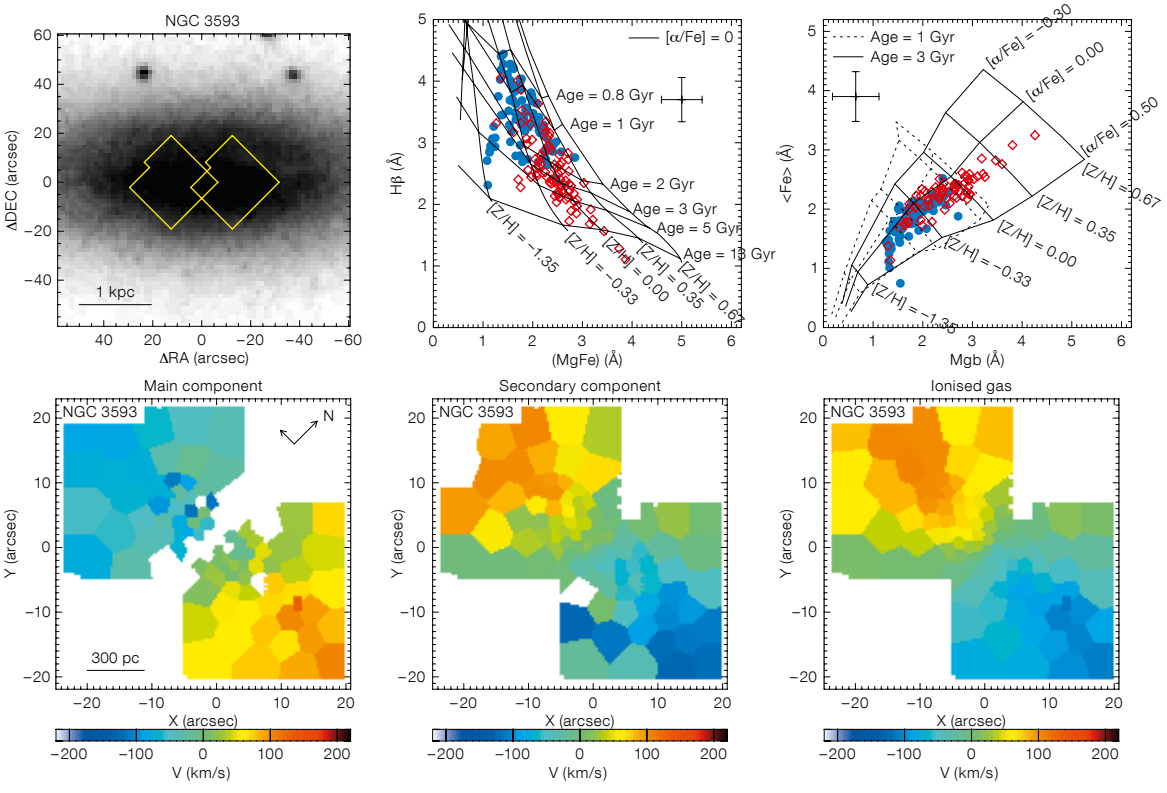

Figure 2. Results of the spectroscopic decomposition of NGC 3593. The top left panel shows the galaxy image with the location of the VIMOS observed field of view. The bottom panels show the two-dimensional kinematics of the main, secondary and ionised gas components, respectively. The top-right panels show the measured equivalent width of the Lick indices; grids with the predictions from single stellar population models are also shown. The crosses on the top-right side of the panels show the mean error bars on the measured indices. Each spatial bin returns two sets of Lick indices, one for each stellar component: red symbols represent the main stellar component, whereas blue symbols represent the secondary counter-rotating component.

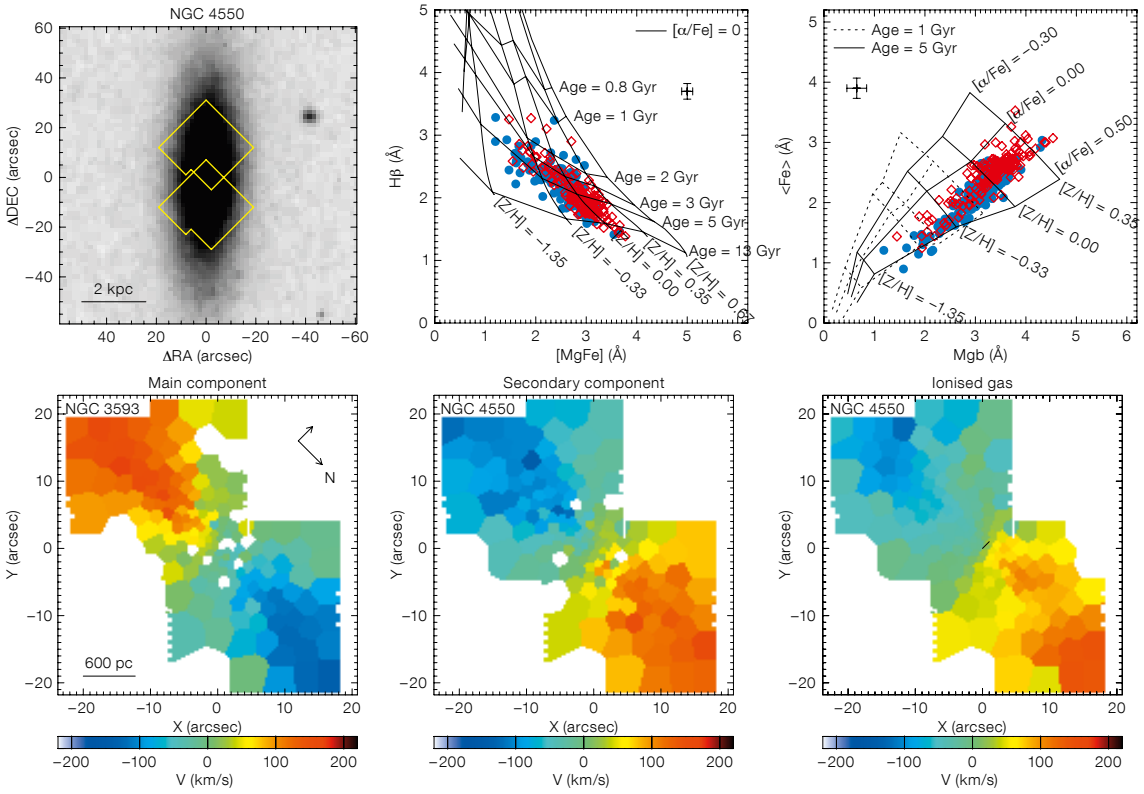

Figure 3. As Figure 2, but for NGC 4550.

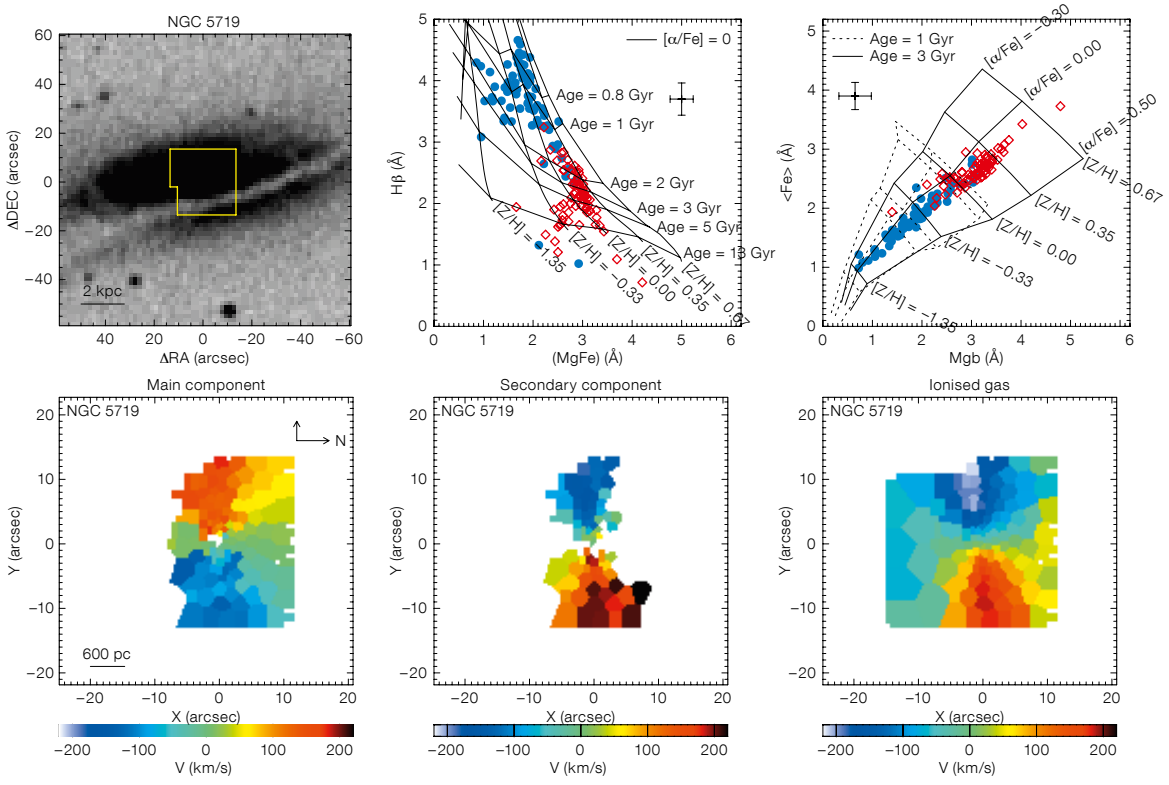

Figure 4. As Figure 2, but for NGC 5719.

the magnesium Mgb index and the mean iron index <Fe> = (Fe5270 + Fe5335)/2.

NGC 3593. An isolated, highly inclined, S0/a spiral at a distance of 7 Mpc. It is characterised by a patchy spiral dust pattern in the centre. The two counter-rotating stellar discs have different scale lengths, but the same intrinsic flattening. The secondary component dominates the innermost 500 pc. The ages of the two components date the accretion event to between 2.0 and 3.6 Gyr ago, i.e., 1.6 ± 0.8 Gyr after the formation of the main stellar disc (Coccato et al., 2013).

NGC 4550. An E7/S0 galaxy in the Virgo Cluster, at a distance of 16 Mpc, and it is often indicated as the prototype of galaxies with counter-rotating stellar discs. It has an elliptical galaxy nearby, NGC 4551, to the northeast of NGC 4550 at a projected distance of 14 kpc. An interaction in the past between these two systems could have produced the counter-rotating stellar disc in NGC 4550, although no photometric signatures of the interaction, such as tidal tails or gas streams, have been detected. The two counter-rotating stellar discs in NGC 4550 have the same scale lengths, but slightly different ellipticity (ε_{main} = 0.6, ε_{second} = 0.5) meaning that they have different scale heights. The measured ages date the accretion event ~ 7 Gyr ago, i.e. less than 1 Gyr after the formation of the main stellar disc (Coccato et al., 2013).

NGC 5719. An Sab galaxy at a distance of 23 Mpc, and a member of a rich group. It is currently interacting with the Sbc galaxy NGC 5713, which is to the west of NGC 5719 at a projected distance of 77 kpc. The interaction between the two systems is traced by a bridge of neutral hydrogen (Vergani et al., 2007), which fuels the secondary counter-rotating stellar component in NGC 5719. The two stellar components in NGC 5719 have similar luminosity, but the secondary is less massive because of its younger age. Moreover, the youngest ages are observed in the secondary component at ~ 700 pc from the centre, where the Hβ emission lines are more intense (Coccato et al., 2011). The ages of the two components date the accretion event between 1.3 and 4.0 Gyr ago, i.e. 2.7 ± 0.9 Gyr after the formation of the main stellar disc (Coccato et al., 2011).

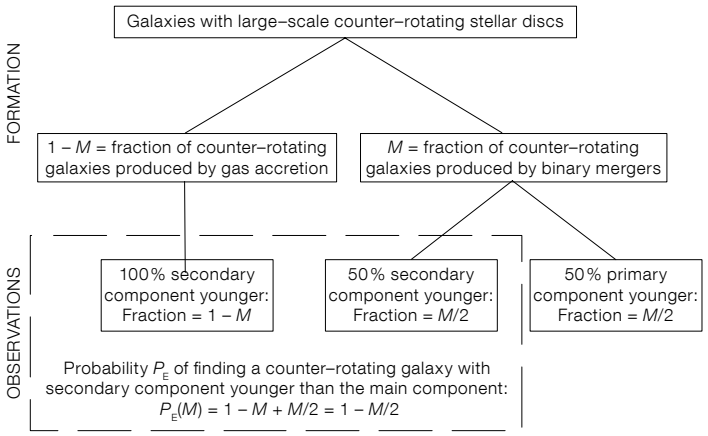

Figure 5. Schematic representation of the probability P_E of observing the secondary stellar disc younger than the main galaxy disc, as a function of the fraction M of galaxies formed through the binary galaxy merger scenario.

The most efficient mechanism to build counter-rotating stellar discs

Our results favour the external origin of the counter-rotating components in all the three observed galaxies, and discard the internal origin scenario. As stated above, in the gas-accretion scenario the stellar component associated with the ionised gas is predicted to always be younger than the main stellar component. In binary galaxy mergers instead, one would expect that the younger stellar component is associated with the ionised gas only in 50% of the cases. Although we always observe the secondary component to be younger than the main galaxy disc, thus favouring the gas accretion scenario, we cannot rule out the binary galaxy merger scenario.

On the other hand, we can infer an upper limit to the fraction of galaxies with two counter-rotating stellar discs that were formed by binary mergers by statistical arguments. We define M as the fraction of galaxies hosting two counter-rotating stellar discs of comparable sizes that were generated by a binary major merger (thus, $(1 - M)$ is the fraction produced by gas accretion), and E as the event of finding the stellar component co-rotating with the gas to be the youngest. The probability P_E to observe E is: $P_E = 1 - M/2$ (see Figure 5). The probability $\Pi_E(M)$ of observing E in exactly N galaxies out of a sample of T counter-rotating galaxies is given by the first term of the binomial distribution. It is therefore possible to compute the most probable value for the fraction of counter-rotating galaxies produced by binary mergers, M_{MAX}, simply by maximising $\Pi_E(M)$. In our case $N = T = 3$, therefore $M_{MAX} < 44\%$ at 1σ confidence level.

Thus, it is fundamental to measure the difference in ages of the counter-rotating components in a larger sample of counter-rotating galaxies to identify the most efficient mechanism and derive more precise constraints. Large spectroscopic surveys like MaNGA will help to identify other potential candidates by recognising the kinematic signatures of stellar counter-rotating discs, such as the two symmetric peaks in the velocity dispersion map. The MaNGA survey is one of the Next Generation Sloan Digital Sky Surveys, and it will collect IFU spectroscopic data for ~ 10 000 galaxies in the nearby Universe within six years. Moreover, the next generation integral field unit MUSE at the VLT will represent a significant step forward for these studies, because of the better spectral resolution, wavelength coverage and field of view with respect to VIMOS.

References

Bertola, F. & Corsini, E. M. 1999, IAU Symposium, 186, *Galaxy Interactions at Low and High Redshift*, eds. Barnes, J. E. & Sanders, D. B. (Dordrecht: Kluwer), 149
Bertola, F. et al. 1996, ApJ, 458, L67
Coccato, L. et al. 2011, MNRAS, 412, L113
Coccato, L. et al. 2013, A&A, 549, 3
Crocker, A. F. et al. 2009, MNRAS, 393, 1255
Evans, N. W. & Collett, J. L. 1994, ApJ, 420, L67
Pizzella, A. et al. 2004, A&A, 424, 447
Rubin, V. C., Graham, J. A. & Kenney, J. D. P. 1992, ApJ, 394, L9
Thomas, D., Maraston, C. & Johansson, J. 2011, MNRAS, 412, 2183
Vergani, D. et al. 2007, A&A, 463, 883

Angular Momentum of Galaxies in the Densest Environments: A FLAMES/GIRAFFE IFS Study of the Massive Cluster Abell 1689 at z = 0.18

Francesco D'Eugenio[1]
Ryan C. W. Houghton[1]
Roger L. Davies[1]
Elena Dalla Bontà[2, 3]

[1] Sub-department of Astrophysics, Department of Physics, University of Oxford, United Kingdom
[2] Dipartimento di Fisica e Astronomia "G. Galilei", Università degli Studi di Padova, Italy
[3] INAF–Osservatorio Astronomico di Padova, Italy

Early-type galaxies (ETGs) exhibit kinematically distinct slow and fast rotator (SR, FR) morphologies. The former are much less common (10 % of ETGs), but their incidence is higher in the core of the Virgo Cluster (25 %). Here we present FLAMES/GIRAFFE integral field spectroscopy of 30 galaxies in the massive cluster Abell 1689 at z = 0.183. Abell 1689 has a density 30 times higher than that of Virgo, making it the ideal place to test the effects of environment, such as local density and cluster properties. We find 4.5 ± 1.0 SRs (or an average ETG fraction, f_{SR}, of 0.15 ± 0.03) in Abell 1689, identical to the value for field/groups in ATLAS^{3D}. Within Abell 1689 f_{SR} increases towards the centre, exceeding the value found in the core of Virgo. This work is the highest redshift study of its kind.

Kinematical classification of ETGs

ETGs comprise morphologically distinct elliptical (E) and lenticular (S0) galaxies. Despite their differences, Es and S0s have lots in common. They are both characterised by old stellar populations, which has earned them the attribute "early-type". The average ETG has little or no cold gas, which is reflected in the star formation rate. Its light profile is smooth and its shape fairly regular. One of the most puzzling facts about these galaxies is how, with masses and luminosities that span several orders of magnitude, they obey a number of tight scaling relations. These include the colour–magnitude relation, the colour–σ and Mg–σ relations (where σ is the velocity dispersion) and the fundamental plane. The mere existence of these empirical laws — alongside their very small scatter — imposes strong constraints on the structure and evolution of ETGs (Bower et al., 1992). This makes them ideal testing grounds for any galaxy formation theory. Their study, important in its own right, is also fundamental for our understanding of the process of structure formation in the Universe.

The advent of integral field spectroscopy (IFS) started a revolution in the study of ETGs. The SAURON survey discovered the existence of two kinematically distinct classes of ETGs, slow and fast rotators (SRs and FRs, see Emsellem et al. [2007]) and Cappellari et al. (2007). The former have little or no rotation, exhibit kinematically decoupled cores and misalignment between kinematics and photometry. The latter are flattened systems, compatible with rotational symmetry and a disc-type origin. The new division crucially crosses the boundary between Es and S0s, in that FRs populate both morphological classes. ATLAS^{3D} (the volume-limited follow-up survey to SAURON; Cappellari et al., 2011a; Emsellem et al., 2011), established that 66 % of morphological ellipticals are FRs, and thus share the same internal structure as S0s. This is evidence for a new classification paradigm, based on kinematics rather than morphology (Cappellari et al., 2011b).

The ATLAS^{3D} team presented the kinematic morphology–density (kT–Σ) relation, analogous to the morphology–density relation (Dressler, 1980). It links the fraction of SRs in the ETG population (f_{SR}) with the local number density of galaxies: they found that f_{SR} is independent of the environment density over five orders of magnitude from field to group environments. But they noticed a sharp increase in f_{SR} in the inner core of the Virgo Cluster, the highest density probed by the ATLAS^{3D} survey. Virgo is an unrelaxed, low-density cluster, but what would be measured in the denser environments beyond the local Universe? Addressing this question gives further insight on the kT–Σ relation, and on the processes that drive galaxy formation and evolution.

Since rich, relaxed clusters are rare, they can only be found at higher redshifts. The multiplexing capabilities of FLAMES/GIRAFFE (Pasquini et al., 2002), combined with the collecting power of the ESO Very Large Telescope (VLT), are the ideal tools for this task.

FLAMES/GIRAFFE observations of Abell 1689

Abell 1689, a massive galaxy cluster at redshift z = 0.183, has regular, concentric X-ray contours suggesting that it is relaxed. Its X-ray luminosity outshines Coma by a factor of three, and Virgo by over an order of magnitude. Its comoving distance is 740 Mpc, giving a scale of 1 arcsecond per 3.0 kpc. Alongside its physical properties, Abell 1689 was an ideal target for FLAMES because the spatial resolution of the GIRAFFE-deployable integral field units (IFUs) samples up to one effective radius (R_e) for most galaxies. Finally, a wealth of archival data, including imaging from the Hubble Space Telescope (HST) Advanced Camera for Surveys (ACS), is available and vital to a study of this nature.

F625W-band imaging from the HST ACS, combined with g'- and r'-band GEMINI imaging were used for the photometry (Houghton et al., 2012). The spectroscopic data (spectral resolution, R = 11 800, spectral range 573 nm < λ < 652 nm [486 nm < λ < 552 nm rest frame]) covers standard V-band absorption features. GIRAFFE provides 15 independent mini IFUs, deployable anywhere on the focal plane; each IFU is positioned by a magnetic button and contains an array of 20 square microlenses. They are arranged in four rows of six (with four "dead" corners) for a total field of view of 3 by 2 arcseconds. Each lenslet is then connected to the spectrometer with a dedicated optical fibre bundle. Alongside the 15 IFUs, the instrument also provides 15 fully deployable sky fibres.

Since the magnetic buttons are larger (10 arcseconds) than the IFU field of view, they cannot be deployed closer than a minimum distance of 11 arcseconds. GIRAFFE permits the observer to target 15 objects simultaneously and we chose to target 30 galaxies as a compromise between sample statistics and integration time. In order to gain the maximum possible signal-to-noise ratio, we initially selected the 30 ETGs with the highest

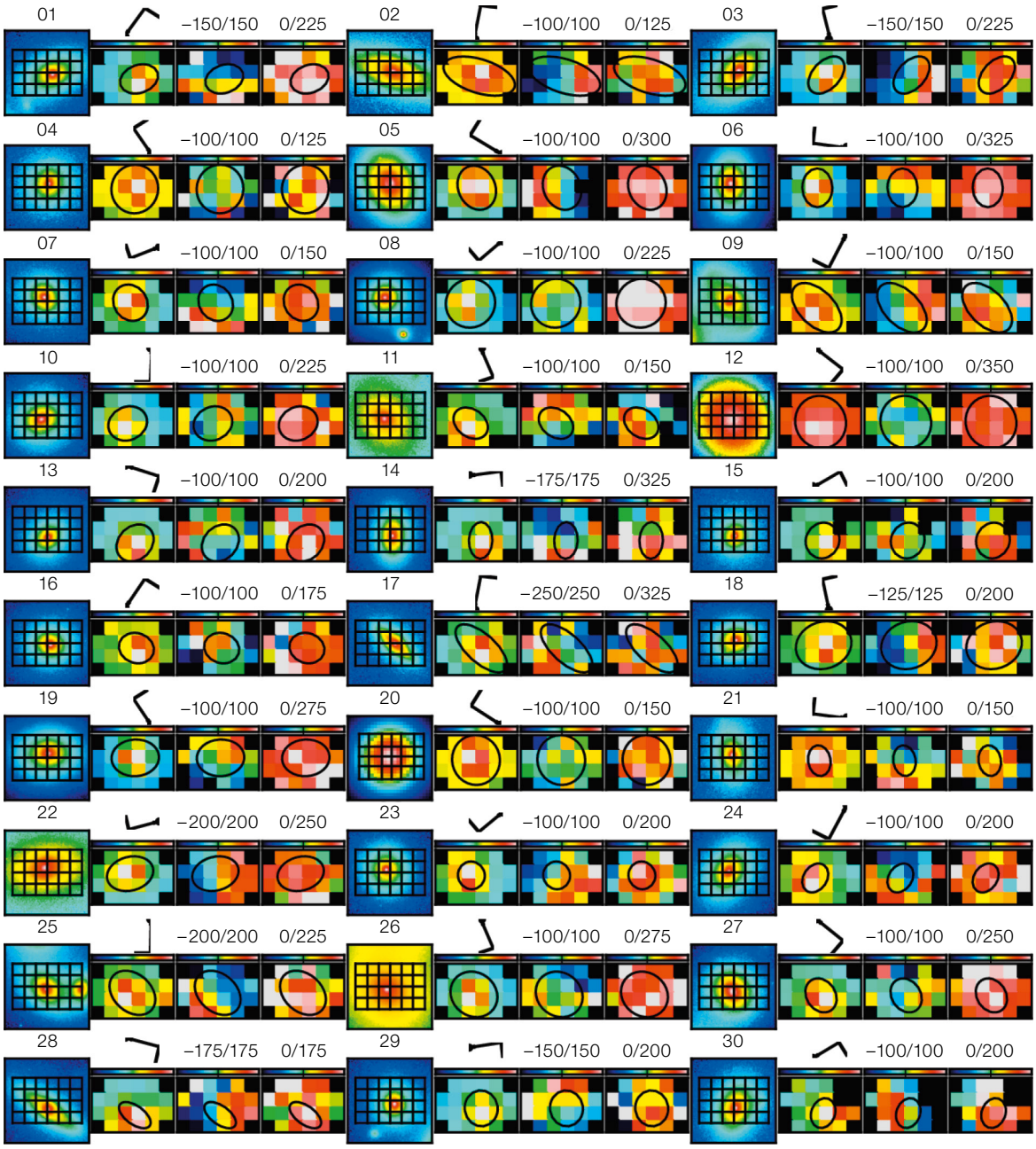

Figure 1. Kinematic maps of the Abell 1689 sample. For each of the 30 galaxies in the sample we present a set of four images. The first one shows FLAMES/GIRAFFE IFU footprints superimposed on HST imaging (Gemini imaging for target 20). The second plot shows the reconstructed image from VLT integral field spectroscopy, where each square is a spaxel and corresponds to a lenslet of the IFU. Also shown is an isophote at either R_e, or the closest integer fraction that fits into the IFU footprint. The four black corners correspond to unavailable "dead" spaxels, while other black spaxels (seen in 11, 15 and 30) correspond to broken or unused fibres. Velocity and velocity dispersion maps are depicted in the third and fourth plots. The black compass arrows show north and east directions. Colour-bar limits are given in km/s.

surface brightness within a 3-arcsecond radius. This sample was then subject to two practical constraints. We needed all of our targets to have high-resolution HST imaging, which limited our choice to candidates in the innermost regions of the cluster. The 11-arcsecond proximity constraint ruled out some targets in the most crowded regions, forcing us to re-select from a reserve list. This left us with 29 galaxies inside the HST field of view and one outside (galaxy 20). Each plate was exposed five times for two hours, for a total of ten hours per galaxy. The observations were carried out in visitor mode, which proved to be both efficient and accurate in terms of object acquisition. Excellent seeing of 0.60 arcseconds reduced the correlation between neighbouring spaxels.

Our sample is biased towards bright objects, which in turn could bias us to detect more SRs. We simulated observations of the Virgo Cluster (for which the SR population is known from ATLAS^{3D}) using the luminosity function of our sample. This showed that we could recover the true value of f_{SR} for Abell 1689. Although we did not do a colour selection, our sample falls entirely on the Red Sequence (RS). However, the number of galaxies that do not fall on the RS in Abell 1689 is extremely low, and we found the bias to be minimal.

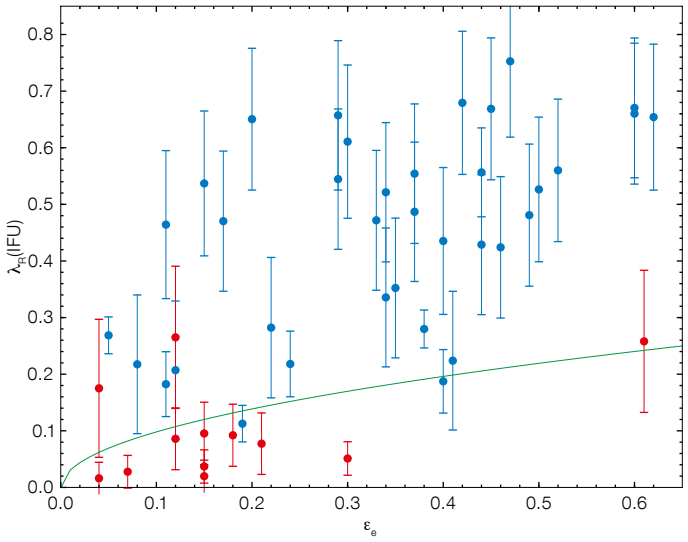

Figure 2. λ_R(IFU) *vs.* ε_e for the simulated observations of the SAURON sample of galaxies. The green lines separate SRs (below) from FRs. Red and blue circles denote SRs and FRs respectively, according to the original SAURON classification (Emsellem et al., 2007). Due to the different observing setup, some galaxies have been misclassified: these are the red dots above the green line and the blue dots below.

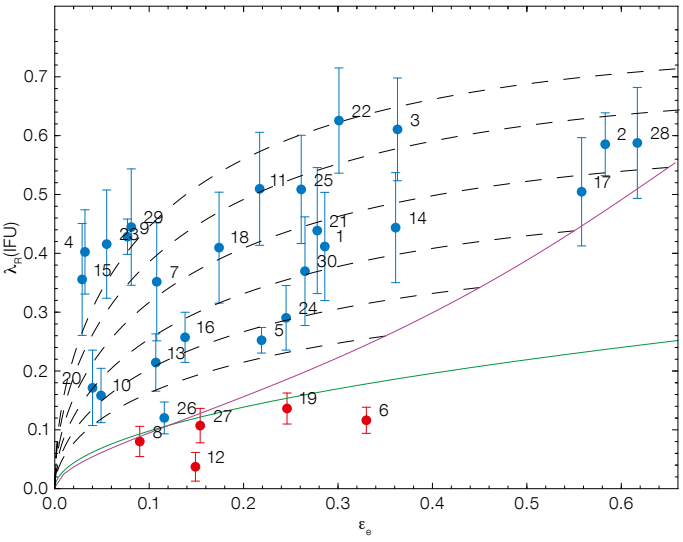

Figure 3. λ_R(IFU) *vs.* ε_e for all target galaxies in Abell 1689. The green line separates FRs (blue dots above) from SRs (red dots below). The magenta and dashed lines represent the view of an axisymmetric galaxy, edge-on and at various inclinations. Details about these models are given in Cappellari et al. (2007) and Emsellem et al. (2011).

To reduce the FLAMES/GIRAFFE data we used the official ESO pipeline[1], following the guidelines ESO offers[2]. Stellar kinematics were extracted using pPXF[3]; we used a line-of-sight velocity dispersion (LOSVD) expressed by a Gaussian function, obtaining just the velocity V and velocity dispersion σ. The stellar template library of choice was the high-resolution version (R = 40 000) of the ELODIE template library[4].

Slow and fast rotators at z = 0.18

Figure 1 shows the resulting kinematic maps. Although the spatial resolution is low (compared to SAURON) rotation can be clearly seen in some galaxies, and not in others.

Since our spatial resolution is coarse, we cannot detect kinematically decoupled cores (KDCs) and double σ peaks (2σ) as in Krajnovíc et al. (2011). If we try to detect SRs from the velocity maps by eye (as done by the SAURON and ATLAS^{3D} teams) we identify at most six: galaxies 4, 8, 12, 20, 26 and 27 (see Figure 1). The overall value of f_{SR} in the sample would then be 0.20, in line with what was found in the Virgo core (Cappellari et al., 2011b). However, contamination from face-on discs, which may appear as SRs, can bias the estimate.

Five more objects, despite exhibiting large-scale rotation, have misaligned kinematic and photometric axes, a feature more common in SRs than in FRs (Krajnovíc et al., 2011): these are galaxies 1, 3, 5, 9, 17 and 25 (Figure 1). Galaxies 3 and 17 have very high ellipticities, and are thus unlikely to be SRs, which have ellipticity $\varepsilon < 0.4$. Galaxy 5 has high velocity dispersion, and also contains an inner disc (R = 1.5 kpc) in the HST imaging.

λ_R measurements and kinematic classification

Emsellem et al. (2007) introduced the estimator λ_R to measure the projected specific angular momentum of galaxies; and Emsellem et al. (2011) further show how the combination of λ_R and ε conveniently captures the kinematic boundary between SRs and FRs. They define $\lambda_R(R_e)$ as the value of λ_R computed inside R_e, and use it in their $\lambda_R(R_e)$ *vs.* ε diagram.

In our study the galaxies are not sampled evenly, because R_e varies while the size of the IFUs is fixed. We cannot follow the ATLAS^{3D} prescription precisely and therefore introduced λ_R(IFU); defined as the value of λ_R computed using all the available spaxels in the IFU field of view. This introduces additional differences between our setup and that of ATLAS^{3D}, but we used existing SAURON data to determine how our observations and definition compare to those of ATLAS^{3D}. We made models of the SAURON galaxies using kinemetry[5] and, after projecting at redshift z = 0.183 and convolving with the seeing, we sampled them using the FLAMES/GIRAFFE setup. The resulting simulated data, after adding noise, have been used to measure λ_R, which we then compared with the original SAURON values to estimate both bias and systematic error.

We corrected λ_R(IFU) according to the bias measured and included the systematic error in quadrature with the random error. This correction takes into account both the different apertures between λ_R(IFU) and $\lambda_R(R_e)$ and the different spatial resolutions between λ_R(IFU) and ε_e. In Figure 2 we plot simulated values of λ_R(IFU) against published values of ε_e (Emsellem et al., 2007). Despite the aforementioned differences, there is little (< 10%) misclassification in our diagram, especially at high values of R_e. Given the known uncertainties, we can calculate the probability distribution for the

measured number of SRs in the SAURON survey (galaxies below the green line in Figure 2 defined by $0.31\sqrt{\varepsilon}$ and the green line in Figure 2, Emsellem et al. [2011]). We adopt a Monte Carlo approach (for each galaxy we assumed Gaussian errors in λ_R). The resulting probability distribution is Gaussian-like and we find 12.3 ± 1.7 slow rotators, where the true value is 12.

When we correct the values for our Abell 1689 data in the same way (Figure 3), we can similarly calculate the probability distribution for the number of SRs in Abell 1689. This analysis finds 4.5 ± 1.0 slow rotators, corresponding to f_{SR} = 0.15 ± 0.03.

Emsellem et al. (2007) warn about using only λ_R to assign a galaxy to either the slow or fast rotator class. The discrepancy between the classification "by eye" and the classification we adopted here underscores that warning. However, when studying galaxies beyond the local Universe, a detailed analysis such as that carried out by the ATLAS^{3D} team is not feasible. We are thus forced to rely on a statistical approach.

Slow rotators and environment density

For each galaxy in the sample we estimate the local environment density following Cappellari et al. (2011b). We define Σ_3 as the number density of galaxies inside the minimum circular area, centred on the target galaxy, and encompassing three other galaxies (down to a magnitude limit). Interlopers were dealt with by subtracting everywhere a constant mean value of Σ_3 = 0.49 galaxies per square arcminute. In Figure 4 we show f_{SR} versus $\log_{10}\Sigma_3$ for Abell 1689 (red), compared to the results of the ATLAS^{3D} survey (green; Cappellari et al., 2011b). The densest environment in ATLAS^{3D} (i.e., the core of the Virgo Cluster) has f_{SR} = 0.25, double that typically found in less dense environments ($f_{SR} \approx 0.12$).

In this study we probed environments with values of $\log_{10}\Sigma_3$ between 2.06 and 3.75: the minimum is comparable to the core of Virgo, and the maximum is 1.7 dex higher. In this respect our work

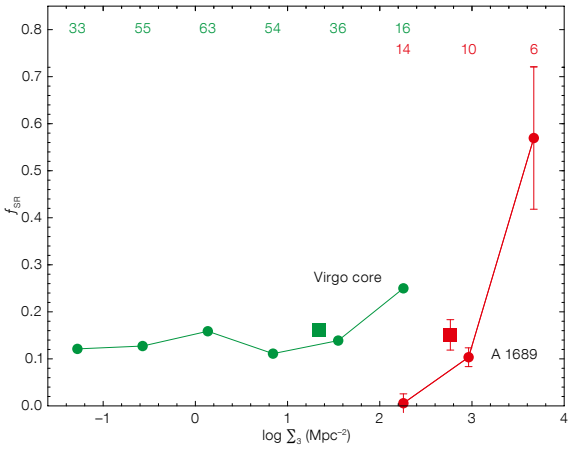

Figure 4. Fraction of slow rotators f_{SR} over the ETG population, as a function of the environment density. The green circles and line are from the ATLAS^{3D} survey (Cappellari et al., 2011b), red symbols are for Abell 1689. The numbers at the top give the total number of galaxies in each bin. The uncertainty in the SR classification is reflected in the error bars. The green square is the value of f_{SR} that we measure, resampling Virgo using our sample luminosity function. The error bars are smaller than the point size. The average fraction for Abell 1689 is shown by the red square.

starts exactly where ATLAS^{3D} finished. Abell 1689 shows a sharp increase in f_{SR} with projected density, from f_{SR} = 0.01 in the least dense environment to f_{SR} = 0.58 in the innermost regions. The densest bin in Abell 1689 has a higher fraction of SRs than the core of Virgo (Figure 4). The intermediate bin has a value of f_{SR} compatible with both the field/group environments and the overall Virgo cluster value, but is less than the Virgo core. f_{SR} in the least dense bin is lower than the ATLAS^{3D} field and group values.

Considering the whole Abell 1689 sample, we find an average value of $\log_{10}\Sigma_3$ = 2.77 and a SR fraction of 0.15 ± 0.03 (red square in Figure 4), which is the same as the overall SR fraction in the Virgo cluster, when sampled in the same way (green square). Furthermore, both values are similar to the field and group samples in ATLAS^{3D}, suggesting little to no difference in f_{SR} when it is averaged over an entire cluster population.

Abell 1689 has a higher average density than Virgo, but the same average slow rotator fraction f_{SR}. Inside the cluster, f_{SR} rises with projected density. In the least dense region, f_{SR} is significantly smaller than the ATLAS^{3D} field/group value. Given the low number of galaxies per bin, we cannot rigorously claim that this is representative. However, a similar "depletion" is observed in the outskirts of the Virgo cluster (Cappellari et al., 2011b). SRs are uniformly distributed across a range of environments; we know that they are on average more massive than FRs, and that dynamical friction is more efficient in objects with mass higher than the average particle mass. Hence the higher f_{SR} in the core of clusters is consistent with the effects of dynamical friction.

On account of the importance of the SR/FR division in understanding galaxy formation/evolution, it is crucial to expand this study, in particular by increasing the number of observed clusters, to quantify the scatter in f_{SR} and the radial variation within different clusters. Sampling clusters with different densities and dynamical states would give us great insight on the topic. Observations of the Abell 1650 cluster, with an intermediate mass, lying between that of Virgo and Abell 1689, are already scheduled at the VLT. Interesting times are ahead!

References

Bower, G., Lucey, J. R. & Ellis, R. S. 1992, MNRAS, 254, 613
Cappellari, M. et al. 2007, MNRAS, 379, 418
Cappellari, M. et al. 2011a, MNRAS, 413, 813
Cappellari, M. et al. 2011b, MNRAS, 416, 1680
Dressler, A. 1980, ApJ, 236, 351
Emsellem, E. et al. 2007, MNRAS, 379, 401
Emsellem, E. et al. 2011, MNRAS, 414, 818
Houghton, R. C. W. et al. 2012, MNRAS, 423, 256
Krajnovíc, D. et al. 2011, MNRAS, 414, 2923
Pasquini, L. et al. 2002, The Messenger, 110, 1

Links

[1] ESO Giraffe Pipeline: http://www.eso.org/sci/software/pipelines/giraffe/giraf-pipe-recipes.html
[2] Guidelines for Giraffe Pipeline: ftp://ftp.eso.org/pub/dfs/pipelines/giraffe/giraf-manual-2.8.7.pdf
[3] pPXF: http://www-astro.physics.ox.ac.uk/~mxc/idl/
[4] Elodie template library: www.obs-u-bordeaux1.fr/m2a/soubiran/elodie_library.html
[5] Kinemetry: www.davor.krajnovic.org/idl

VIPERS: An Unprecedented View of Galaxies and Large-scale Structure Halfway Back in the Life of the Universe

Luigi Guzzo[1]
and the VIPERS Team*

[1] INAF–Osservatorio di Brera, Milano, Italy

The VIMOS Public Extragalactic Redshift Survey (VIPERS) is an ongoing Large Programme to map in detail the large-scale distribution of galaxies at $0.5 < z < 1.2$. With a combination of volume and sampling density that is unique for these redshifts, it focuses on measuring galaxy clustering and related cosmological quantities as part of the grand challenge of understanding the origin of cosmic acceleration. Moreover, VIPERS has been designed to guarantee a broader legacy, allowing detailed investigations of the properties and evolutionary trends of $z \sim 1$ galaxies. The survey strategy exploits the specific advantages of VIMOS, aiming at a final sample of nearly 100 000 galaxy redshifts to $i_{AB} = 22.5$ mag, which represents the largest redshift survey ever performed with ESO telescopes. In this article we describe the survey construction, together with early results based on a first sample of 55 000 galaxies.

* The VIPERS Team:
L. Guzzo[1] (P.I.), U. Abbas[2], C. Adami[3], S. Arnouts[3, 4], J. Bel[5], M. Bolzonella[6], D. Bottini[7], E. Branchini[8], A. Burden[9], A. Cappi[6, 10], J. Coupon[11], O. Cucciati[6], I. Davidzon[12, 6], S. de la Torre[13], G. De Lucia[14], C. Di Porto[6], P. Franzetti[7], A. Fritz[7], M. Fumana[7], B. Garilli[7], B. R. Granett[1], L. Guennou[3], O. Ilbert[3], A. Iovino[1], J. Krywult[15], V. Le Brun[3], O. Le Fevre[3], D. Maccagni[7], K. Malek[16], A. Marchetti[17, 1], C. Marinoni[5], F. Marulli[12], H. J. McCracken[18], Y. Mellier[18], L. Moscardini[12], R. C. Nichol[9], L. Paioro[7], J. A. Peacock[13], W. J. Percival[9], S. Phleps[19], M. Polletta[7], A. Pollo[20, 21], H. Schlagenhaufer[19], M. Scodeggio[7], A. Solarz[16], L. Tasca[3], R. Tojeiro[9], D. Vergani[22], M. Wolk[18], G. Zamorani[6], A. Zanichelli[23]

[1] INAF–Osservatorio di Brera, Milano, Italy; [2] INAF–Osservatorio di Torino, Italy; [3] LAM, Marseille, France; [4] Canada-France-Hawaii Telescope, Hawaii, USA; [5] CPT Universite de Provence, Marseille, France; [6] INAF–Osservatorio di Bologna, Italy; [7] INAF–IASF Milano, Italy; [8] Universitá Roma 3, Rome, Italy; [9] ICG, University of Portsmuth, United Kingdom; [10] Université de Nice, Obs. de la Cote d'Azur, Nice, France; [11] Inst. of Astron. and Astrophys., Academia Sinica, Taipei, Taiwan; [12] Dip. di Fisica e Astronomia, Universitá di Bologna, Italy; [13] Institute for Astronomy, University of Edinburgh, United Kingdom; [14] INAF–Osservatorio di Trieste, Italy; [15] Jan Kochanowski University, Kielce, Poland; [16] Dept. of Particle and Astrophys. Science, Nagoya Univ., Japan; [17] Universitá degli Studi di Milano, Italy; [18] IAP, Paris, France; [19] MPE, Garching, Germany; [20] Astronomical Observ., Jagiellonian University, Cracow, Poland; [21] National Centre for Nuclear Research, Warsaw, Poland; [22] INAF–IASF Bologna, Italy; [23] INAF–IRA Bologna, Italy

There is no doubt that one of the major achievements of observational cosmology in the 20th century has been the detailed reconstruction of the large-scale structure of the Universe around us. Starting in the 1970s these studies developed into what nowadays is the industry of redshift surveys, beautifully exemplified by the ever-growing Sloan Digital Sky Survey project (SDSS, e.g., Eisenstein et al., 2011).

Maps of the large-scale galaxy distribution have shown not only that the topology of large-scale structure is quite different from how it was imagined at the time of Edwin Hubble and Fritz Zwicky, but have also been crucial to quantitatively supporting the current, successful model of cosmology. The inhomogeneity that we can measure in the galaxy distribution on different scales is one of the most important relics of the initial conditions that shaped our Universe. The observed shape of the power spectrum $P(k)$ of density fluctuations (or its Fourier transform, the correlation function $\xi(r)$), indicates that we live in a Universe in which only ~ 25% of the mass–energy density is provided by (mostly dark) matter. Combined with other observations, it also implies that a ubiquitous repulsive "dark energy" is required to provide the remaining ~ 75% and make sense of the overall picture.

The peculiar motions of galaxies, which reflect the overall growth of structure driven by gravitational instability, also produce measurable effects on these clustering measurements. They provide a way to check whether the "dark energy" hypothesis is really correct, or rather that the observed acceleration is indicating a more radical possibility, i.e., that the theory of general relativity (GR), describing the force of gravity, needs to be revised on large scales.

Galaxy velocities affect the measured redshifts and produce what are known as redshift space distortions (RSD) in the maps of large-scale structure (Kaiser, 1987; Peacock et al., 2001) and, in turn, in the measured galaxy correlations. The observed anisotropy is proportional to the growth rate of cosmic structure $f(z)$, which is a trademark of the gravity theory: if GR holds, we expect to measure a growth rate $f(z) = [\Omega_m(z)]^{0.55}$ (Peebles, 1980). RSD are now recognised as one of the primary ways to make this test (Guzzo et al., 2008). Directly probing the amplitude and anisotropy of clustering, redshift surveys promise to play a major role also in 21st-century cosmology, at least as important as they did in the past one, as several planned experiments, including the forthcoming ESA Euclid mission (Laureijs et al., 2011), testify.

However, the yield of a redshift survey is much more than this. By building statistically complete samples of galaxies with measured luminosity, spectral properties and often colours and stellar masses, they are a key probe of galaxy formation and evolution and of the relationship between the baryonic component that we observe and the hosting dark-matter halos. A survey like the SDSS, for example, based on one million redshifts, was able to measure to exquisite precision global galaxy population trends involving properties such as luminosities, stellar masses, colours and structural parameters (e.g., Kauffmann et al., 2003).

In more recent years, deeper redshift surveys over areas of 1–2 square degrees have focused on exploring how this detailed picture emerged from the distant past. Most of these efforts saw the VLT and the VIMOS spectrograph play a central role, specifically in the case of the VVDS (VIMOS–VLT Deep Survey; Le Fevre et al., 2005) and zCOSMOS (Lilly et al., 2009) surveys. The main goal of these projects was to trace galaxy evolution back to its earliest phases and/or understand its relationship with environment. Only the Wide extension of the VVDS (Garilli et al., 2008), encompassed sufficient volume to attempt cosmologically meaningful computations (Guzzo et al., 2008), but with large error bars. At the end of the past decade it therefore became clear to us that a new step in deep redshift surveys was needed, in the direction of building a sample at $z \sim 1$ with volume and statistics comparable to those of the available surveys of the local Universe.

VIPERS

VIPERS was conceived to fill this gap by exploiting the unique capabilities of VIMOS. Started in Period 82, the survey aimed to measure redshifts for ~ 10^5 galaxies at $0.5 < z < 1.2$, covering an unprecedented volume. Its goals are to accurately and robustly measure galaxy clustering, the growth of structure and galaxy properties at an epoch when the Universe was about half its current age. The galaxy target sample is based on the excellent five-band photometric data of the Canada–France–Hawaii Telescope Legacy Survey Wide catalogue (CFHTLS–Wide[1]).

To achieve its goals, VIPERS covers ~ 24 square degrees with a mosaic of 288 VIMOS pointings, split over two areas in the W1 and W4 CFHTLS fields (192 and 96 pointings respectively). With a total exposure time of 45 minutes per VIMOS pointing, VIPERS will use a total of 372 hours of multi-object spectrograph (MOS) observations, plus 68.5 hours of pre-imaging. Its area and depth correspond to a volume of 5×10^7 h^{-3} Mpc^3, similar to that of the 2dF Galaxy Redshift Survey at $z \sim 0$ (Colless et al., 2001). Such a combination of sampling and volume is unique among redshift surveys at $z > 0.5$. The target sample includes all galaxies with $i_{AB} < 22.5$ mag, limited to $z > 0.5$ through a robust *ugri* colour preselection. The use of an aggressive short-slit strategy (Scodeggio et al., 2009), allows the survey to achieve a sampling rate > 40%. The VIMOS low-resolution red grism (spectral resolution $R = 210$), yields a spectral coverage between 5500 and 9500 Å, for a typical redshift root mean square (rms) error of $\sigma_z = 0.00047$ $(1 + z)$ (directly estimated from double measurements of 1215 galaxies). These and more details on the survey construction and the properties of the sample can be found in Guzzo et al. (2013).

Survey and data management

Handling a spectroscopic survey of this size requires the automation of most of the typical operations and that human intervention is reduced to the minimum necessary. Building on the experience accumulated with previous surveys using

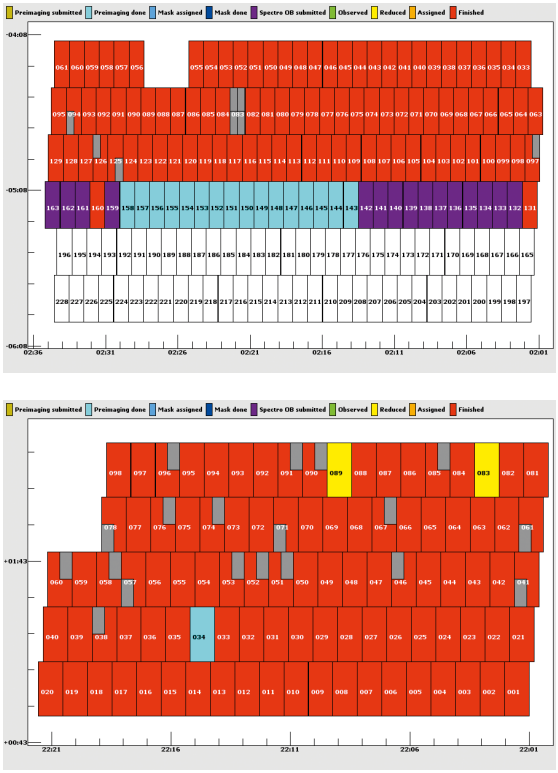

Figure 1. Snapshots from the VIPERS project monitoring web page, giving the detailed status of each VIMOS pointing that is part of the survey. The two images shown here refer to the PDR-1 catalogue discussed in the text, which contains data observed up to January 2012. These correspond to the areas depicted in red. Other colours mark different phases of the data acquisition/processing. The large number of grey rectangles in W4 (bottom) represents VIMOS quadrants for which the mask insertion failed. As can be seen, field W4 is nearly complete.

VIMOS, a fully automated pipeline to process the observations from the raw frames to the final redshift measurement was set up at INAF–IASF in Milan. In this scheme, human work is limited only to the final verification and validation of the measurements, which is still necessary to recover about 20% of the correct redshifts for the lowest quality data.

Most importantly, the whole management and book-keeping of the survey process was also organised within a web-based environment, named EasyLife (Garilli et al., 2012). This is a key feature of VIPERS, which allows us to control in real time any past, present and future events concerning each of the 288 VIMOS pointings that compose the VIPERS mosaic, such as pre-imaging, mask preparation, real-time atmospheric conditions during the MOS observations, quality of the spectra, names of the redshift reviewers, etc. This is achieved through a point-and-click graphical interface, whose appearance is shown in Figure 1. The two panels give the real-time status of each VIMOS pointing in the two W1 and W4 VIPERS fields.

Similarly, the complete work output of the team, from data validation to the science analyses, the distribution of results and draft papers, can be monitored and coordinated through related web pages. Finally, validated redshifts and spectra are fed into an SQL-based database at the completion of the validation phase, such that the real-time survey catalogue (visible only to the data handling group) is constantly and automatically updated to the very last redshift measured. Internal releases can then be made by simply creating a snapshot of the catalogue at a given moment, assuring full version control on the catalogues used for science investigations (internally or publicly) at any stage of the project. A dedicated Wiki-page system provides the team with the appropriate environment for science discussions and to share results. Public web pages are also available, to provide updates about the general project progress[2].

The VIPERS PDR-1 catalogue

After processing, reduction and validation, the data observed up until January 2012 yielded a catalogue of 55 358 redshifts, representing about 60% of the final expected sample. This catalogue, corresponding to the red areas in

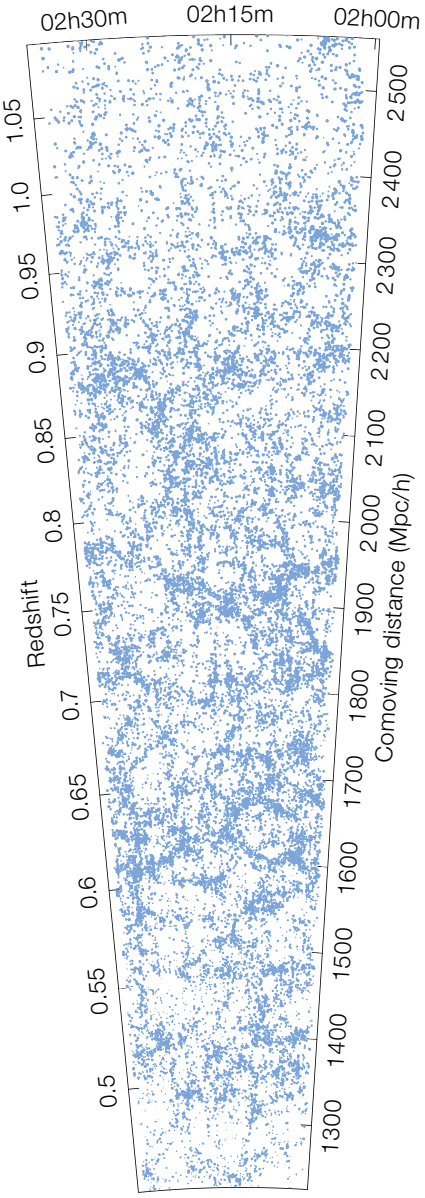

Figure 2. The stunning view of the large-scale structure of the Universe at $0.45 < z < 1.1$, provided by the distribution of ~ 25 000 galaxies in the VIPERS W1 field (Guzzo et al., 2013). The opening angle corresponds to right ascension and the data are projected over ~ 1 degree in declination. The size of each dot is proportional to the galaxy *B*-band luminosity.

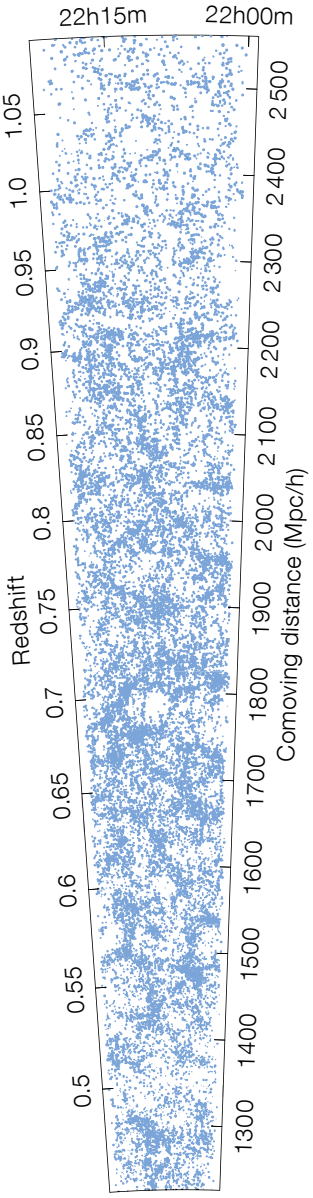

Figure 3. Same as Figure 1, but for the W4 area. The declination projection here is ~ 1.6 degrees.

Figure 1, has been frozen and is now called the Public Data Release 1 (PDR-1) catalogue. All data and analyses presented in the journal papers recently submitted for publication are based on this catalogue, which will become fully public in September 2013. Here we present a selection of these recent results.

Unveiling the structure of the younger Universe

The first immediate outcome of VIPERS is shown by the maps of the galaxy distribution in Figures 2 and 3. The two cone diagrams present a remarkable combination of volume and dynamical range (in terms of scales sampled), which is a unique achievement of VIPERS at these redshifts. They allow us to appreciate both the details and the grand picture of large-scale structure, when the Universe was only between five and eight billion years old.

The following step is to quantify the observed structure as a function of scale. One of the main goals of VIPERS is the measurement of the amplitude and anisotropy of the galaxy two-point correlation function: a first estimate from the PDR-1 sample is shown in the two panels of Figure 4. Crucial for these measurements is an accurate knowledge of several ancillary pieces of information from the survey, such as the photometric and spectroscopic angular selection masks, the target sampling rate and the spectroscopic success rate. These allow us to assign a weight to every observed galaxy in the survey to correct for the overall incompleteness introduced by the different factors.

The fingerprint of RSD is evident in the flattening of $\xi(r_p,p)$ along the line-of-sight direction (left panel of Figure 4). This anisotropy yields a first estimate of the mean growth rate of structure, which is presented in de la Torre et al. (2013). The measured value is in agreement with the predictions of general relativity within the current uncertainty of ~ 17 %. Comparison of the projected correlation functions $w_p(r_p)$ (right panel, Figure 4) shows how well the measurements from the two independent fields agree, in both shape and amplitude. The final VIPERS catalogue will allow us to extend such measurements over two or more redshift bins. Statistical errors will also be reduced by measuring RSD with two independent galaxy populations (McDonald & Seljak, 2009), an important specific advantage allowed by the high sampling of VIPERS.

Figure 5 shows another way of using the VIPERS data and quantifying galaxy clustering. The panels show different estimates of the power spectrum $P(k)$ obtained from the de-projection of the angular clustering measured over the full photometric parent sample of VIPERS i.e. the ~ 140 square degrees of the CFHTLS (Granett et al., 2012). This has been made possible by knowledge of the galaxy redshift distribution provided by an earlier version of the VIPERS catalogue. This measurement of $P(k)$ has been used to obtain improved constraints on the number of neutrino species and

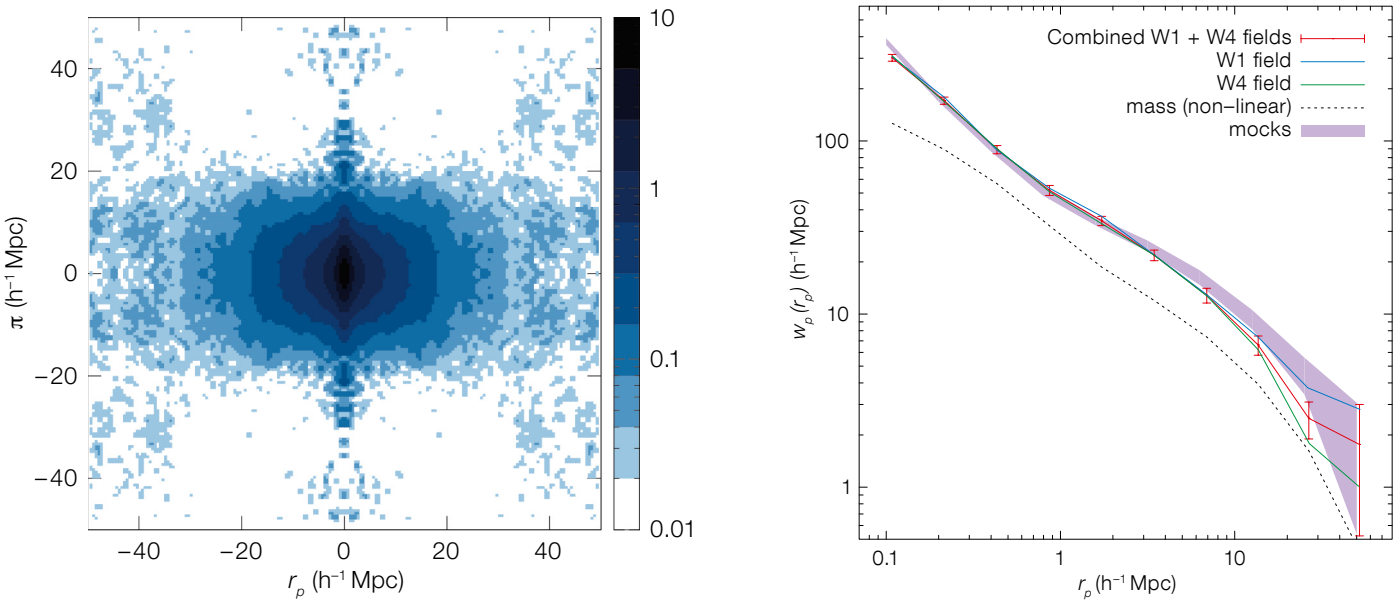

Figure 4. The redshift-space two-point correlation function over the full $0.5 < z < 1.0$ range, from the VIPERS PDR-1 catalogue. Left: The 2D correlation function $\xi(r_p,p)$, showing the well-defined signature of linear redshift distortions, i.e. the oval shape of the contours (de la Torre et al., 2013). Right: The projected correlation function (obtained by integrating the data in the first quadrant of the upper figure along the π direction), for W1 and W4 fields separately and for the total sample. These are compared to the best-fitting Λ Cold Dark Matter model for the mass (dotted line, prediction using the HALOFIT code). The shaded area corresponds to the 1σ error corridor, computed from the scatter in the measurements of a large set of mock surveys, custom built for VIPERS.

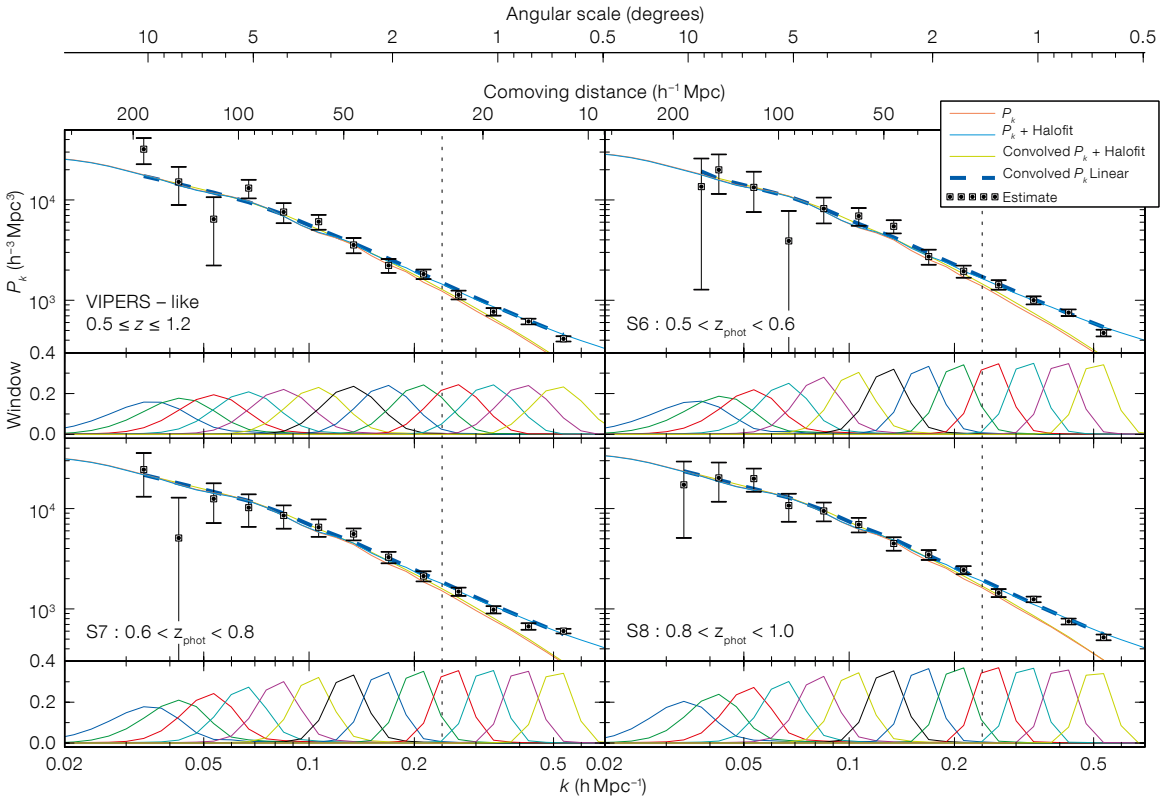

Figure 5. Early estimates of the real-space galaxy power spectrum $P(k)$,through a combination of the photometric data from the full CFHTLS area (140 square degrees) and the redshift distribution *dN/dz* from VIPERS (Granett et al., 2012). The window function of each band is shown in the panel below each plot. The angular power spectrum is estimated from a VIPERS-like colour-selected sample (upper-left panel), and different slices in photometric redshifts are shown in the other three panels. The angular power spectrum is then de-projected to obtain the spatial power spectrum, knowing the *dN/dz* and selection function from VIPERS.

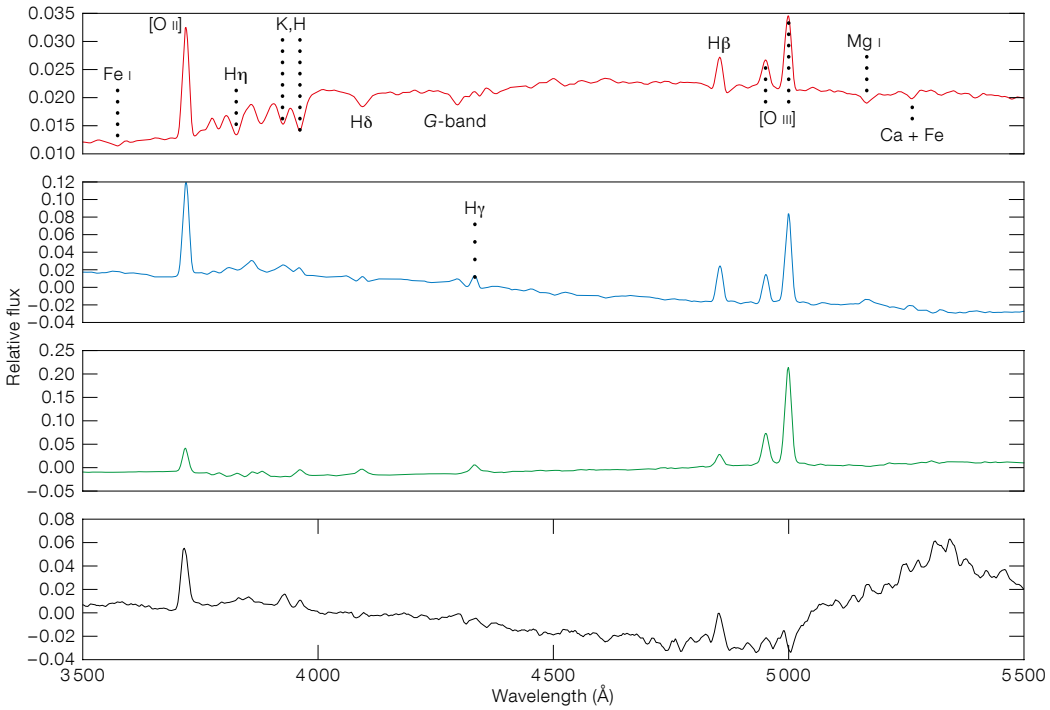

Figure 6. Plot of the first four eigenspectra obtained from the principal component analysis of about 11 000 VIPERS spectra (Marchetti et al., 2013). Each spectrum can be classified in terms of the amplitude of each of its principal components, when it is decomposed into a linear combination of these. This technique allows us to build a spectral classification scheme that is complementary to the SED-fitting technique. In contrast, specific spectra (such as those of active galactic nuclei) can also be spotted among normal galaxies as not being well reproduced by the simple combination of the principal eigenvectors.

their total mass (Xia et al., 2012). A direct measurement of the 3D distribution of $P(k)$ from the VIPERS redshift data alone is under development.

Pinpointing the properties of the galaxy population seven billion years ago

Figure 6 refers to another recently published result, i.e., the decomposition of the first ~ 11 000 VIPERS spectra based on principal component analysis (PCA; Marchetti et al., 2013). The main goal here has been to develop an objective classification of galaxy spectra, capable of separating different populations in a robust way. This will have applications for studies in both galaxy evolution and cosmology (e.g., to define complementary large-scale structure tracers). The application of PCA to the whole PDR-1 sample is ongoing.

As in the case of other deep surveys, an important feature of VIPERS is the complementary photometric information over a wide wavelength range. For VIPERS, the five high-quality bands of the CFHTLS have been further enriched with ultraviolet (UV; Galex) and near-infrared K-band (WIRCAM) photometric observations. These measurements are combined to obtain, for all VIPERS galaxies, reliable spectral energy distribution (SED) fits and, in turn, luminosities and stellar masses. Figure 7 graphically shows the unique power of combining large-scale (positions) and small-scale (here galaxy colour) information: the fact that the colour–density relation of galaxies is already in place at these redshifts is obvious from this figure. Such a wealth of information can be quantitatively encapsulated by statistical measurements of the global population, to reveal overall evolutionary trends. One such statistic is the galaxy stellar mass function; in Figure 8 we show our estimate of this from the VIPERS PDR-1 catalogue and Davidzon et al. (2013) provide more plots and details. Given the volume of VIPERS, Figure 8 presents, without doubt, the most precise estimate ever of the bright end of the mass function at $z \sim 1$ (Davidzon et al., 2013), establishing a new reference for the mean density of massive galaxies at $0.5 < z < 1.2$.

Further results and future perspectives

There are several other important results being obtained from the current VIPERS data. These include an estimate of the matter density parameter Ω_m at $z \sim 0.8$ (Bel et al., 2013), the luminosity dependence of clustering (Marulli et al., 2013) and the non-linearity of the galaxy biasing function (Di Porto et al., 2013), the evolution of the colour–magnitude relation and luminosity function of galaxies (Fritz et al., 2013) and an automatic classification of stars, galaxies and active galactic nuclei (AGN) based on Support Vector Machines (SVM; Malek et al., 2013).

The PDR-1 catalogue includes only ~ 60 % of the final expected data. During the summer and autumn of 2012, 31 additional pointings were observed, covering another full row in W1 (the purple and cyan fields in the upper panel of Figure 1). These data are being processed and, based on the usual yield, are expected to deliver around 11 000 new redshifts. With the current pace, we expect spectroscopic observations at Paranal to be completed by 2014.

We can foresee a number of exciting results being obtained from the VIPERS data in the coming years, with many that will originate from the general community, once the PDR-1 sample is in the public domain in September 2013. The grand view of large-scale structure in the young

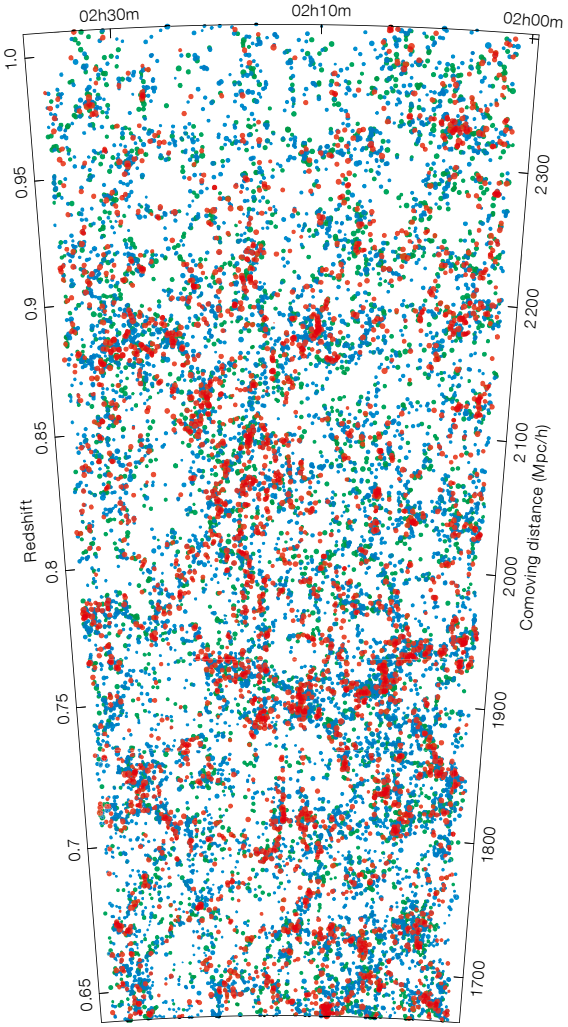

Figure 7. A zoom into the fine structure of the W1 field galaxy distribution, with an additional dimension provided by galaxy restframe colours. This picture gives an idea of the power of coupling multiband photometry to galaxy positions, when scales well above 100 h^{-1} Mpc are mapped. In this example, galaxies have been marked in red, green or blue, depending on their *U–B* restframe colour. In addition, the size of each dot is proportional to the *B*-band luminosity of the corresponding galaxy. The result shows, in all its glory, the colour–density relation for galaxies, already in place at these redshifts, with red early-type galaxies tracing the backbone of structure and blue/green star-forming objects filling the more peripheral lower-density regions.

Universe provided by the first data we have discussed here, makes us hope that — as has happened with previous redshift surveys — the most exciting results will be those that were not even mentioned in the original proposal, but are there awaiting us, written inside the large-scale distribution of galaxies.

Acknowledgements

We acknowledge the continuous support of the ESO staff for all operations in Garching and at Paranal. We especially thank our project support astronomer, Michael Hilker, for his enthusiastic contribution to all phases of the observation preparation and realisation chain.

References

Bel, J. & VIPERS Team, 2013, A&A, submitted
de la Torre, S. & VIPERS Team, 2013, A&A, submitted
Colless, M. et al. 2001, MNRAS, 328, 1039
Davidzon, I. & VIPERS Team, 2013, A&A, submitted
Di Porto, C. & VIPERS Team, 2013, A&A, submitted
Eisenstein, D. et al. 2011, AJ, 142, 72
Fritz, A. & VIPERS Team, 2013, A&A, submitted
Garilli, B. et al. 2008, A&A, 486, 683
Garilli, B. et al. 2012, PASP, 124, 1232
Granett, B. J & VIPERS Team, 2012, MNRAS, 421, 251
Guzzo, L. et al. 2008, Nature, 451, 541
Guzzo, L. & VIPERS Team, 2013, A&A, submitted
Kaiser, N. 1987, MNRAS, 227, 1
Kauffmann, G. et al. 2003, MNRAS, 341, 54
Ilbert, O. et al. 2010, ApJ, 709, 644
Laureijs, R. et al. 2011, arXiv 1110.3193
Le Fevre, O. et al. 2005, A&A, 439, 845
Lilly, S. J. et al. 2009, ApJS, 184, 218
Malek, K. & VIPERS Team, 2013, A&A, submitted
Marchetti, A. & VIPERS Team, 2013, MNRAS, 426, 1424
Marulli, F. & VIPERS Team, 2013, A&A, submitted
McDonald, P. & Seljak, U. 2009, JCAP, 10, 007
Peacock, J. A. et al. 2001, Nature, 410, 169
Peebles, P. J. E. 1980, *The Large-Scale Structure of the Universe*, (Princeton: Princeton University Press)
Pozzetti, L. et al. 2007, A&A, 474, 443
Pozzetti, L. et al. 2010, A&A, 523, 10
Scodeggio, M. et al. 2009, The Messenger, 135, 13
Xia, J.-Q. et al. 2012, JCAP, 06, 010

Links

[1] CFHTLS: http://www.cfht.hawaii.edu/Science/CFHLS/
[2] VIPERS public web pages: http://vipers.inaf.it

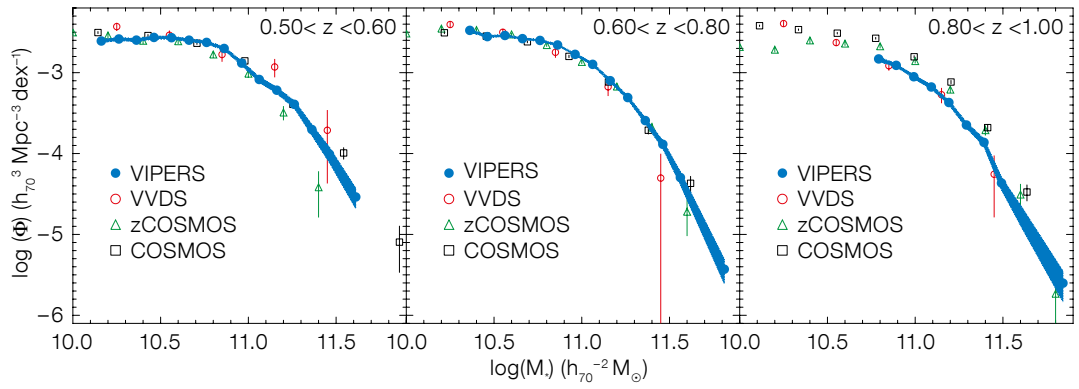

Figure 8. The VIPERS galaxy stellar mass function (MF) at three reference redshifts, estimated from the PDR-1 catalogue (blue points with error corridor, Davidzon et al., 2013). Comparison is provided with previous estimates from two spectroscopic VLT surveys (Pozzetti et al., 2007; 2010) and from the COSMOS photo-*z* sample (Ilbert et al., 2010). Note the small size of the error corridor, indicating how, at large masses, VIPERS is providing a remarkably precise measurement for these redshifts, owing to its large volume.

Progress of the construction of the ESO Headquarters extension is apparent in this image from early March 2013.

The President of the European Commission, José Manuel Barroso, visited Paranal in January 2013 and is shown accompanied by the ESO Director General, Tim de Zeeuw (left). See Release eso1305.

European Commission/ESO

The Federal President of the Republic of Austria, Dr Heinz Fischer, and his wife Margit Fischer visited ESO Santiago offices in December 2012 and are pictured with ESO's Representative in Chile, Massimo Tarenghi (right). See Announcement ann12097.

Report on the Workshop

Ecology of Blue Straggler Stars

held at ESO Vitacura, Santiago, Chile, 5–9 November 2012

Henri Boffin[1]
Giovanni Carraro[1]
Giacomo Beccari[1]

[1] ESO

The last workshop dedicated to blue straggler stars (BSS) took place 20 years ago and there have been a great number of subsequent developments since in both observations and theory. The wide range of BSS topics covered at the workshop are briefly summarised; the published proceedings will form the first book on the subject.

The existence of blue straggler stars (BSS), which appear younger, hotter, and more massive than their siblings, is at odds with a simple picture of stellar evolution, as such stars should have exhausted their nuclear fuel and evolved long ago to become cooling white dwarfs. With the many advances in observational and theoretical work on blue straggler stars, the time was considered ripe for a dedicated workshop to summarise the current state of the field, identify the many still open questions and define in a coordinated way new avenues of research to address these issues. The resulting workshop brought together specialists in binaries and multiple star systems, stellar evolution and stellar populations, as well as the dynamics of clusters. The chosen format of the event (i.e., a low number of participants and a large amount of time devoted to discussion) resulted in a very lively workshop, which was much appreciated by the participants. The discussions were triggered by the very detailed and useful invited talks — no less than 12 were given — providing a unique and insightful view on the field.

The introductory talk by R. Cannon reminded us of the first discovery of blue straggler stars in 1953 by Alan Sandage in the globular cluster M53, as well as the fact that the only previous proper workshop on BSS took place in October 1992, at the Space Telescope Institute, i.e. 20 years ago! It was also Cannon who recalled that the germ of the idea that BSS are due to binaries was planted by none other than Fred Hoyle, only two years after their discovery, as well as by John Crawford in the same year, and then further developed by William McCrea in 1964.

Observations of BSS

As is typical for astronomical conferences, the first few days were dedicated to a review of the observational evidence, clearly demonstrating that BSS are ubiquitous: they exist in globular clusters (talk by F. Ferraro), in open clusters (talks by R. Mathieu and J. Ahumada) and in nearby dwarf galaxies (Y. Momany). Field blue stragglers have also been identified from their anomalous kinematics and chemical abundances (G. Preston). These reviews revealed the fantastic advances made in the field in the past decades.

Ferraro and his group discussed the challenges associated with observing these relatively faint stars in overcrowded stellar regions, such as the cores of globular clusters, and the key advances obtained through high-resolution ultraviolet (UV) photometry. The speakers provided detailed evidence that BSS are a common population found in each globular cluster properly observed, with some clusters (e.g., M80) having more than 100 identified BSS. The observations of many clusters allow a comparative analysis of BSS in globular clusters with different physical parameters to be made, showing the clear connection that is emerging between BSS properties and the parent cluster dynamical evolution. Indeed, the shape of the BSS radial distribution provides a record of the degree of dynamical evolution experienced to date by the parent cluster, indicating how efficient dynamical friction has been, while the presence of double BSS sequences in

Figure 1. The conference photograph in the grounds of ESO Vitacura.

the colour–magnitude diagram could testify to, and even date, the occurrence of the cluster core collapse event. Ferraro's group also presented exhaustive chemical and kinematical analysis of BSS in globular clusters.

R. Mathieu presented a fine study of the BSS population in the open cluster NGC 188, allowing him and his colleagues to perform "micro-astronomics", i.e., determination of the binary frequency and study of the distributions of the orbital parameters (period, eccentricity and secondary mass). G. Preston did the same for the BSS in the field, and the conclusion of both these studies is that BSS present a high binary fraction, with orbital periods of 1000 days, low orbital eccentricities and typical secondary masses of 0.5 $M_{\odot}$. Whether this is similar to the population of BSS in globular clusters is still unknown, but such properties are, as explained by H. Boffin, very reminiscent of the population of barium and other peculiar red giant stars, and thus possibly the result of wind mass transfer from an asymptotic giant branch (AGB) star. The fact that most field BSS are s-process enriched — the exact signature of barium stars — is thus perhaps no surprise, even though much more work is required to connect the two categories of stars.

Interpreting BSS

Following the observational talks, the next days were devoted to the theory and the interpretation of the data. As mentioned, Boffin reviewed the scenario of mass transfer by winds, while N. Ivanova covered Roche lobe overflow. If the latter mass transfer scenario is most likely to occur in the very short period systems (with orbital period of a few days or less), the crucial question is to know under which conditions mass transfer from an AGB star could be stable, so as to avoid the common-envelope (CE) phase. Formation of a CE is thought to cause a dramatic shrinkage of the orbit and thus would not allow the long orbital periods observed in open clusters to be explained. The recent results from Ivanova's group seem to indicate that mass transfer from a giant star may be much more stable than previously thought, leaving a much wider parameter range to explain the existence of BSS. However, it is not certain that this mass transfer happens early enough that plenty of mass is still available to be transferred, a pre-requisite for a BSS.

H. Perets, M. Davies and A. Geller presented the possible formation channels for BSS in various environments, S. McMillan reviewed the dynamical evolution of globular clusters and how BSS fit into the picture, while C. Knigge and A. Sills showed detailed confrontations between the theory and observations. In some cases, data exist that are precise enough to derive detailed information on the characteristics of some blue straggler systems (namely mass, temperature and luminosity), to enable comparison with evolutionary tracks and mass transfer modelling. There were indeed a few surprises: as several reviewers indicated, it is still unclear how to produce BSS with their observed luminosities, which appear to be much too low for their mass, or how one can even produce BSS with such high masses. Similarly, it was generally assumed that two mechanisms were responsible for blue straggler stars — merger and mass transfer — both of which can operate in the same cluster: the exact preponderance of one mechanism over the other possibly depending on the cluster's property, that is, the blue straggler's ecology. The wealth of observations reviewed during the workshop showed that it is still impossible to conclude whether stellar collisions do occur, and could create some BSS. More work is clearly still required in this area.

The last invited talk, by L. Deng, showed the importance of BSS in stellar population synthesis, and how the presence of BSS can dramatically alter the observables of distant systems — their neglect can lead to large errors in the inferred spectrophotometric properties of galaxies. The last word was given to R. Mathieu who brilliantly summarised the workshop and led the final discussion.

As R. Cannon also reminded us during his introductory talk, the few good reviews about BSS date back to the 1990s and no dedicated book exists on this exciting topic. We have thus decided to remedy this situation and make use of the unique expertise gathered by the workshop to produce the first ever book dedicated to BSS. The book will be published by Springer in its Astronomy and Astrophysics Library Series and will contain major chapters from all the invited speakers, edited by us. We aim at producing a book that will appeal to a large community of researchers and especially to graduate students. The book should appear by the year's end. In the meantime, you can still view the presentations and watch some of the recorded talks on the conference web page[1].

Acknowledgements

It is a pleasure to thank all the participants for contributing so actively to the workshop, and especially the invited speakers for providing very clear and exhaustive reviews of their respective areas. Special thanks go to Bob Mathieu for providing an illuminating and entertaining summary talk, from which we unashamedly borrowed to write the present report. Warm thanks also go to the Local Organising Committee for the smooth organisation of the workshop.

Links

[1] Ecology of BSS workshop pages: http://www.eso.org/sci/meetings/2012/bss2012.html

Report on the Conference

The First Year of ALMA Science

held at Puerto Varas, Chile , 12–15 December 2012

Leonardo Testi[1]
Paola Andreani[1]

[1] ESO

The conference reviewed the scientific results of the first year of ALMA Early Science operations and a summary of the highlights is presented. All areas of ALMA Cycle 0 science were covered, with emphasis on new results for astrochemistry, the Solar System, star and planet formation, the life cycle of stars, nearby galaxies, active galactic nuclei and the high redshift Universe. The priorities and prospects for ALMA Full Science and ALMA upgrades were also discussed.

ALMA Early Science Operations Cycle 0 observations started on 30 September 2011. Before then, in spring and summer 2011, the observatory had started to release science-qualified Science Verification (SV) datasets. The first scientific papers based on ALMA data started to appear in press at the beginning of 2012. Since the Cycle 0 observation season was completed at the beginning of 2013 (see Zwaan et al. p. 20), December 2012 was perfect timing to review the first ALMA science results in a dedicated conference.

The conference was co-organised and co-sponsored by all the ALMA partners, with an important additional contribution from the European Commission FP7 Radionet-3 project. 199 astronomers from all over the world gathered in the beautiful setting of the town of Puerto Varas in southern Chile to discuss ALMA science (see Figure 1). Senior astronomers and many young students and postdocs shared their enthusiasm over the first ALMA results. Thijs de Graauw, Massimo Tarenghi and Pierre Cox, current, previous and future ALMA Directors respectively, addressed the participants, sharing with them their insights and reflections on the initial phases of construction, the excitement of delivering the first science observations and the great expectations for future science results. Two public evenings were also organised as part of the conference events, with

Figure 1. The participants at the First Year of ALMA Science conference held in Puerto Varas, Chile.

Raphael Bachiller (Director of the Observatorio Astronómico Nacional [OAN] in Madrid, ESO Council Member and Chairman of the Radionet-3 Board) and Juan Cortes of the Joint ALMA Observatory (JAO) presenting the ALMA project and its science objectives to the general public.

The promise of ALMA was to revolutionise many scientific areas by providing an unprecedented quantity and quality of high spatial and spectral resolution (sub) millimetre wavelength spectral line data. The ALMA challenge is then to allow observers to perform detailed tests of astrochemical models, star and planet formation, galaxy formation and evolution, and many other investigations. Throughout the conference, the transformational power of ALMA data, even with the limited capabilities available so far during SV and Cycle 0, were emphasised many times. The enormous progress in sensitivity and image fidelity provided by ALMA, even at these early stages, was clearly demonstrated.

The science programme for the conference included eight overview talks introducing the different areas of ALMA science, 43 oral contributions, all presenting results from ALMA data, and approximately 100 posters on observational, theoretical and instrumental topics connected with ALMA. Below we provide a short summary of the main science highlights; the programme is available on the conference web page[1].

Astrochemistry

Astrochemistry was one of the main recurring topics in the conference, across all the science areas. ALMA's sensitivity has transformed the field of astrochemistry from the confines of exotic Galactic sources and a few starburst galaxies to a theme that encompasses all areas of ALMA science. Different chemical evolutionary paths during the formation of protostars were discussed at the conference: the new ALMA data are highlighting not only the distinction between "hot corino" and "warm carbon chain chemistry" protostars, which need to be understood and reconciled in a common framework, but also the chemical complexity of the interplay between dust, ices and different molecular species and isotopologues in the path from clouds to planetary systems.

The chemistry of deuterated and complex organic molecules in protostars and discs

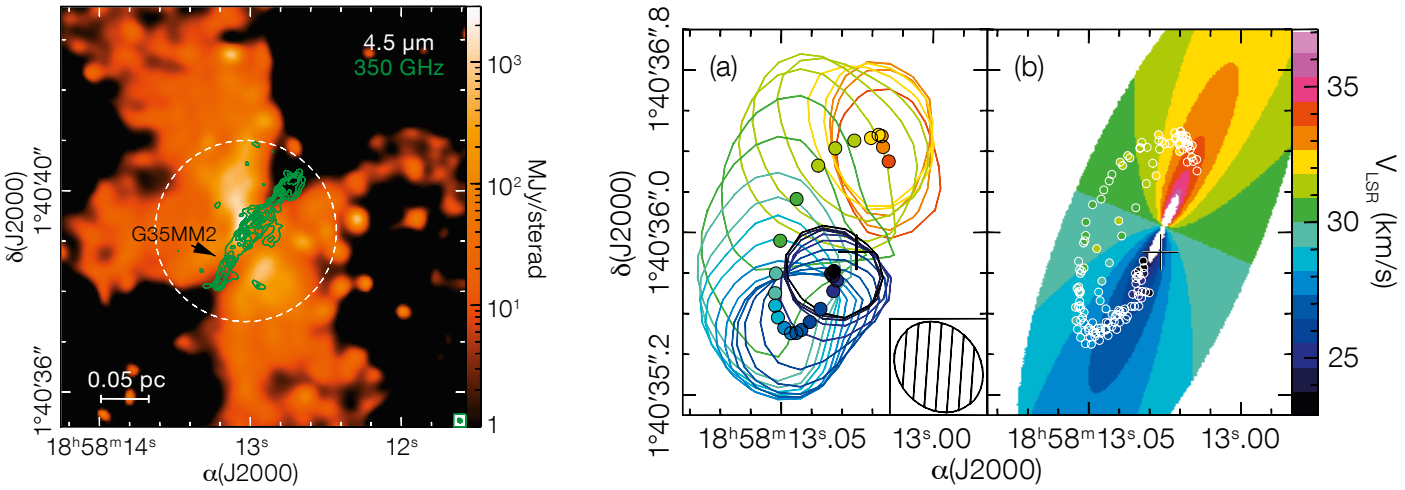

Figure 2. The candidate Keplerian disc around a massive (proto-)stellar system in G35.20-0.74N. In the left panel, the ALMA 350 GHz continuum emission (green contours) is overlaid on the 4.5 μm Spitzer image. The right panels show the kinematical analysis of the disc. To the left is shown the result of the kinematical analysis of the molecular line data towards the hot core (B) in this region with the small filled circles showing the displacement of the photocentre in various velocity channels and the coloured contours showing the full width at half maximum of the emission in each of the velocity channels. To the right is shown the comparison to a disc with a Keplerian velocity pattern. ALMA resolves the emission from several components of the (19-18) transition of methyl cyanide (CH_3CN), as well as transitions of vibrationally excited methanol (CH_3OH) and the HC_3N molecule, both spatially and kinematically, at sub-arcsecond resolution. These complex organic molecules trace the inner few thousand astronomical units of a disc that is well modelled by the Keplerian rotation pattern orbiting a central mass of 18 $M_\odot$. Figure adapted from Sánchez-Monge et al. (2013), in press.

was a major discussion topic, with talks and posters showing the mapping of water isotopes and deuterated species in the planet-forming regions of discs. In a young solar analogue a simple sugar, glycolaldehyde, has been detected (see Release eso1234), which is thought to be an essential step in developing biotic molecules, in particular the RNA molecule. The impact of astrochemistry on extragalactic studies was also highlighted by the Cycle 0 observations of nearby and high-redshift galaxies, which at the ALMA sensitivity are now showing emission from many of the complex and less abundant molecules that have, so far, been mostly studied in our own Galactic environment.

Solar System science

The power of ALMA to study and understand the atmospheres and surfaces of bodies in our own Solar System was reviewed. Some of the main topics where ALMA is expected to make a contribution are in the characterisation of the chemical composition and seasonal variation of the atmospheres of planets and moons, and preliminary ALMA maps of Venus and Titan illustrated this point. A detailed analysis of a combined Herschel–ALMA study of the great storm in Saturn's atmosphere was also presented. The analysis of the data from the two observatories confirms that, while the differing CO intensity inside and outside the storm is just caused by a higher temperature within the storm and not by an abundance variation, the H_2O abundance in the storm is higher than in the rest of the stratosphere of the planet and was probably caused by the vapourisation of icy clouds and enrichment with material from the O-rich troposphere. Much progress is expected to come from the study of the chemical composition of comets, which should provide important constraints on the origin of water and, possibly, complex organic molecules on Earth.

Star formation

Besides the chemical studies, ALMA is now providing new insights on the physical and kinematical structure of protostars and young stellar objects. The first hints that ALMA has started to address directly the long-standing problem of the kinematical signature of disc formation during protostellar collapse was presented at the meeting. Detailed analysis of the CO isotopes in Class 0 protostars reveals a possible break in the kinematics of the collapsing envelope within the central 30–40 AU, an indication of a small inner disc in Keplerian rotation around the central protostar.

The quest for the initial conditions for high-mass star formation has already been brought to a new level with ALMA, where detailed studies of different candidates across the Galaxy provide critical data that can now be directly compared with numerical models. The role of discs and outflows and their structure in the formation of highest-mass stars was also addressed. Tantalising new evidence for Keplerian discs surrounding very massive protostellar candidates provides direct constraints on the formation mechanism (see Figure 2 for an example). The high angular resolution, sensitivity and wide-area interferometric mapping capabilities of ALMA are also proving to be a key tool to understand the formation of very massive clusters, both in our Galaxy and in the Local Universe. The spectacular images of a proto young massive-cluster candidate near the Galactic Centre reveal for the first time a chemical, physical and kinematical complexity that will keep both observers and theorists occupied for several years.

Planet formation

Several new ALMA Cycle 0 results were presented on the structure and evolution of protoplanetary discs and the implications for the formation of planetary systems. Observations of dust evolution in discs around very low-mass stars and brown dwarfs with ALMA cannot easily be explained with the existing dust evolution models, suggesting that our understanding of the processes governing dust evolution in discs is not complete (see Release eso1248). The detection of CO in several of these discs around young brown dwarfs confirms that some of these are indeed surrounded by relatively large and massive discs.

Even in Cycle 0, ALMA has already started to transform the field of planet formation. The sensitivity of ALMA in the high frequency bands, as compared to the previous facilities, has allowed high quality images to be obtained of the asymmetries in the dust distribution and quantitative measurement of the gas content in the inner dust-evacuated holes of evolved discs. The data reveal indirectly the presence of forming planets and constrain the flow of material from the outer disc through the planet and into the inner regions of the system (see Figure 3 and Release eso1301). The dust asymmetries are interpreted as the effect of a planet that induces an asymmetric pressure variation in the outer disc, creating an efficient trap for dust grains. The ALMA sensitivity and angular resolution also allows the direct detection of the CO-emitting layer in the large disc around HD 163296 and to directly constrain the flaring of the disc in molecular gas.

ALMA (ESO/NAOJ/NRAO), S. Casassus et al.

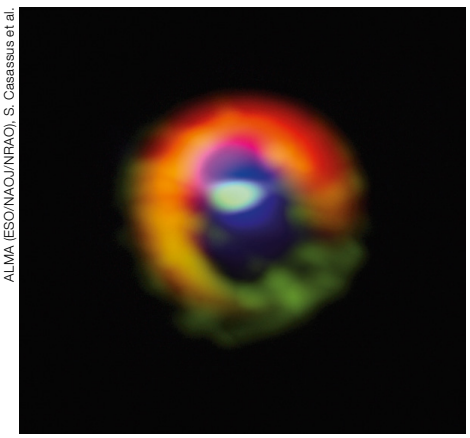

Figure 3. The disc around the young star HD 142527 shown in a montage of HCO^+(4-3) and CO(3-2) emission and dust continuum, highlighting the streams of gas flowing across the gap in the disc. The dust emission in the outer disc is shown in red, dense gas in the streams flowing across the gap, as well as in the outer disc, is shown in green (HCO^+ emission), and diffuse gas in the central gap in blue (CO). The gas filaments can be seen at the three o’clock and ten o’clock positions. From Casassus et al. 2013; see Release eso1301 for more details.

Stellar evolution

ALMA can also provide new constraints, not only on the cool side of the Universe, but also on the hot atmospheres of stars. Multi-wavelength observations at centimetre and millimetre wavelengths of the stellar chromospheres can allow the amount of magnetic heating in stars to be probed. For this reason, its capability to observe the Sun is one of the key features of ALMA, and has been designed into the system from the very beginning of the project. While observations of the Sun are still being tested and commissioned, ALMA has been observing different phases of stellar evolution from the beginning of Cycle 0. Millimetre flares in young stellar objects have been recently observed and will become an important topic for ALMA science owing to the high sensitivity available.

Millimetre continuum observations will also be critical to separate the non-thermal emission from the coronae and the stellar wind components, allowing direct measurements of the mass loss in stars of various masses and ages. Initial results in this area are expected from Cycle 1 programmes. In Cycle 0, several programmes focused on the study of the mass loss in the late stages of evolved stars. Observations of stars in the late stages of stellar evolution provide constraints on the chemical enrichment of the interstellar medium. Some of the most spectacular ALMA data on the late stages of stellar evolution presented at the meeting included: the mass-loss history following the thermal pulse in the asymptotic giant branch star RScl (see ESO release eso1239 and the cover of *The Messenger* 149) and detection of the dust, CO and SiO emission in the ejecta of SN 1987A in the Large Magellanic Cloud.

Galaxy formation

In the nearby Universe there is the potential for ALMA to directly study the sites of star formation, i.e. giant molecular clouds (GMCs), in order to derive the star formation efficiency and the gas depletion time on sub-galactic scales. These can be related to galaxy properties, such as metallicity, cloud densities and pressures, and velocity dispersions. Some nearby galaxies have already been targets of ALMA SV projects. The impressive M100 large-scale mosaic shows that CO emission traces a two-armed spiral and a double bar out to 10 kpc and that the time needed for the current star formation rate to consume the existing gas reservoir is 1.7–1.9 Gyr.

Molecular gas fragmentation has been observed to occur at parsec (pc) scales along filamentary structures in NGC 253, the Antennae Galaxy and 30 Doradus. At galactic scales, the parents of these filamentary structures are GMCs, with masses of ~ 10^{5-6} $M_\odot$ and sizes of tens of pc. These are found in spiral galaxies and in the interarm region of the overlap of the arms of the Antennae. A newly discovered tidal filamentary arm was presented in NGC 4039, 3.4 kpc long and < 200 pc wide, where the star formation efficiency is a factor of ten larger than in disc galaxies.

ALMA’s resolution also enables details of the centres of nearby mergers to be probed. Double nuclei have been detected in NGC 3256, similar to those in Arp 220, while in NGC 34 (a luminous infrared galaxy with an active galactic nucleus [AGN]) Band 9 CO(6–5) observations are consistent with two nuclei: one associated with a starburst and another with the AGN.

Several presentations clearly pointed out the fundamental contribution that ALMA is providing to the field of galaxy formation in addressing the major mechanisms: merger and starburst-driven or governed by secular evolution. An initial attempt to answer some specific questions was carried out by the LESS and COSMOS continuum surveys with the determination of galaxy counts. These surveys also enable better estimation of the spectral energy distribution (SED) of galaxies, and therefore of the dust mass and gas fraction.

Active galactic nuclei

One of the biggest puzzles in active galactic nuclei physics is the removal of the angular momentum from the disc gas and mechanisms driving infall down to the nucleus on scales of tens of parsecs. Simulations suggest a role for galaxy bars, but no correlation between AGN activity and bars is seen. New ALMA results for two sources (NGC 1433 and NGC 1566) show that the dense molecular gas seems to fall into the nucleus at the unprecedented spatial resolution of 24 pc. The kinematics of the nuclear spiral arms in NGC 1097 have been followed down to ~ 50 pc from the central supermassive black hole (SMBH) from the ALMA detection of HCN, a tracer of high density gas.

Absorption lines in the spectra of AGN, the nearby Centaurus-A (Cen-A) and PKS1830-211 at z = 0.886, were also shown. Such investigations offer a unique opportunity to find gas that might be feeding the AGN. Towards the SMBH of Cen-A, the gas becomes denser, warmer and influenced by the presence of photon dissociation regions (PDRs). Detailed study of absorption lines towards AGN reveals the chemical enrichment of the Universe through isotopic ratios and can constrain the constancy of fundamental constants by detecting line shifts with respect to laboratory measurements, such as in PKS1830-211, where ALMA observations include water in absorption.

Molecular outflows may be associated with AGN activity or with vigorous starbursts and have been detected with ALMA in HCO^+(4-3) and CO(3-2) through their high-velocity wings. In the centre of NGC 253, the ALMA detection of the H40α line in a molecular outflow raises the question of the mechanism for efficient transfer of angular momentum to the molecular gas. Several talks pointed out the need to measure outflow rates of cold gas and test star formation and AGN feedback models. A key issue is the investigation of the processes that quench star formation and turn galaxies into “red and dead”. New ALMA results were presented on a sample of extremely rare ultra/hyper-luminous very red radio-loud quasars, which are considered young jet feedback candidates at z = 0.5–3. ALMA is able to put strong constraints on the presence of cool dust and star formation, and to confirm that this sample consists of heavily obscured Type 2 quasars, often Compton-thick and very strongly AGN-dominated; some sources do not show any evidence of star formation.

The environment around galaxies, such as the X-ray cavities in galaxy clusters provides good locations for measuring the mechanical power injected by the SMBH. AGN heating is energetically sufficient to offset radiative cooling in galaxy cluster cores and can be coupled to the cooling gas and therefore to feedback. CO has been detected in the centre of two nearby clusters with extreme X-ray cooling rates; a radiative cooling time < 1 Gyr and a star formation rate of 10–100 $M_\odot$/yr for the central radio galaxy were derived. The bulk of the cold gas is centrally condensed and has a similar spatial extent to the star formation.

Observations of two extremely obscured luminous infrared galaxies (LIRGs) with very large obscuration and hidden compact infrared cores show a rich, hot-core-like chemistry with vibrationally excited HC_3N, HNC and HCN. In NGC 1266, an interacting galaxy, we are witnessing a rapid cessation of star formation, with a dense molecular gas outflow rate of ~ 100 $M_\odot$/yr, much larger than the star formation rate. An AGN is the likely driver of the outflow, and shocked molecular gas is located near the launch point of the outflow, as seen in ALMA multi-transition SiO observations. The detection of other molecular species with ALMA will help build a more complete chemical picture of NGC 1266.

High redshift sources

The redshifts of very high-z (z > 5) galaxies leads to fuller understanding of the objects responsible for the reionisation of the Universe. Their redshifts can be determined through detection of the [C II] line, which is the principal interstellar medium gas coolant, traces PDRs, and warm intergalactic and circumnuclear media, and CO lines (see Figure 4 for an example). [C II] is up to ten times more luminous than any other line in the far infrared/millimetre range, and at z > 5 the line is redshifted into ALMA bands. ALMA can detect [C II] from a galaxy with a star formation rate of only 5 $M_\odot$/yr at z = 7 in 1 hour (5σ in two channels). Furthermore, in low metallicity systems, as high-z objects are expected to be, the ratio [C II]/far-infrared is larger, i.e. increases with decreasing metallicity. Outflows can also be detected in such distant galaxies, as revealed by [C II] emission line profiles in a z = 6.4 quasar with velocities > 1000 km/s, size > 10 kpc and an outflow mass rate of ~ 3000 $M_\odot$/yr. The gas consumption timescale due to outflow may be less than the star formation timescale, highlighting the “quasar-mode” feedback process which inhibits further star formation and enriches the local intergalactic medium.

Gravitational lenses

The flux magnification provided by gravitational lensing enabled a spectroscopic redshift survey with ALMA to be performed in Cycle 0, targeting 26 sources from the South Pole Telescope using CO line detections (see Figure 4). 40% of these sources lie at z > 4. It appears that the fraction of dusty starburst galaxies at high redshift is far higher than previously thought. Two sources were found at z = 5.7, placing them among the highest redshift starbursts known, and demonstrating that large reservoirs of molecular gas and dust can be present in massive galaxies near the end of the epoch of cosmic reionisation. The ALMA detection of the arcs and source images of a beautiful gravitational lens, g15.v2.19, was also shown and discussed.

Prize poster competition

Given the large number of young participating students and postdocs, who presented many excellent results in the poster sessions, the Scientific Organising Committee decided to organise a competition for the best posters amongst them. The poster prize committee, composed of the overview speakers and the project scientists, awarded three prizes for the best science posters to: E. Akiyama for the analysis of the SV data on the protoplanetary disc around the

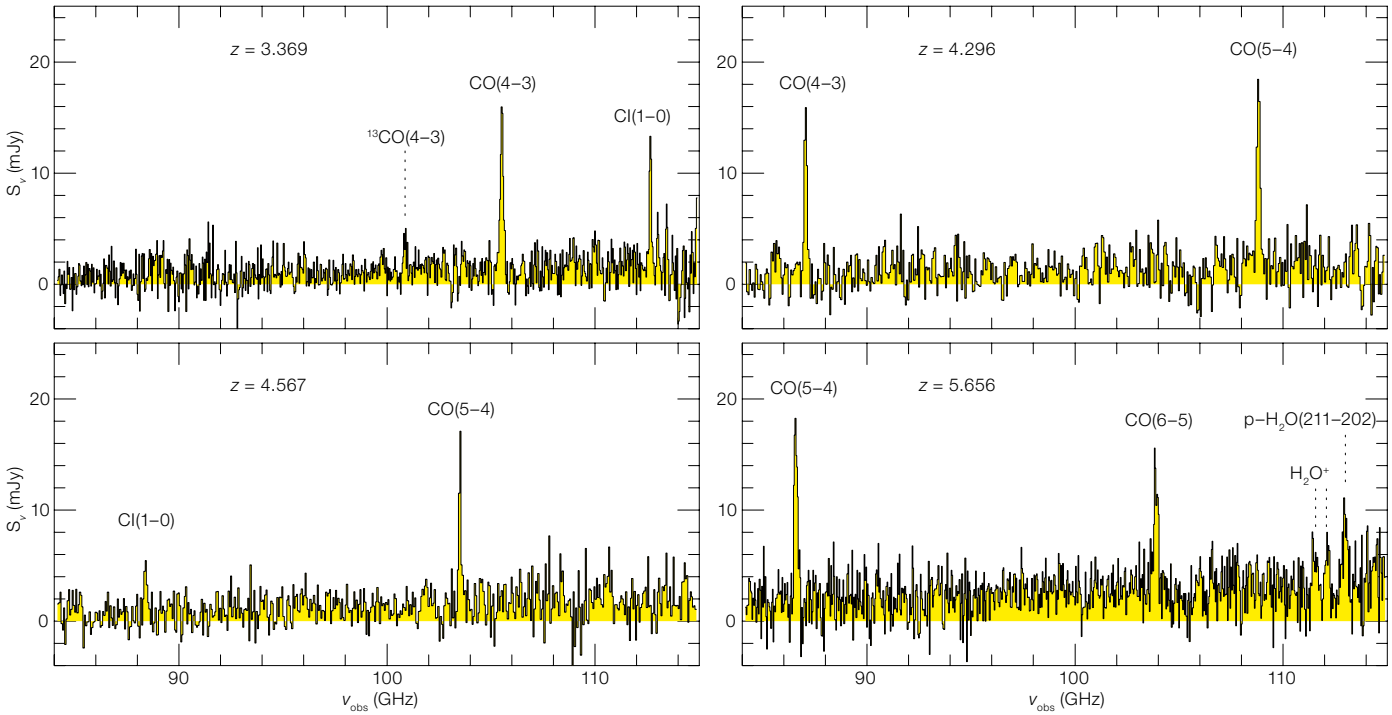

Figure 4. Example ALMA Band 3 spectra of gravitationally lensed submillimetre galaxies selected from the South Pole Telescope survey (Weiss et al., 2013). The spectra demonstrate the sensitivity of ALMA and the richness of the survey with detections of ^{12}CO, ^{13}CO, C I, H_2O and H_2O^+.

intermediate-mass pre-main sequence star HD 163296; R. Herrera-Camus, for the important work on the calibration of the [C II] line as a star formation tracer in the deep Universe; and M. McCoy for the study on the Early Science absorption spectrum of the nearby active galactic nucleus of Cen-A. Each of the three winners received an ALMA coffee mug, as a useful tool for the long hours to be spent on the scientific interpretation of the ALMA data, and a copy of the book *Cerca del cielo*, to remind them of the beauty and biological richness of the region of northern Chile that hosts the ALMA Observatory. Two posters describing important technical developments for ALMA also received a special mention: A. Avison for his work on the Observation Support Tool and H. Nagai for the description of the status of ALMA polarisation observations.

The practical organisation of the meeting was a great success, thanks to the efforts of the local organising committee at the JAO: Mariluz Calderón, Ann Edmunds, Valeria Foncea, Itziar de Gregorio Monsalvo, Violette Impellizeri, Hanifa Nalubowa, and Gautier Mathys (chair). The conference was co-sponsored by ESO, NAOJ, NRAO, the EC-FP7 Radionet-3 project and CONYCIT.

References

Casassus, S. et al. 2013, Nature, 493, 191
Sánchez-Monge, Á. et al. 2013, A&A, in press
Weiss, A. et al. 2013, ApJ, in press

Links

[1] First Year of ALMA Science conference website: http://www.almasc.org/

ESO/B. Tafreshi (twanight.org)

A recent view of the Chajnantor Plateau and ALMA taken from the nearby peak of Cerro Chico. See Picture of the Week 24 December 2012 (potw1252a).

Report on the ESO Workshop

Real Time Control for Adaptive Optics 2012

held at ESO Garching, Germany, 4–5 December 2012

Enrico Fedrigo[1]

[1] ESO

The Real Time Control for Adaptive Optics workshop series was conceived to bring together international specialists in real-time control (RTC) for adaptive optics in order to share and exchange experience regarding the design and implementation of these systems. During two full days, the participants were presented with 28 talks divided into seven sessions, one panel discussion and two free-form open discussions. The major topics covered during this second RTC workshop are briefly reported.

The real-time control system is a crucial component for any astronomical adaptive optics (AO) system. The computational demands placed on the next generation RTCs for future extremely large telescopes (ELTs) are enormous, and even current systems require specialised skills to implement. The workshop series brings together international AO RTC specialists with the aim of sharing and exchanging experience in order to improve the design of new and proposed AO systems, increasing their performance and usability. Although the workshops are focused principally on astronomical AO, attendance of participants from non-astronomical areas, including industry, was welcomed, and indeed encouraged, to allow cross-disciplinary discussions to take place.

Figure 1. The QR code used to announce the website[2] of the RTC Workshop 2012.

Facts and figures

This was the second in a series of Real Time Control for AO workshops; the first was held in Durham in April 2011[1]. Sixty-six outside participants, complemented by a number of ESO staff members, attended the 2012 workshop: the 28 talks were divided into seven sessions and there was one panel and two open discussions (access the workshop programme via the QR code [Figure 1] or directly via the web page[2]). Most of the participants were European (see the breakdown in Figure 2), with about 10% non-European participants (USA, Canada, east Russia), and almost 20% of the participants were from industry, all former or current ESO partners. The workshop also invited participants to a social dinner in true Bavarian style at the Augustiner restaurant in central Munich, surrounded by the warm atmosphere of the Christkindl open-air market.

Technology

The major topics covered in the workshop were technology and algorithms, the former divided into three technological families: Central Processing Units (CPUs), Graphical Processing Units (GPUs) and Field Programmable Gate Arrays (FPGAs). Different groups took different approaches and none was really identified as the “silver bullet”. FPGAs are components that can execute a program at hardware level and are therefore potentially very fast but, above all, extremely deterministic, since every phase of the process is under the control of the programmer. This is the approach taken by one group at the Thirty Meter Telescope (TMT) project [talk by Ljusic] who designed a custom board populated by a large number of FPGA chips. Something similar was made by Microgate [presented by Biasi], with custom boards made with both FPGA and DSPs (Digital Signal Processors), the latter a technology that does not seem to hold any prospects for the future. SPARTA[3] for the VLT also contains FPGAs and DSPs [Suarez], integrated in commercial boards.

While recognising the value of predictability and determinism, important for multi-year development projects, the panel discussion immediately pointed out the main problem with this technology, which is the long round-trip engineering cycle required to develop under FPGAs. This aspect was exacerbated in ESO’s SPARTA project, as all FPGA development is outsourced and therefore any new requirement takes a long time to be completed, mostly due to contractual issues. With respect to this point, some talks [Dipper] identified the Open Computing Language (OpenCL) framework as a promising approach for enhancing FPGA design productivity that would, at the same time, unify the development between FPGAs, GPUs and the advanced mathematical units of the CPUs.

The second family of technology that was considered is the GPU, or rather General Purpose Graphical Processing Unit (GP-GPU), currently being looked at by many groups. When used in real time, this approach suffers from the computing model offered by the GPU cards presently on the market: no on-board input/output is featured and they must receive data from the central processing unit and its memory. Recent developments such as NVIDIA GPUDirect [talks by Gratadour and Dipper] promise to

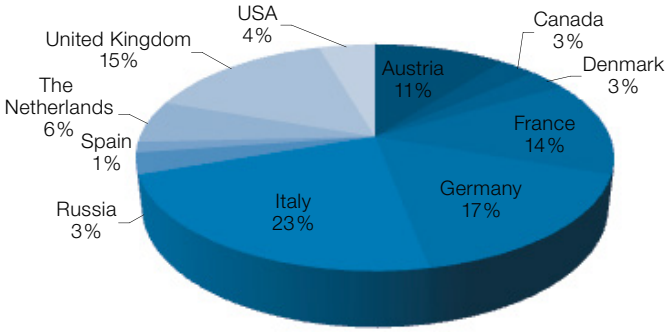

Figure 2. The breakdown of participants to the second Real Time Control for Adaptive Optics workshop.

alleviate some of the problems. Several prototypes and projects were presented by LESIA [Sevin, Gratadour], another group from TMT [Wang] and the Dutch Organization for Applied Scientific Research [TNO; Doelman], the latter projecting a possible GPU-based system for an instrument of the size of the E-ELT Exoplanet Imaging Camera and Spectrograph (EPICS; see Kasper & Beuzit, 2010).

However, even though of a different magnitude, GPUs suffer from a similar problem to the FPGAs: they need specialised tools and specialised knowledge to really harness the computing power available. GPUs are now very common; so many libraries are available to implement standard algorithms, without the need to learn a new technology. Also mentioned in several talks was the upcoming Intel Phi [Dipper, Gratadour], the first instance of the new Intel many-core architecture. It shares several aspects of a GPU since it sits on the same peripheral component interconnect (PCI) bus and acts as an accelerator without dedicated input/output. However inside it is a many-core system, so will be something potentially easier to program with standard tools and languages.

Especially relevant here was the invited talk delivered by a worldwide expert in the field of high performance computing, author of FFTW (Fastest Fourier Transform in the West) and Cilk (a computing language for multi-threaded parallel computing), Matteo Frigo. One of the issues clearly understood and mentioned also in several talks is the need to develop a strategy for managing obsolescence, since the main subject of the workshop is devoted to computer systems that will be operational for the first time in ten years from now and will run for 10 to 20 years. Frigo explained how he designed FFTW and Cilk in a fully portable way regardless of the number of available cores, their cache or interconnections, without penalising performance, hints that can be exploited in developing a CPU-based system, in particular with the Phi.

The last technology family, standard CPUs, was presented by several groups who are pursuing implementations of small or medium-sized AO systems on an all-CPU system, from solar astronomy at the Kiepenheuer Institute (Linux, ~ 500 subapertures; with plans to switch to the higher performance FPGA for the future 1600-subaperture system, [Bekerfeld]), to Force Technology (FreeBSD, with 2500 subapertures, [Kamp]), to the Durham DARC real-time controller (Linux, with ~ 200 subapertures, [Basden]), to the all-CPU version of ESO’s SPARTA running on the Intel version of the real time operating system VxWorks (1300 subapertures, [Tischer]).

The clear advantage of all-CPU systems is the ease of programming and the short development time required to achieve a minimum functionality. This was clearly demonstrated by the Durham system where a number of strategies and algorithms were prototyped and tested [Basden]. What it takes to scale the system up is more debatable: how to tune it to the best performance possible and move the implementation from prototype to production. The major issue with this approach might not be the debate about whether performance can come by tweaking and hacking a freely available operating system or by purchasing an already optimised one together with its optimisation tools, but rather the people factor: any coding effort, including the “hacking” part, requires people to do it and perform long-term maintenance. It is this latter aspect that will play a major role in the decision process more than the technical solution.

The other problem with an all-CPU strategy that the audience identified is the unpredictability of any CPU-based implementation: until code is instantiated on a given platform you will never know how well it runs, making the cycle of design-on-paper-then-implement-on-silicon difficult to manage without proper prototyping. But it is clear that a system based on CPU with its inherent flexibility would be a powerful tool to test new strategies and algorithms as well as powering a laboratory system, where downtime is normally not the first issue to solve.

As a synthesis of all the presented technologies, the SPARTA team proposed a concept [Suarez] that encompasses many of the previous ideas in a flexible architecture originally presented at the SPIE 2010 meeting. The main idea is to maximise the reuse of the SPARTA architecture and software to achieve the highest cost-saving possible, while abandoning the VMEbus in favour of using server-class systems to host accelerators of various types, or even just using the available plain CPU to achieve lower hardware costs and better maintenance capability.

Algorithms

The other major topic of the workshop concerned which algorithm a real-time controller should implement. A typical measure of the complexity of an AO RTC is the product of the number of degrees of freedom at the input (the total number of gradients, or double the number of subapertures), the number of degrees of freedom at the output (the total number of mirror actuators) and the sampling rate. Without going into the details of latency requirements [as discussed by Fedrigo], this measure defines the minimum computing power required, assuming a standard least squares estimate reconstructor, which can be easily implemented as a matrix-vector multiplication (MVM). For certain systems like EPICS this measure can be prohibitively high, so this is where smart algorithms come into play.

Smart algorithms can be divided into two broad categories: ones that use a sparse, or sparsified, interaction matrix without inverting it; and others that use a model of the system, sometimes applying an interaction matrix to tune the model. In the former case the solution is found by using a conjugate gradient descent or a variation of it. In the latter case it depends on which model is used. Several talks in the algorithms session came from the Austrian Adaptive Optics group who are contributing to ESO with in-depth research on novel reconstruction algorithms. Some of their proposed algorithms have already been tested on the laboratory bench and even on sky (as reported at the workshop, [Bitenc]) and seem very promising. The portfolio of proposed algorithms spans a broad range running from a single conjugate AO (SCAO)/extreme AO (XAO) system (the CuRE family of algorithms, [Rosensteiner] and [Shatokhina])

Figure 3. One of the Real Time Control for Adaptive Optics workshop sessions in the auditorium of ESO Headquarters.

to multi-conjugate (MCAO)/laser tomography (LTAO) AO (Kaczmarz and wavelets, [Ramlau] and [Yudytskiy]) with multi-object AO in the works.

Further contributions from Lyon [Bechet] presented an optimisation of the already mature, at least in the simulation world, Frim algorithm, that has versions available for SCAO and MCAO. This algorithm is essentially a pre-conditioned conjugate gradient (PCG) method, with an arrangement that exploits the closed-loop nature of the process and thus reduces the iterations of the PCG to only one, pushing the others outside the latency cycle, a smart arrangement that is rather generic. A contribution from TU-Delft [Verhaegen] uses splines on triangular partitions to reconstruct the wavefront in a highly parallelisable architecture that, in a similar way to the CuReD (a fast wavefront reconstructor), could address the E-ELT planet-finder EPICS directly. Finally a method that only uses the images in the science detector was proposed [Koriakoski], however it is still in an early stage and suffers from several limitations. Overall, an impressive array of methods and algorithms are now available to replace traditional matrix-vector multiplication methods and the next step is to try them out.

Conclusions

Two trends are developing and converging: a push to make the real-time controller hardware faster and computationally more powerful, and a push to reduce the required computational power by means of approximated methods. The feeling of the audience was that the convergence point has already passed, such that smart algorithms can be implemented into relatively small and cheap systems, while traditional MVMs can now reach very large dimensions. It might now be a matter of choice: a relatively cheap system based on an approximated smart algorithm or a more expensive, bigger system based on the well-known and feature-rich MVM. Smart algorithms will certainly be more complex to implement than a plain MVM where extreme optimisations can be obtained; therefore smart algorithms might be best coupled with all-CPU systems or with CPU-based accelerators, while highly optimised MVM-based algorithms can be better served by GPU- or FPGA-based or accelerated systems.

Amongst the major drivers that need careful examination, the workshop identified on the one hand that the future RTC for AO will likely be a heterogeneous computing environment [Dipper, Suarez] and, on the other, that software development costs are going to be the important factor [Dipper]. Therefore the need to share developments across instruments arises. Amongst real systems, SPARTA for the VLT has already achieved that [Suarez], serving 20 AO instruments of various sizes and characteristics. Moreover it features an almost complete supervisor software that accounts for the majority of the coding effort. But other initiatives aim at achieving similar results.

A “killer” feature of the future platforms will be the capability to integrate a quasi real-time AO simulation system, similar to the end-to-end AO simulators used to predict system performance [Gratadour]. This will be desperately needed since the number of ELT-size AO benches and their availability will be extremely limited in the future and therefore the majority of the development and testing of the RTCs for the ELT AO-based instruments will be done without a bench and only with the aid of a simulation tool. Yet another challenge for the community.

Given the success of this second workshop the community agreed to convene again in about 18 months for a third one. Exact date and place will be published both on the workshop mini-site[2] and on the AO RTC collaborative web hub[4]. Meanwhile all of the presentations given at the workshop are available online[2].

Acknowledgements

The workshop was only possible thanks to the dedication of the members of the Scientific Organising Committee (Alastair Basden, Dolores Bello, Corinne Boyer, Enrico Fedrigo [chair], Glenn Herriot, Arnaud Sevin and Marcos Suarez [co-chair]), the Local Organising Committee (Samantha Milligan, Marcos Suarez, Enrico Fedrigo), the ESO IT Helpdesk, in particular the video-conferencing team, and many others, who provided logistical support. We are particularly grateful to Samantha Milligan and her passion for detail, that everything in the organisation ran smoothly, and the very positive spirit of all attendees made all tasks very pleasant. I thank all the organisers and participants.

References

Kasper, M. & Beuzit, J. L. 2010, The Messenger, 140, 24

Links

[1] The 2011 RTC for AO workshop pages: http://www.dur.ac.uk/cfai/ adaptiveoptics/rtc2011/

[2] The 2012 RTC for AO workshop pages: http://www.eso.org/sci/meetings/2012/RTCWorkshop.html

[3] SPARTA platform for AO RTC development for the VLT: http://www.eso.org/sci/facilities/develop/ao/tecno/sparta.html

[4] The AO RTC hub: http://aortc.ast.cam.ac.uk/

Llullaillaco and Paranal's Skyline

Reinhard Hanuschik[1]

[1] ESO

The visibility of the volcano Llullaillaco from Paranal is discussed. That it can be seen at all depends on two circumstances: a fortunate geometry and the superb quality of the atmosphere over the Atacama Desert, stretching over a baseline of 190 kilometres, much longer than in any astronomical observation.

If you have ever happened to visit Paranal you will have very likely recognised a majestic peak on the eastern horizon. This is Llullaillaco (pronounced You-ya-i-yaco, meaning "dirty lagoon" in Ketschua), at 6739 metres above sea level, the third-highest peak in Chile, the seventh highest in the Andes, and arguably the highest active volcano in the world. The view from Paranal is shown in Figure 1. The last eruption of Llullaillaco was recorded in 1877. It has beautiful lava flows extending both to the north and south. During most of the year it appears as snow-capped, although without glaciers: the snow limit in that part of the Andes is the highest in the world, at about 6500 metres. Even in that part of the Andes you would have to travel 265 kilometres to find a higher contour (Tres Cruzes, 6749 metres). It is impressive even by Chilean standards, and dwarfs Europe's highest mountain, Mt. Blanc at 4810 metres.

The first recorded ascent was in 1952[1], but there were earlier visitors: the mummies of three Inca children were discovered close to the summit in 1999, thus making Llullaillaco the highest archaeological site in the world.

Visibility

There are several interesting aspects about Llullaillaco that are related to Paranal itself and its skies. First, as Google Earth confirms, the Paranal–Llullaillaco line of sight (LOS) spans 190 kilometres, starting on the Paranal platform at an elevation of 2600 metres and ending at 6739 metres, right at the

Gianluca Lombardi/ESO

Figure 1. Llullaillaco as seen from the VLT platform. Close-up of a picture taken by Gianluca Lombardi on 19 December 2011.

Chilean–Argentine border. This is almost the entire width of Chile at this latitude.

If you take it for granted that one can spot a 6700-metre peak from a distance of 190 kilometres, then it is interesting to check the LOS profile (Figure 2, dotted blue line) from Paranal (P) towards Llullaillaco (L). There are two "critical" points: the nearby Sierra Vicuña Mackenna (A, 20 kilometres distant from Paranal, and including Cerro Armazones), and the distant Cordillera de Domeyko (B, 125 kilometres). For orientation, the ruta 5 is also marked (red square). It is clear that we have been lucky (or benefit from careful planning) with the siting of the Paranal platform: if it had been blasted just a few tens of metres lower, the view towards the Llullaillaco summit would have been vignetted by the nearby Sierra Vicuña Mackenna, as one can confirm by walking down from the platform along the road to the hairpin bend. The other element of luck is that the LOS crosses the Sierra just south of Cerro Armazones.

Figure 2. The line of sight (in blue), the terrain, and atmospheric layers, neglecting surface curvature between Paranal (P) and Llullaillaco (L) . Intervening places are explained in the text. The terrain has been taken from Google Earth. Distances are in kilometres, elevation in metres.

In addition to the purely fortuitous terrain morphology, there is another important effect to take into account: the curvature of the Earth. With distance D from the reference point P, the deviation of the tangential plane from the (ideal) surface curvature grows as $D^2/(2R)$, where R (6371 kilometres) is the mean Earth radius[2]. Figure 3 shows the LOS with curvature taken into account. Since the

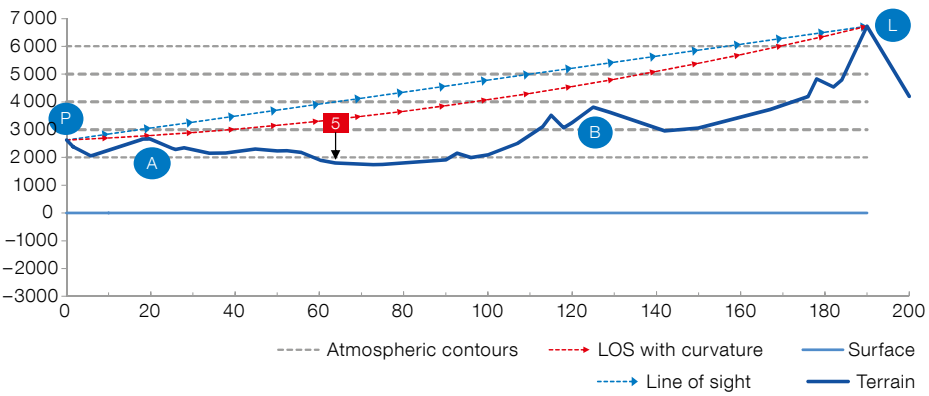

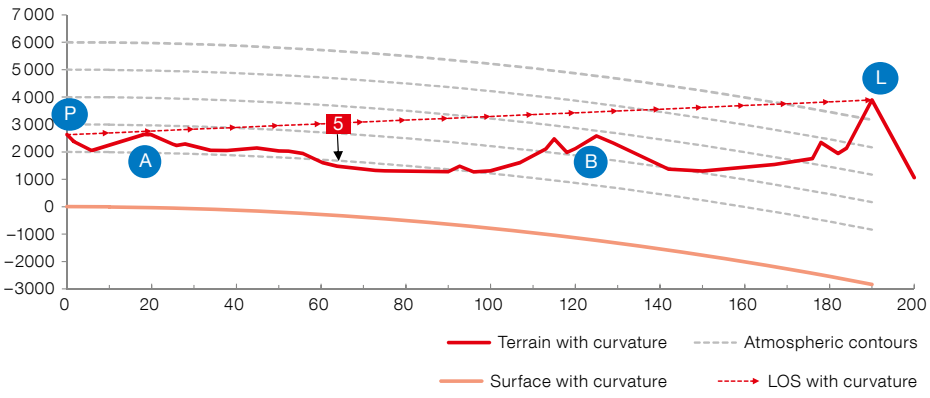

Figure 3. Same line of sight as Figure 2 but now considering surface curvature of the Earth. The LOS intersects with lower atmospheric layers than in Figure 2. This LOS with curvature is also sketched in Figure 2 (red dotted line).

curvature effect grows with D^2 it affects Sierra Vicuña Mackenna by 30 metres and the Cordillera de Domeyko, 125 kilometres away, by 1.2 kilometres. At the distance of Llullaillaco (190 kilometres) the surface curves down by an amazing 3.1 kilometres with respect to the tangential plane! So that the summit has effectively only an elevation of 3600 metres as seen from Paranal.

A careful analysis would also take atmospheric refraction into account: objects in the far distance are effectively lifted up and the effect of curvature is thus reduced. This is usually accounted for by choosing a 10 % higher value for *R* in the above formula, lifting Llullaillaco by the same 10 % to 4.1 kilometres. This effect is neglected in the following discussion.

Figure 4. Llullaillaco in winter, displaying a spectacularly rich contrast and wealth of details (taken on 14 July 2012 by Dimitri Gadotti).

The curvature effect is strongest for the most distant points, and much less so for the nearby and intermediate terrain. So, surface curvature makes it much easier for the Sierra Vicuña Mackenna to mask Llullaillaco, although it is only at the same altitude (2645 metres, curvature-corrected) as Paranal itself. The curvature-corrected LOS requires 2763 metres at that distance, giving a clearance of just 120 metres (point A in Figures 2 and 3), which could indeed be called a near-miss given the geometrical dimensions of the problem. The much higher Cordillera de Domeyko (3882 metres and 125 kilometres distance away; point B in Figures 2 and 3) is less critical for the LOS, since it is itself curvature-reduced by 1.2 kilometres, giving a comfortable clearance of more than 800 metres.

Transparency

With the geometry sorted out, now we need to look at sky transparency: how is it possible to look through the atmosphere along a 190-kilometre baseline and still retain excellent contrast (as evident from Figure 4)?

Light travelling through the atmosphere, no matter whether it is starlight or sunlight scattered off Llullaillaco towards Paranal, is both absorbed and scattered. We are discussing here much stronger effects than are usual in astronomy: lines of sight towards the stars traverse the atmosphere roughly vertically, with a typical scale height of 8 kilometres, and the first, and worst, 2.6 kilometres have already been truncated by Paranal's elevation. Here, we look through 190 kilometres of air, almost tangentially. What is the typical atmospheric elevation across that LOS? The blue LOS in Figure 2 steadily increases from 2600 to 6700 metres, but that needs to be corrected since the atmospheric layers follow the gravitational curvature (Figure 3). This is the red LOS in Figure 3, repeated in Figure 2: all points except the two end points cross lower atmospheric layers than the uncorrected LOS, with the maximum difference of about 600 metres in the middle, 95 kilometres from Paranal. Assuming constant density in the atmosphere, the effective average altitude in the uncorrected LOS would be 4700 metres, and 4200 metres with curvature correction. A more realistic description of the atmosphere would take into account its exponential structure, with a much higher weighting given to the lowest layers. Since these are close to Paranal, where curvature is smallest, we can keep things simple and ignore the curvature-induced correction in the following.

The LOS towards Llullaillaco is dominated by atmospheric layers well above the atmospheric boundary layer, sometimes also called the inversion layer. Most of the atmospheric dust, aerosols and humidity are trapped below that boundary zone. Astronomical observations with Paranal

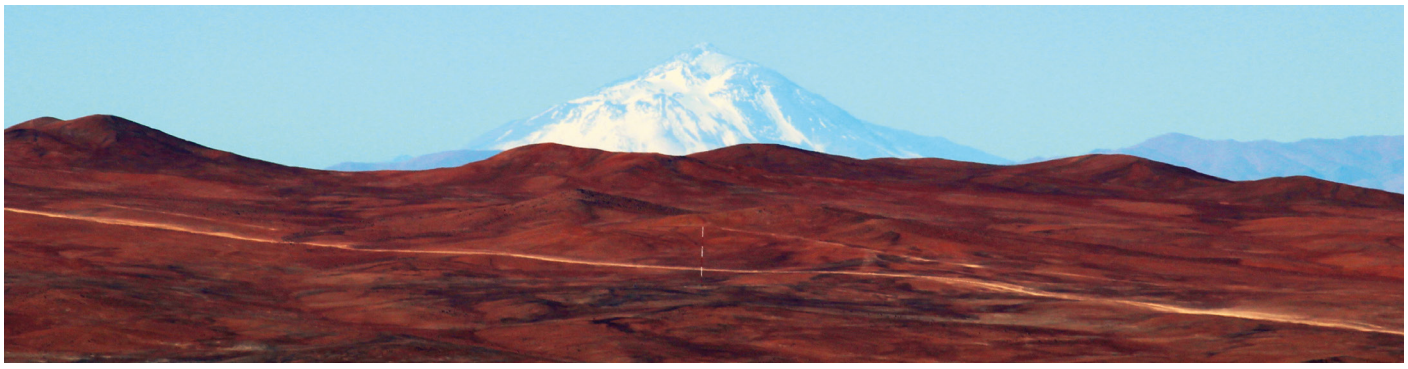

Dimitri Gadotti/ESO

instruments measure the quality of the atmosphere by the extinction, the fraction of light being absorbed or scattered by the atmosphere. In the *V* passband (visual, centred around 550 nm) the extinction towards the zenith is about 0.12 mag, or about 12% on a good Paranal night, occurring in the roughly 4–5 kilometre-long column of air effectively contributing above the observatory. Most of the extinction is caused by scattering, whereby the wavelength of the photon is preserved, but its directional information is lost, degrading the contrast. (Light is scattered out of the LOS, but light from other sources is also randomly scattered into the LOS. Blue daylight is an example of the scattering of blue sunlight, completely disassociated from its original direction.)

In clear skies, mountains turn blue in the distance, just like the open sky, and eventually can't be distinguished from the sky. So what do you need to see a target at 190 kilometres, apart from visibility? Contrast! Llullaillaco is very cooperative with visible snow fields on dark lava rocks throughout the year, and in particular during the winter months (Figures 4 and 7).

Still, with 12 % contrast loss over 5 kilometres, less than 1% of "quality" light (with preserved directional and colour information) would remain over a 190-kilometre baseline, while a rule-of-thumb suggests that a minimum of 2 % contrast is required[3]. Looking at Figure 4, the contrast of Llullaillaco must be much better than 2%: one can distinguish crisp white and dark bands that can readily be identified with features visible on satellite imagery presented by Google Earth (Figure 6). Visibility of this quality is not a rare exception, as confirmed by quotes from frequent Paranal observers (Gadotti, 2013; priv. comm.) and by other pictures, like the one by Gerd Hüdepohl (Figure 7).

The apparent contradiction between these photographs with their amazing contrast, and the estimates from astronomical observations can likely be explained by assuming that most of the atmospheric extinction actually happens even closer to the ground than assumed above, in the densest parts of the atmosphere just above the Observatory. It seems that beyond roughly 3500–4000 metres, the Atacama atmosphere does not contribute significantly to the extinction, and the larger part of the LOS towards Llullaillaco suffers virtually no extinction.

Figure 5. Summer view of Llullaillaco taken by the author, from Cerro Armazones, in November 2009.

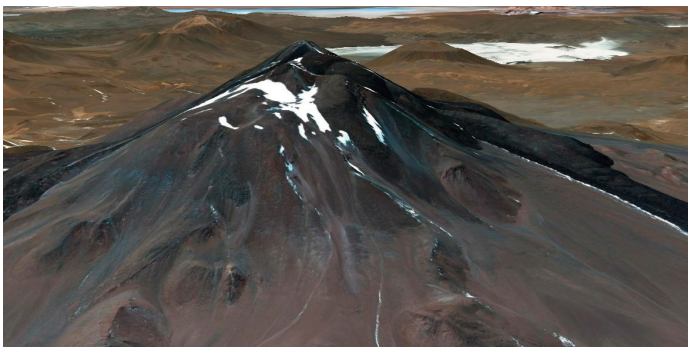

Figure 6. Satellite picture of Llullaillaco, rendered in 3D by the author using the information available from Google Earth (view towards the east into Argentina, north is left, with Paranal behind the viewer). This close-up view is from almost the same direction as from Paranal.

The very long baseline must also be essentially free of dust; a significant assertion given all the open-pit mining and industrial activity taking place in the Atacama Desert. The main dust source in that direction, the Escondida copper mine (currently the largest on Earth), is comfortably north of the LOS to Llullailliaco.

Are there other peaks visible from Paranal, constituting a true "skyline"? There are some other candidates in the "summit 6000" club, like Socompa (6050 metres at 222 kilometres); Lastarria (5700 metres, 202 kilometres; not quite 6000 metres, but close); or Pular (6230 metres, 244 kilometres). However, all of these are hidden behind the Sierra Vicuña Mackenna as seen from Paranal. But moving just a bit higher, as Gerd Hüdepohl did for his famous aerial photo (Figure 7), helps a lot when trying to spot the volcano Socompa. This mountain to the north of Llullaillaco is also visible from Cerro Armazones. Possibly Cerro Pular is also visible (6230 metres, 244 kilometres), but this is unconfirmed. None of them offers the same spectacular view as Llullaillaco since they are lower in altitude, further away, and have few if any snow fields.

Finally, there is another interesting question: could one spot Paranal from Llullaillaco? The issue is contrast, again. Seen from Cerro Armazones, Paranal is mainly visible by its structures, and the contrast is poor even at short distances, at least for most of the day. Spotting Paranal from the summit would require climbing to at least 5500 metres (roughly the altitude of the lowest part of Llullaillaco visible from Paranal). The best contrast could be expected in the morning, so you would need to stay overnight, at temperatures reported by mountaineers to be as low as –20 or –30°C. Just before morning

Gerd Hüdepohl/ESO

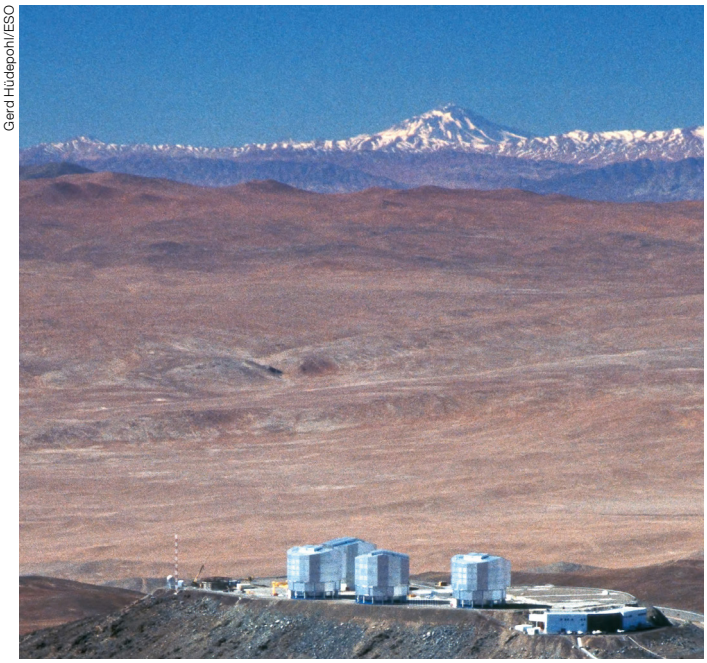

Figure 7. Winter view of Llullaillaco, taken by Gerd Hüdepohl in July 2002 from an aeroplane, i.e., with a slightly different LOS than in the other pictures, but from a similar distance. The volcano Socompa is the peak close to the lefthand edge.

coffee you could probably spot the first rays of the Sun reflected off the silver domes in a spectacular flash, as in Gianluca Lombardi's picture of Paranal taken from Cerro Armazones[4]. Probably the three Inca children could tell, as they might have enjoyed this view every morning for a few years. Not for too long though, since their mummies were discovered in 1999 and taken to a museum in Salta/Argentina.

Links

[1] Cerro Llullaillaco: http://en.wikipedia.org/wiki/Llullaillaco
[2] Mean radius of the Earth: http://en.wikipedia.org/wiki/Horizon
[3] Contrast of distant objects: http://en.wikipedia.org/wiki/Visibility
[4] View of Paranal from Armazones: http://www.eso.org/public/images/potw1205a/

Hännes Heyer Retires

Lars Lindberg Christensen[1]

[1] ESO

Figure 1. Among the gifts received by Hännes Heyer at his farewell reception on 6 December 2012 was a mounted print of one of his photographs signed by his colleagues. He is shown holding this trophy aloft.

Hännes, or Hans Hermann, Heyer was at ESO for 25 years and experienced the remarkable coincidence of being honoured for both his retirement and celebrating his 25th anniversary at ESO on the same day. On the morning of 6 December 2012 the Director General hosted a small ceremony for Hännes as well as two other staff members, Hélène Neuville and Enzo Brunetto, and in the afternoon Hännes was at the centre of a reception in the Council Room in Garching (see Figure 1).

There is hardly anyone at ESO who does not know Hännes. He has played an important role in taking and curating our photographs since the days of the ESO Information and Photographic Service (IPS, reflecting the origins of key staff in the former ESO Sky Atlas Laboratory). The IPS was created in 1986, during the exciting time of the 1985–86 Halley apparition. At that time, science communication as a profession hardly existed and a fully developed conceptual framework

for such activities had yet to materialise. In that sense, at least in Europe, ESO certainly found itself among the pioneers in the field. Hännes, hired as a photographer and one of the first people in this new progressive department in 1987, was one of those pioneers.

With growing experience came the realisation that information is a commodity that must be managed, and the department changed its name in the early 1990s to the ESO Education and Public Relations Department (EPR), and naturally Hännes moved into the new era. The new name revealed the strategic choice that ESO had made in engaging in science education activities. In 2005, the department underwent a restructuring, following the recommendations of the 2004 ESO Visiting Committee as far as possible. The name change to the Public Affairs Department (PAD) signified a step towards addressing political decision-makers and administrators. After a review in 2008, PAD became the education and Public Outreach Department (ePOD) as it is known today. As our photographer, Hännes has documented many of the key moments in ESO's history during his time here, and he has an almost encyclopaedic knowledge of the events, people, and images over the decades.

As such, he played an important role in our celebrations of ESO's 50th Anniversary in 2012, and he worked closely with

Figure 2. One of Hännes' early photographic images of which he was proud — moonrise over the Andes from La Silla.

Claus Madsen on many of the photographs in his book *The Jewel on the Mountaintop*. Historical photographs are an area where Hännes made an important and long-lasting impact: in the lead-up to the anniversary a significant effort was made to digitise the most important photographs in ESO's historical photo archive to create a legacy that will stand for many years.

Hännes has really left his mark on ESO: when you walk around the buildings in Garching and Chile, many of the photographs you'll see on the walls are from him. Also many of the photographs that have featured in *The Messenger* were taken by Hännes and many ESO staff, visitors and committee members have been photographed by him, whether at meetings, in group photos, or even for staff ID cards.

A big thank you to Hännes for all he has put into ESO over the past 25 years!

New Implementation of the ESO Data Access Policy

As of ESO Observing Period 91, the ESO Science Archive Facility is the sole access point for data obtained with ESO telescopes. This includes access to proprietary data for both Visitor and Service Mode runs.

Typically, the files become available from the Science Archive Facility[1] within a few hours of the time of observation. The Archive Calibration Selector service allows associated calibrations and ancillary files to be associated to raw science files for further processing.

As of 1 April 2013, the proprietary period for all science and acquisition files will run from the moment the file can be accessed and downloaded from the Archive. This means that the "proprietary period" will begin on that date. No PI or PI delegate action will affect the proprietary period.

This new implementation applies to all observations belonging to Observing Period 91 and onwards, as well as data from earlier Observing Periods which were carried over to Period 91.

Links

[1] Science Archive Facility: http://archive.eso.org

Fellows at ESO

Luca Cortese

Luca Cortese

Becoming an astronomer was definitely not my childhood dream. Until secondary school, I wanted to become an architect and design something as amazing as the Sydney Opera House. I suspect that this was mainly driven by my early great passion for LEGO.

I was born and grew up in Milano (Italy) and only started to develop a deep interest in astrophysics during high school. A significant influence on this passion came from my father's fascination with astronomy and, probably, also from the fact the walls of my parents' house have always been filled with maps of the night sky and images of Jupiter's moons taken by *Voyager 2*. Thus, when I started my undergraduate degree in physics at Milan University in the autumn of 1997, my goal was to become a professional astronomer. However, I had to wait until winter 2001 to start getting my hands dirty with what, since then, has become my everyday job.

As part of Peppo Gavazzi's course of laboratory astrophysics, we went to the Loiano Observatory (in the Italian Apennines) to observe galaxies in nearby clusters. At least this was the original plan. Out of the ten nights we had, eight were lost due to bad weather and we were almost ready to pack and go back home when the sky finally started to clear. Unfortunately, it had snowed a lot during the previous days and the dome was covered in snow. Thus, we ended up spending the entire afternoon manually clearing the dome and the roof of the building, just to be able to have our first hands-on experience at the telescope. The following night turned out to be an amazing experience, and I realised then that observational astronomy was exactly what I wanted to do. For the final stage of my undergraduate degree, I decided to undertake a Master's thesis with Peppo on the analysis of Hα images of galaxies in nearby clusters. The experience was so rewarding that I was even more certain that I had taken the right path.

My initial plan was to leave Italy and carry out a PhD abroad. However, finding a PhD place turned out to be more complicated than anticipated and I ended up staying in Milan, where I started a PhD under Peppo's supervision at the end of 2002. Looking back at those days, I am very glad with how things went. I was lucky enough to win a grant that allowed me to carry out half of my thesis work in France, at the Laboratoire d'Astrophysique de Marseille, under the supervision of Alessandro Boselli. This gave me the opportunity to become heavily involved in the exploitation of the data obtained by the GALEX mission, a NASA space telescope which carried out the first survey of the entire sky at ultraviolet wavelengths. So, I spent the three years of my PhD studying the effects of the environment on the star formation and dust extinction properties of cluster galaxies. It was during this time that I had my first experience at ESO, observing at the 3.6-metre telescope in La Silla. This was a very different experience compared to my previous observing trips: the system performance was very smooth, which made the observations almost too easy (when it comes to observations, "boring is good"!).

With a PhD degree in the bag, on a rainy day in January 2006 I filled up my car with all my stuff and drove the 1500 kilometres between Milan and Wales to start a postdoctoral position at Cardiff University, in the group led by Jonathan Davies. Although my initial contract was for just one year and half, I spent four and half amazing years in Wales. Working at Cardiff has been a great experience both professionally and personally. At first, my investigations shifted from the ultraviolet to the radio regime, as I carried out 21 cm observations of nearby galaxies to study their atomic gas reservoir. This gave me the opportunity to use the Arecibo radio telescope in Puerto Rico, the largest single-dish telescope in the world, and definitely one of the most amazing astronomical facilities I have had the privilege to use. Then, starting from 2008, I changed wavelength domain again, becoming deeply involved in the planning and exploitation of far-infrared and submillimetre surveys of nearby galaxies carried out with ESA Herschel Space Observatory. Herschel observations are crucial to gain information on the role played by the dust on the star formation cycle of nearby galaxies.

In the summer of 2010, I crossed the Channel again to start a Fellowship at ESO in Garching. Working at ESO has allowed me to experience directly how the Atacama Large Millimeter/submillimeter Array (ALMA) works. The opportunity to help carry out Cycle 0 observations at the ALMA site, and experiencing how this amazing facility works, is definitely the highlight of my time at ESO. Moreover, by getting involved in ALMA, I have been able to gain familiarity with millimetre interferometric observations. This is one of the most amazing parts of this job. In the last ten years I have been able to keep studying the same galaxies, but the advent of new facilities has made it possible to look at them from very different points of view, thus always yielding new insights into how they formed and evolved.

ESO is definitely a unique place at which to carry out a postdoctoral fellowship. It provides you with deep insights into how modern observatories work, something that it is impossible to imagine while working at other universities or research institutes.

Sadly, my experience at ESO is now coming to an end. In just a few months I will leave Europe to move to Australia, opening another, certainly exciting, chapter of my job as an astronomer.

Grant Tremblay

Grant Tremblay

When I was nine years old, I was the world's worst paleontologist. Based on embarrassingly weak evidence, I was convinced that there was a dinosaur buried in the field behind my house in Maine, USA. I asked my father to inform the local science museum of my impending find, and I launched a carefully planned and well-researched expedition to excavate it. When I mistook the white root of a sapling for the neck bone of a *Dilophosaurus*, I was overcome with the sort of elation that could only herald a future astronomer's first spectacular failure in science.

I may have been disappointed when I realised my dinosaur was actually a mound of dirt and shrubbery, but the experience was a perfect illustration of why I love science. Amid the collapse of my hypothesis, I learned the difference between bones and fossils, discovered that plant roots could be bright white, and realised, after some follow-up research, that a field in Maine is not the likeliest place to find giant ancient reptiles. Most importantly, I learned that human beings advance our understanding of Nature not by becoming more right, but by slowly becoming less wrong. Today, I am grateful for the privilege of working in a field where getting things wrong is the most important part of eventually getting it right.

This is why I feel so lucky to be at ESO. After doing half of my PhD research at the Space Telescope Science Institute (the operational heart of the Hubble Space Telescope) and the other half in Rochester, I had dreamed of going to Europe for my first postdoc. Being from the US, an ESO Fellowship felt so out of reach. Yet in addition to building the world's greatest telescopes, one of ESO's most important gifts to the world is its perfect illustration of international cooperation toward a common goal, and of human collaboration that is blind to borders and flags. ESO welcomed me, and I now live in both Germany and Chile, and have an incredible group of friends and collaborators from no less than 27 different countries. In addition to my Fellowship in Garching, my ESO duties are performed as an astronomer in the Paranal Observatory Science Operations team, supporting UT2/Kueyen on the Very Large Telescope. Every night at the telescope, I feel like that kid in the field in Maine.

My own research uses data from the VLT, as well as the Hubble Space Telescope, Chandra X-ray Observatory, Herschel and now ALMA to study the black-hole-powered outflows of nearby radio galaxies. They are amongst the largest and most powerful objects in the Universe, and many of them are embedded in megaparsec-scale halos of ultra-hot primordial gas. The mechanical feedback associated with the propagation of these outflows amid their atmospheres excavates buoyant bubbles large enough to encompass 500 Milky Way galaxies. And I thought dinosaurs were big!

I don't know where I'll end up next, but I'll always be grateful for my years at ESO. A year after my failed dinosaur hunt, I first saw the rings of Saturn through my tiny toy telescope, and it started me on the path towards becoming an astronomer. Twenty years later, thanks to ESO, I find myself writing these words in the Paranal Observatory control room, using a telescope with 12 000 times greater light-collecting area. I still haven't found any dinosaurs, but I guess I haven't stopped searching.

ESO Studentship Programme

The research studentship programme of the European Southern Observatory provides an outstanding opportunity for PhD students to experience the exciting scientific environment at one of the world's leading observatories for a period of up to two years.

ESO is the foremost intergovernmental astronomy organisation in Europe. Its approximately 110 staff astronomers, 40 Fellows and 50 PhD students conduct frontline research in fields ranging from exoplanets to cosmology, offering one of the most vibrant and stimulating scientific settings anywhere in the world.

ESO's studentship positions are open to students enrolled in a PhD programme in astronomy or related fields. Students accepted into the programme work on their doctoral project under the formal supervision of their home university, but they come to ESO to work and study under the co-supervision of an ESO staff astronomer, normally for a period of between one and two years. Studentships may be hosted either at ESO's Headquarters in Garching (Germany) or at ESO's offices in Santiago (Chile), where two additional positions per year are provided for students enrolled in South American universities.

Applicants and their home institute supervisors should agree upon and coordinate their research project jointly with their prospective ESO supervisor. For this purpose the ESO supervisor should be contacted well in advance of the application deadline (15 June 2013). A list of potential ESO supervisors and their research interests can be found at http://www.eso.org/sci/activities/personnel.html. A list of PhD projects currently being offered by ESO staff is available at http://www.eso.org/sci/activities/thesis-topics.html.

It is highly recommended that applicants plan to start their PhD studies at their home institute before continuing to develop their research projects at ESO.

ESO Chile students have the opportunity to visit the observatories and to get involved in small technical projects aimed at giving insights into the observatory operations and instrumentation. Such involvement is also strongly encouraged for Garching students. In addition, students in Garching may attend and benefit from the series of lectures delivered in the framework of the International Max Planck Research School on Astrophysics.

Students who are already enrolled in a PhD programme in the Munich area (e.g., at the International Max Planck Research School on Astrophysics or a Munich University) and who wish to apply for an ESO studentship in Garching, should provide a compelling justification for their application.

The Outline of the Terms of Service for Students (http://www.eso.org/public/employment/student.html) provides some additional details on the employment conditions and benefits.

If you are interested in enhancing your PhD experience through an extended stay at ESO please apply online at https://jobs.eso.org/. Reference letters to support your application should be sent to vacancy@eso.org for Garching and vacchile@eso.org for Chile.

Please include the following documents in your application:
– a Curriculum Vitae (including a list of publications, if any);
– copies of your university transcript and certificate(s) or diploma(s);
– a summary of your master's thesis project (if applicable) and ongoing projects, indicating the title and the supervisor (maximum half a page);
– an outline of the proposed PhD project highlighting the advantages of coming to ESO (recommended one page, maximum two);
– two letters of reference, one from the home institute supervisor and one from the ESO local supervisor;
– a letter from the home institute that i) guarantees the financial support for the remaining PhD period after the termination of the ESO studentship, ii) indicates whether the requirements to obtain the PhD degree at the home institute have already been fulfilled.

All documents should be typed in English (but no translation is required for the certificates and diplomas).

Closing date for applications is 15 June 2013, and review of the application documents (including the recommendation letters) will begin immediately. Incomplete applications will not be considered.

Candidates will be notified of the results of the selection process during July–August 2013. Studentships typically begin between August of the current year and March of the following year.

For further information please contact Christina Stoffer (cstoffer@eso.org).

Although recruitment preference will be given to nationals of ESO Member States (members are: Austria, Belgium, Brazil, the Czech Republic, Denmark, Finland, France, Germany, Italy, the Netherlands, Portugal, Spain, Sweden, Switzerland and United Kingdom) no nationality is in principle excluded.

The post is equally open to suitably qualified female and male applicants.

Announcement of the ESO Workshop

Deconstructing Galaxies: Structure and Morphology in the Era of Large Surveys

18–22 November 2013, ESO Vitacura, Santiago, Chile

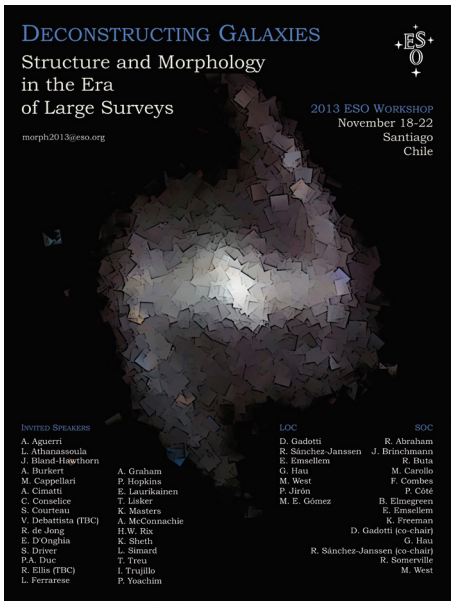

The study of the structure and morphology of galaxies is one of the major tools astronomers have to address how galaxies form and evolve. Recent progress in the field has boosted our understanding of the properties of different structural components in nearby galaxies, as well as in galaxies at intermediate redshifts ($z \sim 1$–2). Yet the link between structural properties, kinematics, stellar population content and the complex physics involved in the formation and evolution of galaxies is a much more challenging step. One of the major goals of this conference is to address this connection, by questioning, for instance, what the structure of galaxies tells us about their formation and evolution, and how observations can help constrain models.

In addition, the complexity of methods used to obtain structural measures has grown considerably in recent years. It is thus important to address the strengths and limitations of the different techniques, particularly with the expectation that automated procedures designed to handle large surveys may prevail in the future.

This conference will bring together over 100 observers and theorists, and it is intended to be highly participative with substantial time devoted to discussions. It should set the basis for the study of galaxy structure and morphology in the next decade.

Pre-registration is open until 1 April.

Details are available at:
http://www.eso.org/sci/meetings/2013/morph2013.html
or by email to: morph2013@eso.org.

Announcement of the ESA/ESO Workshop

SCIENCE OPERATIONS 2013: Working Together in Support of Science

10–13 September 2013, ESAC, Madrid, Spain

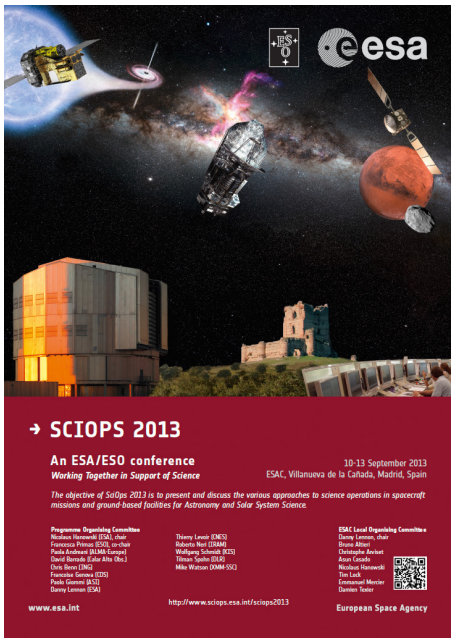

The objective of SCIOPS 2013 is to present and discuss the various approaches to science operations in spacecraft missions and ground-based facilities for astronomy and Solar System science.

The meeting is intended to:
– Compare and improve our processes and approaches
– Foster innovations
– Enable a more efficient use of our resources
– Establish and intensify collaborations

via a focus on:
– Community support and services
– Science and instrument planning
– Instrument handling and calibration
– Science data processing
– Science data archiving and product generation
– Science operations organisation and management

... throughout all project phases from initial concepts to legacy products.

Details are available at:
http://www.sciops.esa.int/sciops2013 or by email to: sciops2013@sciops.esa.int.

The abstract deadline is 1 May 2013 and registration will close on 15 July 2013.

Announcement of the Workshop

400 years of Stellar Rotation

17–22 November 2013, Natal, Brazil

In 1613 Galileo Galilei reported in the *l'Istoria e dimostrazioni intorno alle macchie solari e loro accidenti* the evidence of solar spots and the interpretation of their motion as due to solar rotation. After 400 years we are able to quantify, thanks to extremely fine experiments like SOHO, details of the internal and surface rotation of the Sun, and to measure, thanks to precise photometry obtained with the Kepler and COROT satellites, rotation periods for large numbers of stars. In addition, projected rotational velocities (*Vsini*) are now available for thousands of these stars, thanks to ground-based high resolution spectroscopy. These data offer the unique possibility to study in detail the behaviour of the rotation of the Sun over time, as well as the evolutionary behaviour of stellar rotation all along the Hertzsprung–Russell diagram.

Stellar rotation is not only a key ingredient to understanding solar and stellar angular momentum evolution properly. This fundamental parameter can also provide important constraints for models of stellar evolution, as well as important information on the presence of external rotational brakes, tidal interactions in binary systems and on the mechanisms controlling stellar activity. Rotation also plays a primary role in stellar chemical evolution and it reflects the complex interaction between stars and the circumstellar/protoplanetary disc in the pre-main sequence phase.

To celebrate the 400 years of the public announcement of the Sun's rotation by Galileo Galilei, the workshop, *400 Years of Stellar Rotation*, co-sponsored by the European Southern Observatory and the International Institute of Physics of Natal, will be held in Natal, Brazil.

Additional information can be found at the workshop website: http://www.dfte.ufrn.br/400rotation/.

Registration is open until 1 June 2013.

Personnel Movements

Arrivals (1 January–31 March 2012)

Europe	
Barbosa, Carlos Eduardo (BR)	Student
De Pascale, Marco (I)	Student
Gall, Elisabeth (D)	Student
Jochen, Haucke (D)	Head of Software Engineering
Riedel, Mario (D)	Administrative Clerk
Zocchi, Alice (I)	Student

Chile	
González, Edouard (RCH)	Telescope Instruments Operator
Pallanca, Laurent (F)	Instrumentation Engineer
Razmilic, Jasna (RCH)	Executive Assistant
Sippel, Anna (D)	Student
Smith, Gerardo (RCH)	Electronics Technician

Departures (1 January–31 March 2012)

Europe	
Allouche, Fatme (RL)	Instrumentation Engineer
Alvarez Candal, Alvaro (RA)	Fellow
Drouart, Guillaume (F)	Student
Iribarrem, Alvaro (BR)	Student
Lakicevic, Masha (SRB)	Student
Longmore, Steven (GB)	Fellow
Märcker, Matthias (D)	Fellow
Rushton, Anthony (GB)	Fellow
Smolcic, Vernesa (HR)	Fellow
Zilker-Kramer, Irmtraud (D)	Paid Associate

Chile	
Araya, Ernesto (RCH)	Optical Technician
Barria, Daniela (RCH)	Student
Bhatia, Ravinder (GB)	Project System Engineer
de Graauw, Mattheus Thijs (NL)	ALMA Director
Lieder, Stefan (D)	Student
Riffo, Lidia (RCH)	Secretary
Tyndall, Amy (GB)	Student
West, Michael (USA)	Head of Science Vitacura

Annual Index 2012 (Nos. 147–150)

Subject Index

Astronomical News

Author Index

ESO, the European Southern Observatory, is the foremost intergovernmental astronomy organisation in Europe. It is supported by 15 countries: Austria, Belgium, Brazil, the Czech Republic, Denmark, France, Finland, Germany, Italy, the Netherlands, Portugal, Spain, Sweden, Switzerland and the United Kingdom. ESO's programme is focused on the design, construction and operation of powerful ground-based observing facilities. ESO operates three observatories in Chile: at La Silla, at Paranal, site of the Very Large Telescope, and at Llano de Chajnantor. ESO is the European partner in the Atacama Large Millimeter/submillimeter Array (ALMA) under construction at Chajnantor. Currently ESO is engaged in the design of the European Extremely Large Telescope.

The Messenger is published, in hard-copy and electronic form, four times a year: in March, June, September and December. ESO produces and distributes a wide variety of media connected to its activities. For further information, including postal subscription to The Messenger, contact the ESO education and Public Outreach Department at the following address:

ESO Headquarters
Karl-Schwarzschild-Straße 2
85748 Garching bei München
Germany
Phone +49 89 320 06-0
information@eso.org

The Messenger:
Editor: Jeremy R. Walsh;
Design, Production: Jutta Boxheimer;
Layout, Typesetting: Mafalda Martins;
Graphics: Roberto Duque.
www.eso.org/messenger/

Printed by Color Offset GmbH,
Geretsrieder Straße 10,
81379 München, Germany

ISSN 0722-6691

Contents

Front cover: The spiral galaxy NGC 2442 is shown in a colour composite from images taken by the Wide Field Imager on the MPG/ESO 2.2-metre telescope. Images in two broadband filters (*B* and *V*) and a narrowband, isolating the emission lines Hα and [N II], were combined. This peculiar tidally distorted SAB spiral galaxy is situated at about 21 Mpc, has a low ionisation active galactic nucleus (LINER) and a core collapse supernova was observed in the southern spiral arm (SN 1999ga). See Photo Release eso1115 for more details.